AD-A113 597 SCIENCE APPLICATIONS INC MCLEAN VA F/G 20/9
RADIATION FROM HIGH TEMPERATURE PLASMAS.(U)
FEB 82 E KANE, J APRUZESE N00173-80-C-0493
UNCLASSIFIED SAI-82-686-WA NL

1 OF 3
AD A
113597

12

SCIENCE APPLICATIONS, INC.

[illegible]

[illegible]

RADIATION FROM HIGH TEMPERATURE PLASMAS

SAI-82-686-WA

Prepared by:
Edward Kane and John Apruzese

ATLANTA • ANN ARBOR • BOSTON • CHICAGO • CLEVELAND • DENVER • HUNTSVILLE • LA JOLLA
LITTLE ROCK • LOS ANGELES • SAN FRANCISCO • SANTA BARBARA • TUCSON • WASHINGTON

RADIATION FROM HIGH TEMPERATURE PLASMAS

SAI-82-686-WA

FINAL REPORT

February 1982

Submitted to:

Plasma Physics Division
Naval Research Laboratory
Washington, D.C. 20375

Prepared Under:

Contract No. N00173-80-C-0493

Prepared by:

Edward Kane and John Apruzese
Science Applications, Inc.
McLean, VA 22102

SCIENCE APPLICATIONS, INC.

P.O. Box 1303
1710 Goodridge Drive
McLean, Virginia 22102
(703) 734-5840

SECURITY CLASSIFICATION OF THIS PAGE (When Data Entered)

REPORT DOCUMENTATION PAGE		**READ INSTRUCTIONS BEFORE COMPLETING FORM**
1. REPORT NUMBER	2. GOVT ACCESSION NO. AD-A113597	3. RECIPIENT'S CATALOG NUMBER
4. TITLE (and Subtitle) RADIATION FROM HIGH TEMPERATURE PLASMAS		5. TYPE OF REPORT & PERIOD COVERED Final Report 27 Aug 80 - 31 Dec 81
		6. PERFORMING ORG. REPORT NUMBER SAI-82-686-WA
7. AUTHOR(s) Edward Kane and John Apruzese		8. CONTRACT OR GRANT NUMBER(s) N00173-80-C-0493
9. PERFORMING ORGANIZATION NAME AND ADDRESS Science Applications, Inc. P.O. Box 1303, 1710 Goodridge Drive McLean, Virginia 22102		10. PROGRAM ELEMENT, PROJECT, TASK AREA & WORK UNIT NUMBERS
11. CONTROLLING OFFICE NAME AND ADDRESS Plasma Physics Division Naval Research Laboratory Washington, D.C. 20375		12. REPORT DATE February 1982
		13. NUMBER OF PAGES
14. MONITORING AGENCY NAME & ADDRESS(if different from Controlling Office)		15. SECURITY CLASS. (of this report) Unclassified
		15a. DECLASSIFICATION/DOWNGRADING SCHEDULE

16. DISTRIBUTION STATEMENT (of this Report)

17. DISTRIBUTION STATEMENT (of the abstract entered in Block 20, if different from Report)

18. SUPPLEMENTARY NOTES

19. KEY WORDS (Continue on reverse side if necessary and identify by block number)

z-pinch, mass scaling, plasma mixtures, spectroscopic signatures, imploding discharge, collisional-radiative atomic model, radiation hydrodynamics

20. ABSTRACT (Continue on reverse side if necessary and identify by block number)

The dominant physics affecting spherical and cylindrical plasma implosions is studied. Detailed modeling of opacity sources, line and continuum emission, and coupled hydrodynamics is presented. Simulations of actual experimental spectra, plasma mixture experiments, and improved photon transport methods are described. Z-pinch code benchmarks, and output predictions for various elements and mass loads are given.

DD FORM 1 JAN 73 1473 EDITION OF 1 NOV 65 IS OBSOLETE
S/N 0102-LF-014-6601

SECURITY CLASSIFICATION OF THIS PAGE (When Data Entered)

(This page intentially left blank.)

TABLE OF CONTENTS

TABLE OF CONTENTS (Continued)

TECHNICAL DISCUSSION

1. INTRODUCTION

SAI has continued to achieve notable gains in understanding the interactive dynamics of radiative emission, absorption, and exchange, and plasma hydrodynamic motion. During the performance period of the contract addressed by this report (27 August 1980 to 31 December 1981) the r-dependent collapsing z-pinch code WHYRAD was vastly improved in numerical efficiency and flexibility and benchmarked to establish its accuracy. The code was applied to various experimental conditions and elements in a predictive and analytical effort which yielded much insight into the general physics as well as specifically valuable design guidelines. Important advances were made in the modeling of the radiation itself (apart from the hydrodynamics), such as extension of escape probability techniques to cylindrical and spherical geometry. Our efforts in detailed radiation modeling are covered in Section 2 and Appendices A through C; the z-pinch radiation-hydrodynamics calculations are described in Section 3 with a discussion of the WHYRAD code subroutines included in Appendix D.

2. DETAILED RADIATION MODELING

As we have demonstrated in a previous NRL contract and in publications,(1) the application of escape probability concepts to line transport can be very fruitful in reducing computational labor while maintaining an adequate degree of accuracy. Until this year such applications have been limited to plane parallel geometry due to the difficulties of solid-angle integrations in spherical and cylindrical geometry. However, we have discovered a method to bypass the integrations by use of a single angle for inner-to-outer cell couplings and a reciprocity relationship for coupling constants for outer-to-inner cell couplings. This allows the extension of probabilistic techniques to cylindrical and spherical geometry. The mathematics is detailed in Appendix A, "Direct Solution of the Equation of Transfer Using Frequency- and Angle-Averaged Photon-Escape Probabilities for Spherical and Cylindrical Geometries."

Our extensive spherical plasma spectrum simulation capability utilized for NRL is aimed at employment in pellet experiments where the actual emitted spectrum is measured. Before such an approach is employed with confidence, the usefulness of the simulated spectra must be benchmarked. Last year's report(2) presented a successful one-on-one comparison of a calculated neon spectrum with a published spectrum obtained from a pellet implosion experiment at the University of Rochester. This demonstrated that an exact replication of an experimental spectrum from an optically thick plasma was feasible and could lead to accurate temperature and density diagnostics.

Since then a great many more pellet spectrum calculations have been performed for predictive and analytical purposes. The goal of this latterset of calculations is to understand how the spectrum changes with pellet temperature and density. The calculations are detailed in Appendix B, "Collisional-radiative-equilibrium spectroscopic diagnosis of a compressed, optically thick neon plasma." In addition to elaborating in detail the expected spectral changes with degree of heating or compression, an approximate analytic model of the approach to LTE of a multistate, multistage plasma is developed in this appendix.

Prediction and analysis of plasma mixture experiments and the effects of overlapping absorption and emission have been of continuing interest to SAI and NRL. We have recently considered photopumping in opacity resonances for Silicon/Aluminum and Sodium/Neon mixtures. Our detailed results are given in Appendix C, "Plasma Conditions Required for Attainment of Maximum Gain in Resonantly Photo-Pumped Al XII and NeIX."

Until this past year, our analyses of wire plasma spectra have concentrated on inferring average temperatures and densities for these plasmas. To this end, spectra from assumed isothermal, isodense plasmas have been computed and compared with the measurements in an iterative process until agreement was obtained. This was satisfactory as an initial procedure in obtaining approximate characteristic plasma temperatures and densities. Moreover, an understanding of more realistic situations where gradients are present may only be obtained if the simpler homogeneous plasmas and the evolution of their spectra are fully comprehended. This year we have extended our previous first order analyses of homogeneous plasmas to investigate the effects of gradients.

Some of the ambiguities(3) which may result from using line ratios only for spectroscopic diagnostics may be at least partially resolved by use of high-dispersion, high resolution spectroscopy in analyzing line profiles along with their measured intensity. Temperature gradients, in particular, are susceptible to diagnosis using line profiles, since the degree of self-reversal in an optically thick line depends on the radial temperature profiles.(4) A full physical explanation for this effect appears in Reference 4. As detailed in our final report for last year,(2) plasma implosion and its accompanying frequency Doppler shifts may transform a symmetric line profile self-reversal into an asymmetric one, with the blue wing dominant. In principle, therefore, both implosion velocity and temperature profiles may be inferred by analyzing an optically thick profile. We present the following analyses of exploded-wire spectra as successful applications of the usefulness of these effects.

A first-order analysis of the spectrum of PI shot 529 has been presented elsewhere.(5) In the present analysis we utilize the approximate information obtained previously to infer additional plasma properties from the Si XIII $1s^2$-1s 2p ^1P resonance line profile. As pointed out in reference 5, this line seemed to exhibit opacity broadening, with a peculiar "shoulder" present on the red wing of the line. A high dispersion spectrum of the appropriate wavelength region appears in fig. 1. If the average conditions diagnosed in ref. 5 ($T = 650$ eV, $n_e = 2 \times 10^{20}$) are applied in modeling the resonance line profile with an implosion velocity of 4×10^6 cm sec^{-1} at the outer plasma surface, one obtains from a multifrequency calculation the resonance line profile plotted in fig. 2. This profile was computed assuming an isodense, isothermal plasma and a pinhole-measured radius of 250 μm (P. Burkhalter, private communication). Note the striking resemblance to the measured spectrum of fig. 1. However, once the resonance line profile is convolved with the estimated 5 mÅ of experimental broadening (fig. 3) the shoulder feature washes out and the resemblance disappears. The isodense, isothermal model therefore does not work when the finite resolution of the spectrograph is properly accounted for.

The results of a vastly improved profile simulation for this shot are presented in figs. 4 and 5. Figure 4 presents the computed line profile (without experimental broadening added in) for a plasma identical to that of figs. 2 and 3 except that the temperature profile decreases sharply as radius increases. The inner 20% of the plasma is assumed to have a temperature of 1170 eV; from 20% to 100% of the total radius T_e is presumed to ramp linearly downward from 500 to 170 eV. This cold plasma exterior serves to improve the profile agreement by producing a deep self-reversal (see fig. 4). Even after convolution with a 3 mÅ instrumental gaussian, the profile is in excellent agreement (fig. 5) with experiment. This inference of a temperature gradient is fully in accord with our new analysis of another shot which we now discuss.

Based on an investigation of the effects of gradients on the emitted spectra of plasmas by some of the NRL staff(3) we have broadened and expanded our analysis of Maxwell Laboratories shot 159. This analysis further supports the inference of temperature gradients of the type described above in PI shot 329.

Shot 159 resulted from the implosion of Al wires and the measured time-integrated spectrum exhibits an asymmetric self-reversed profile for the Al XII $1s^2$-$1s\,2p\ ^1P$ resonance line (fig. 6). Symmetric self-reversed profiles are a well-understood, classical effect of large line opacity. To produce asymmetry with a suppressed red wing, however, the Doppler shift of plasma implosion <u>combined</u> with large line opacity is required, as detailed in last year's report. We previously obtained an excellent fit to this profile assuming a homogeneous plasma of radius 250 μ, temperature of 500 eV, ion density 8×10^{18} cm^{-3}, and implosion velocity 4×10^{6} cm sec^{-1}. However, this fit required an experimental spectral resolution $\Delta\lambda_e \leq 1.6$ mÅ in order that the profile not wash into a gaussian due to experimental broadening. This resolution is a factor of 2-3 better than the estimates (which are themselves somewhat uncertain). The washout to a gaussian could be prevented if the <u>intrinsic</u> profile (the one which would be measured with infinite resolution) were wider with a deeper core self-reversal. Such a profile can be produced by an <u>inhomogeneous</u> plasma with a hot core and colder outer region. We have found that by employing such a gradient in our simulation that the measured profile can be reconciled with larger experimental broadening and thus be completely consistent with all available information. A slightly smaller velocity of 2×10^{6} cm sec^{-1} is also required. This velocity is interpreted as the mean velocity of implosion during the K-shell emission pulse. We have also simulated the time-integration of the spectrum by summing the line profiles produced by a range of implosion velocities from 0 to 4 x 10^6 cm sec^{-1}, assuming the velocity changes linearly with time. The result is that the resultant "integrated" theoretical profile is virtually identical to that produced by snapshot emission from a plasma imploding at 2 x 10^6 cm sec^{-1}. Therefore, the velocity reflected by the shape of the emitted line profile is consistent with the physical mean velocity of implosion. This is to be expected, as a zero velocity plasma will produce a symmetric profile and one of say 4 x 10^6 cm sec^{-1} will produce a profile more skewed than at 2 x 10^6 cm sec^{-1}. The sum of the emitted profiles will thus be characteristic of an intermediate velocity which is also consistent with a physical mean. Of course, to produce this profile there is no escaping the conclusion that the bulk of the K-shell emission must occur during implosion rather than expansion after the peak compression.

The precise conditions we have inferred from line ratios as well as the resonance line profile are as follows: the inner 20% (radially) is at 900 eV; the outer 80% is at 400 eV just outside the 900 eV core and ramps linearly to 130 eV at the outer boundary of the emitting plasma. As is shown in the z-pinch solutions given in Sec. 5 the region of appreciable radiative yield is strongly dependent on the plasma density. In low emission regions with the high ionization level obtained, corona temperature can rise to 10 keV or more, but direct confirmation is lacking. The total ion density remains unchanged from our previous analysis at 8 x 10^{18} cm^{-3}. The plasma diameter of 1 mm is roughly consistent with the somewhat irregular configuration revealed by the pinhole picture. The profile produced by such a plasma is presented in figs. 7 through 9, for assumed instrumental linewidths of 0, 2, and 3 mÅ, respectively. Note that the experimental smearing of the intrinsic profile of fig. 7 gradually makes the self-reversal shallower, to the point where fig. 9's profile nicely matches experiment. The assumed resolution of 3 mÅ is in excellent agreement with estimates based on the experimental configuration. Figure 10 presents the profile of the resonance line which would be produced by an identical static plasma (no implosion). This line profile bears no resemblance to the experimental one--which fact, combined with the good resemblance of fig. 9--is clear evidence for implosion effects on the line emission in the laboratory frame. The character of the inferred temperature gradient closely resembles that of the silicon shot 329. Taken together, these two analyzed spectra demonstrate the power of spectroscopic analysis in inferring most, if not all, of the plasma properties of interest.

REFERENCES

1. J. P. Apruzese, J. Davis, D. Duston, and K. G. Whitney, J. Quant Spect. Radiat. Transfer, Vol. 23, p. 479 (1980).
2. J. P. Apruzese, E. Kane, P. Vitello, D. Duston, and A. Drobot, "Radiation From High Temperature Plasmas," SAI Report No. SAI-81-239-WA, Sept. 1980.
3. D. Duston, J. Davis, and P. C. Kepple, Phys. Rev. A, 24, 1505 (1981).
4. J. P. Apruzese, J. Davis, and K. G. Whitney, J. Appl. Phys. 48, 667 (1977).
5. P. Burkhalter, J. Davis, J. Rauch, W. Clark, G. Dahlbacka, and R. Scheider, J. Appl. Phys. 50, 705 (1979).

FIGURE CAPTIONS

Fig. 1 High dispersion spectrum of the SI XIII $1s^2$-$1s\ 2p\ ^1P$ and intercombination lines obtained from PI shot 329.

Fig. 2 Theoretical resonance and intercombination line profile obtained from a 250 μm Si plasma of implosion velocity 4×10^6 cm sec^{-1}. Assumed temperature is 650 eV; electron density, 2×10^{20} cm^{-3}.

Fig. 3 Same as Fig. 2, except that the spectrum has been convolved with a 3 m Å gaussian to simulate finite experimental resolution.

Fig. 4 Silicon plasma spectrum calculated to arise from the same plasma modeled in Fig. 2, except that a temperature decrement (described in the text) has been applied.

Fig. 5 Same as Fig. 4, except that the spectrum has been convolved with a 3 m Å gaussian to simulate finite experimental resolution.

Fig. 6 High dispersion spectrum of the Al XII principal resonance and intercombination lines obtained from Maxwell Laboratories' shot 159.

Fig. 7 Computed spectrum which would be emitted by a 1 mm diameter Al plasma of ion density 8×10^{18} cm^{-3}. The temperature profile is as described in the text. The implosion velocity is assumed to be 2×10^6 cm sec^{-1}. No experimental gaussian convolution was performed.

Fig. 8 Same as Fig. 7, except 2 m Å experimental broadening is assumed.

Fig. 9 Same as Fig. 7, except 3 m Å experimental broadening is assumed.

Fig. 10 Same as Fig. 9, except a zero implosion velocity for the plasma is assumed.

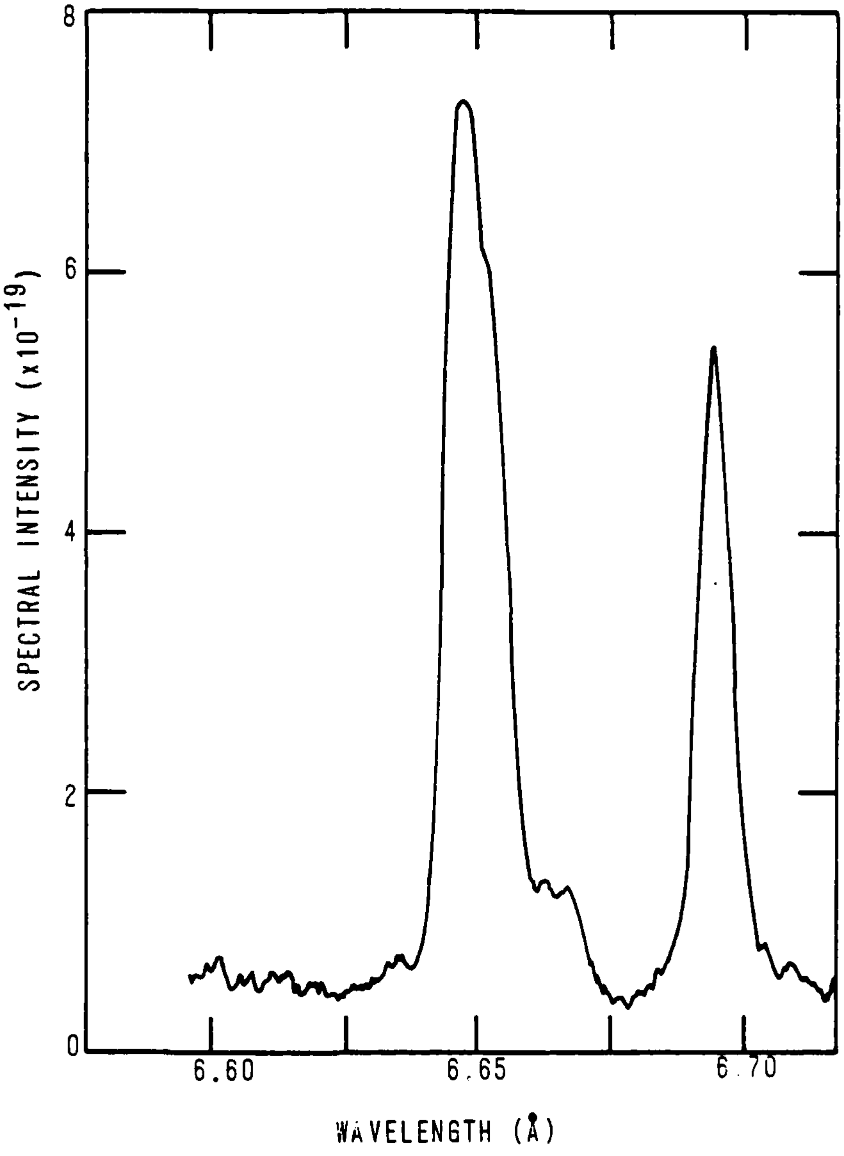

Figure 1

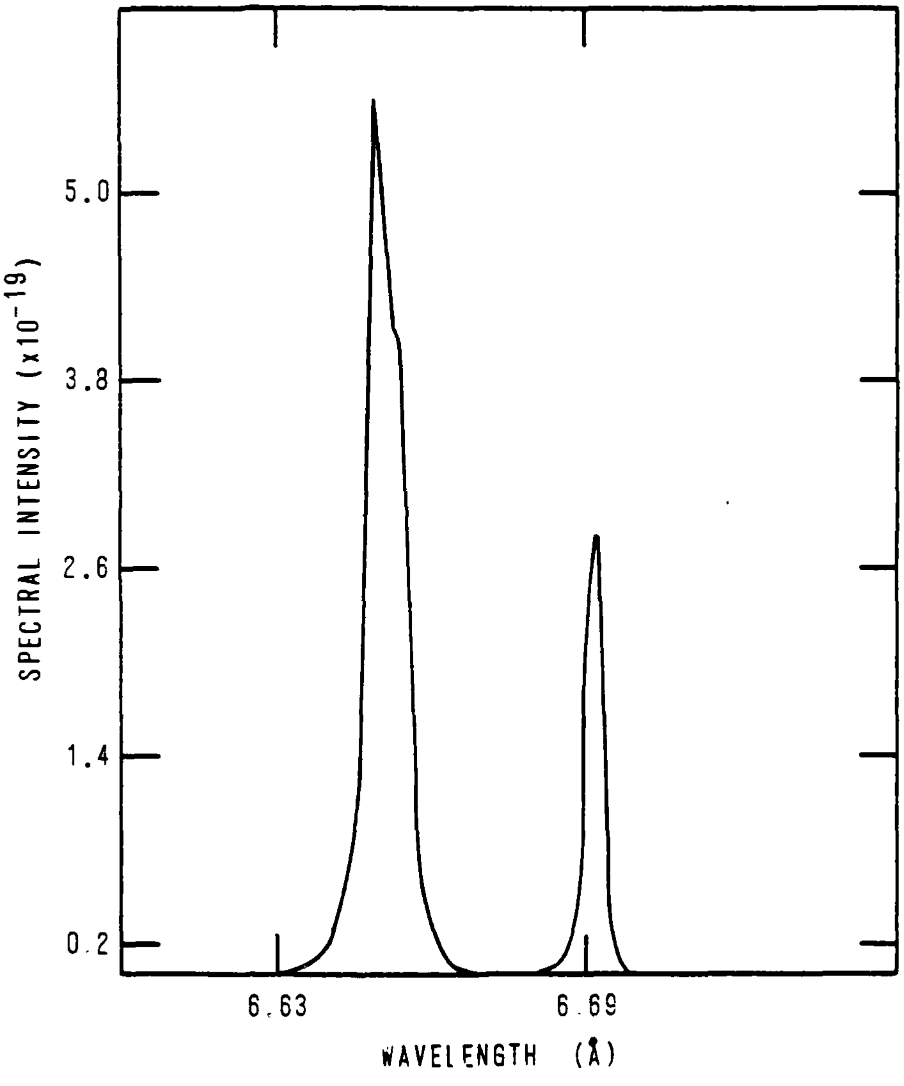
SPECTRAL INTENSITY ($\times 10^{-19}$)
5.0
3.8
2.6
1.4
0.2
6.63
6.69
WAVELENGTH (Å)

Figure 2

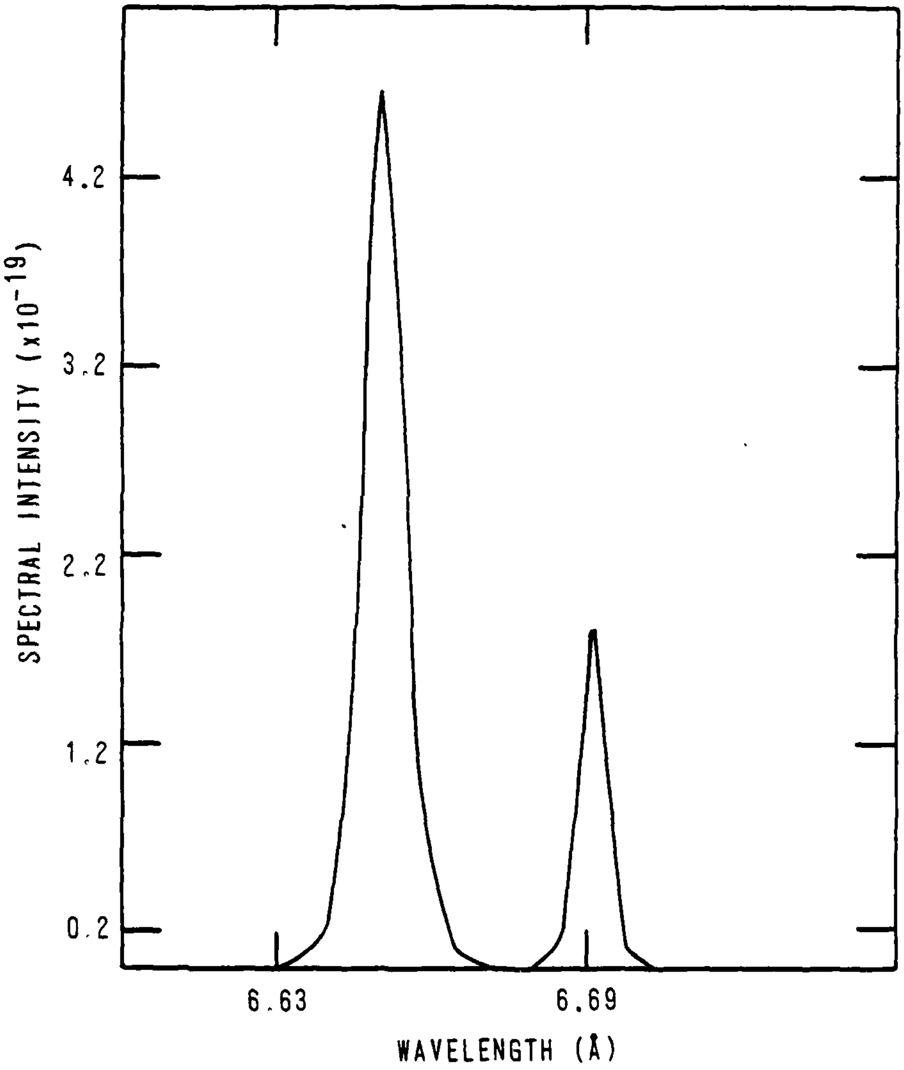

Figure 3

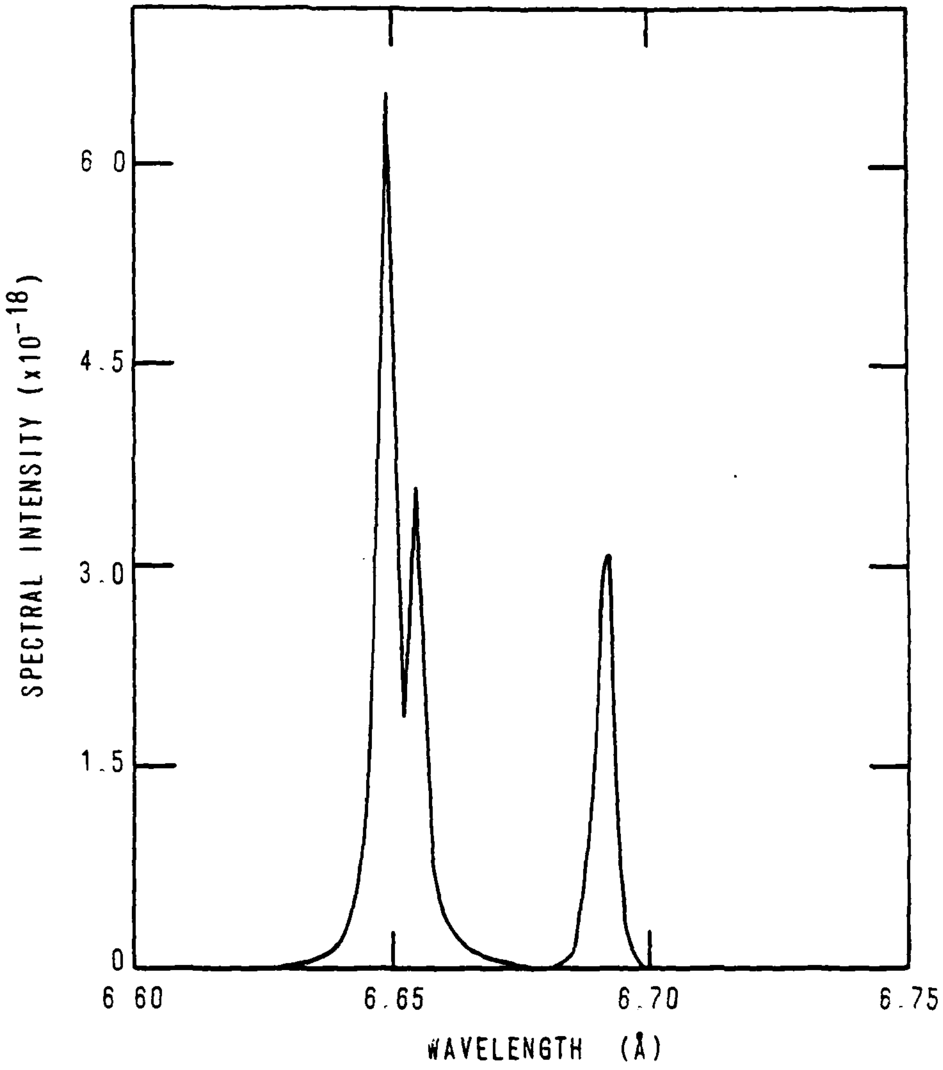
6.0
4.5
3.0
1.5
0
SPECTRAL INTENSITY (x10^-18)
6.60
6.65
6.70
6.75
WAVELENGTH (Å)

Figure 4

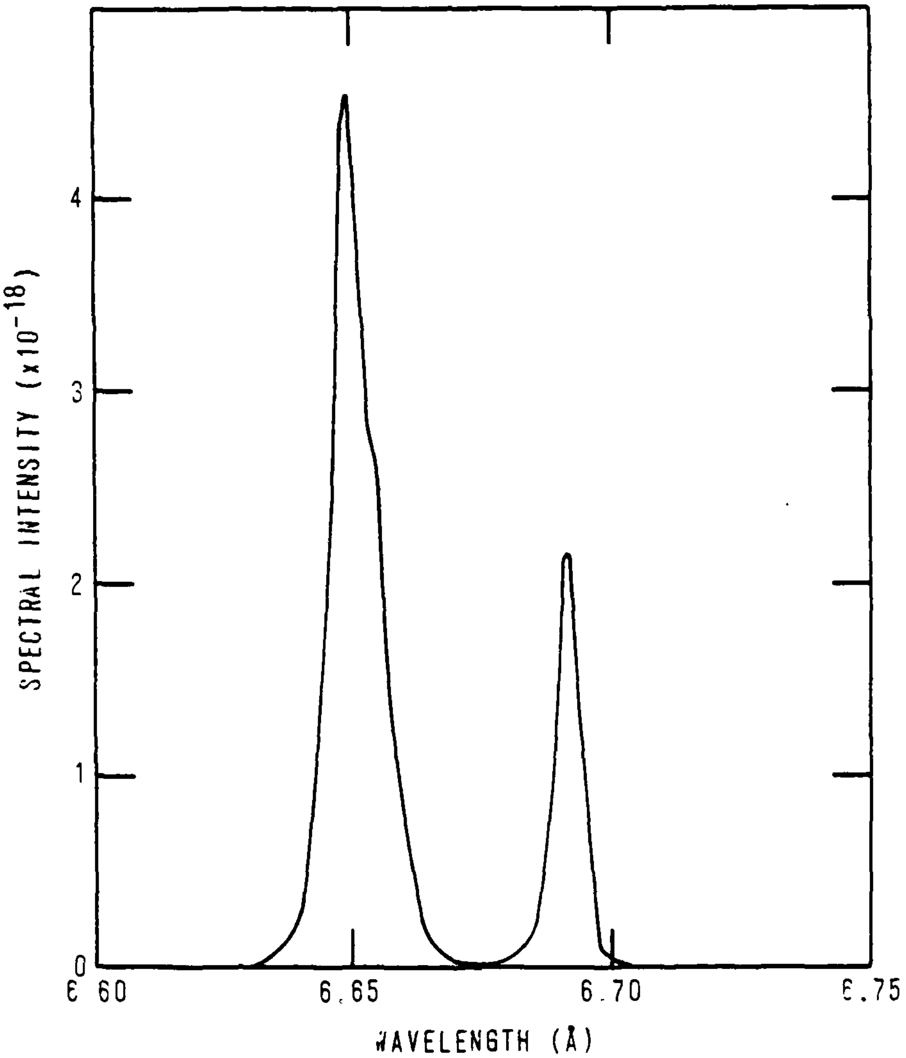

SPECTRAL INTENSITY (x10⁻¹⁸)
4
3
2
1
0
6.60
6.65
6.70
6.75
WAVELENGTH (Å)

Figure 5

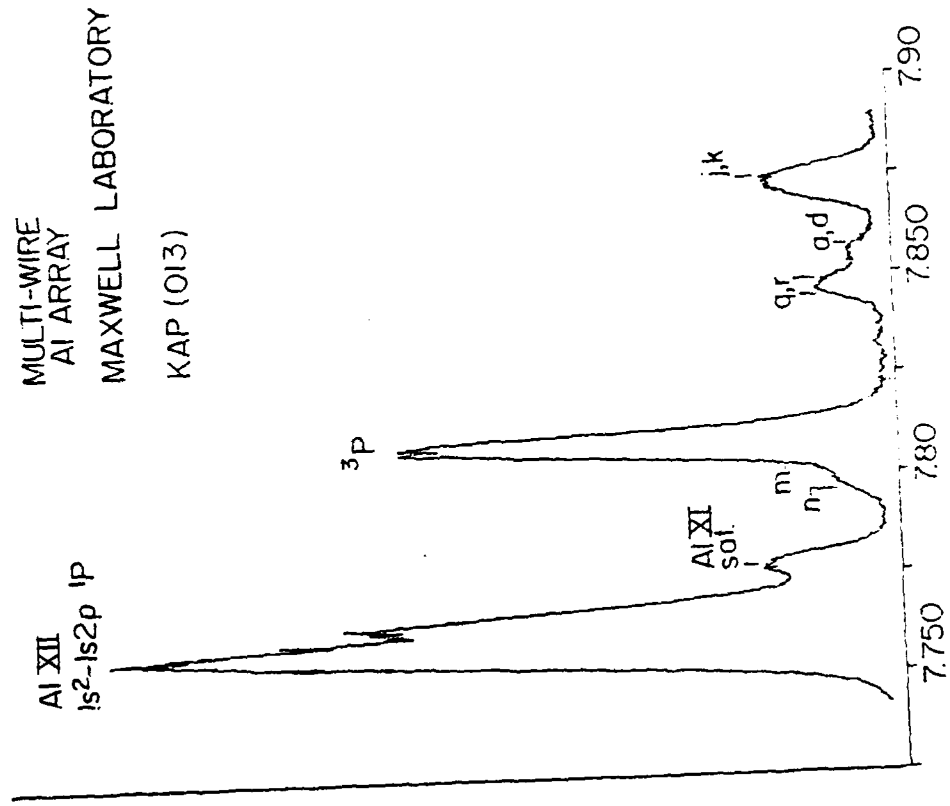
MULTI-WIRE
Al ARRAY
MAXWELL LABORATORY
KAP (013)
Al XII
$1s^2$-$1s2p$ ^1P
Al XI
sat.
^3P
m
n
q,r
a,d
j,k
7.750
7.80
7.850
7.90
ANGSTROMS

Figure 6

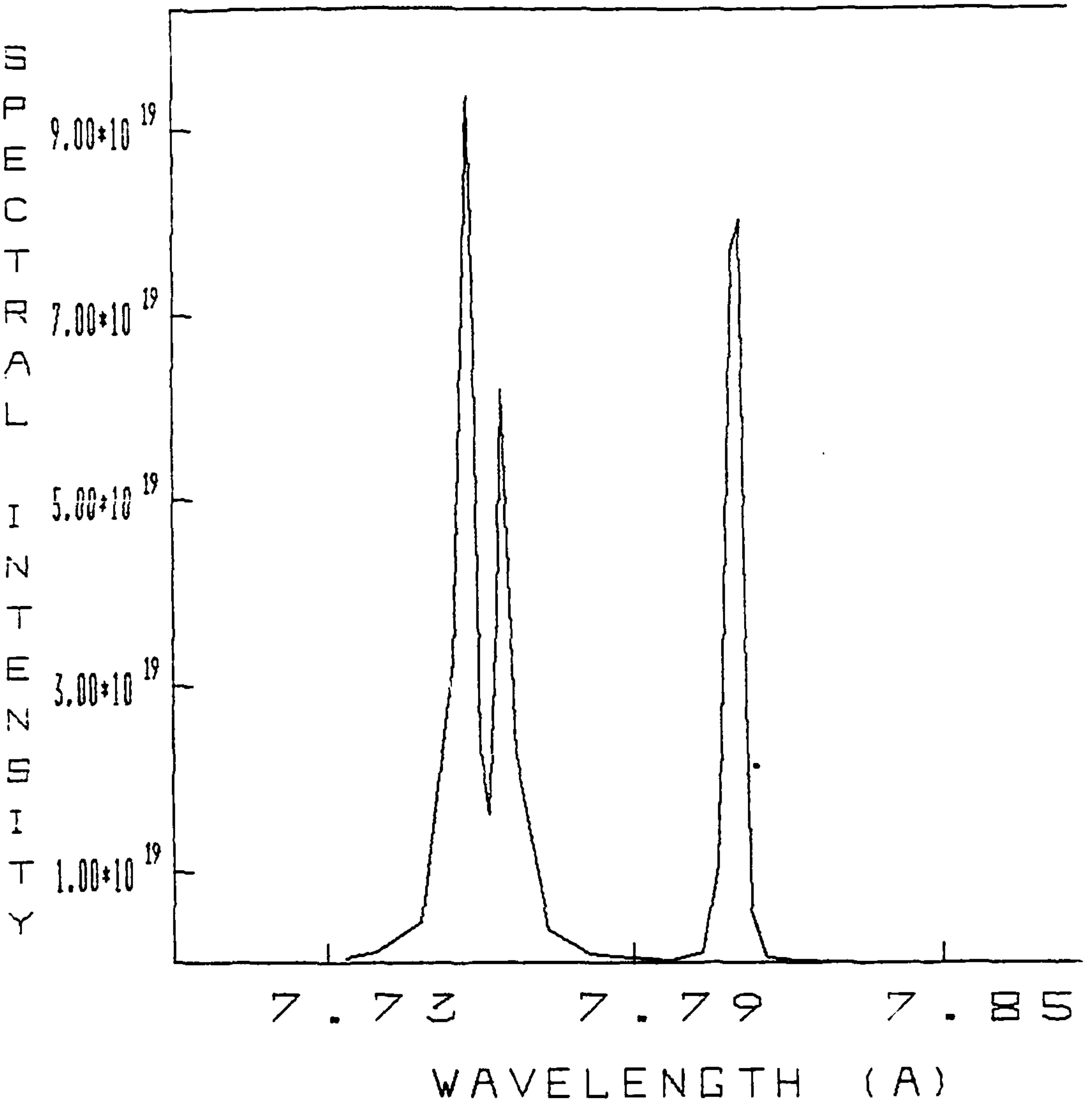

SPECTRAL INTENSITY
9.00*10 19
7.00*10 19
5.00*10 19
3.00*10 19
1.00*10 19
7.73
7.79
7.85
WAVELENGTH (A)

Figure 7

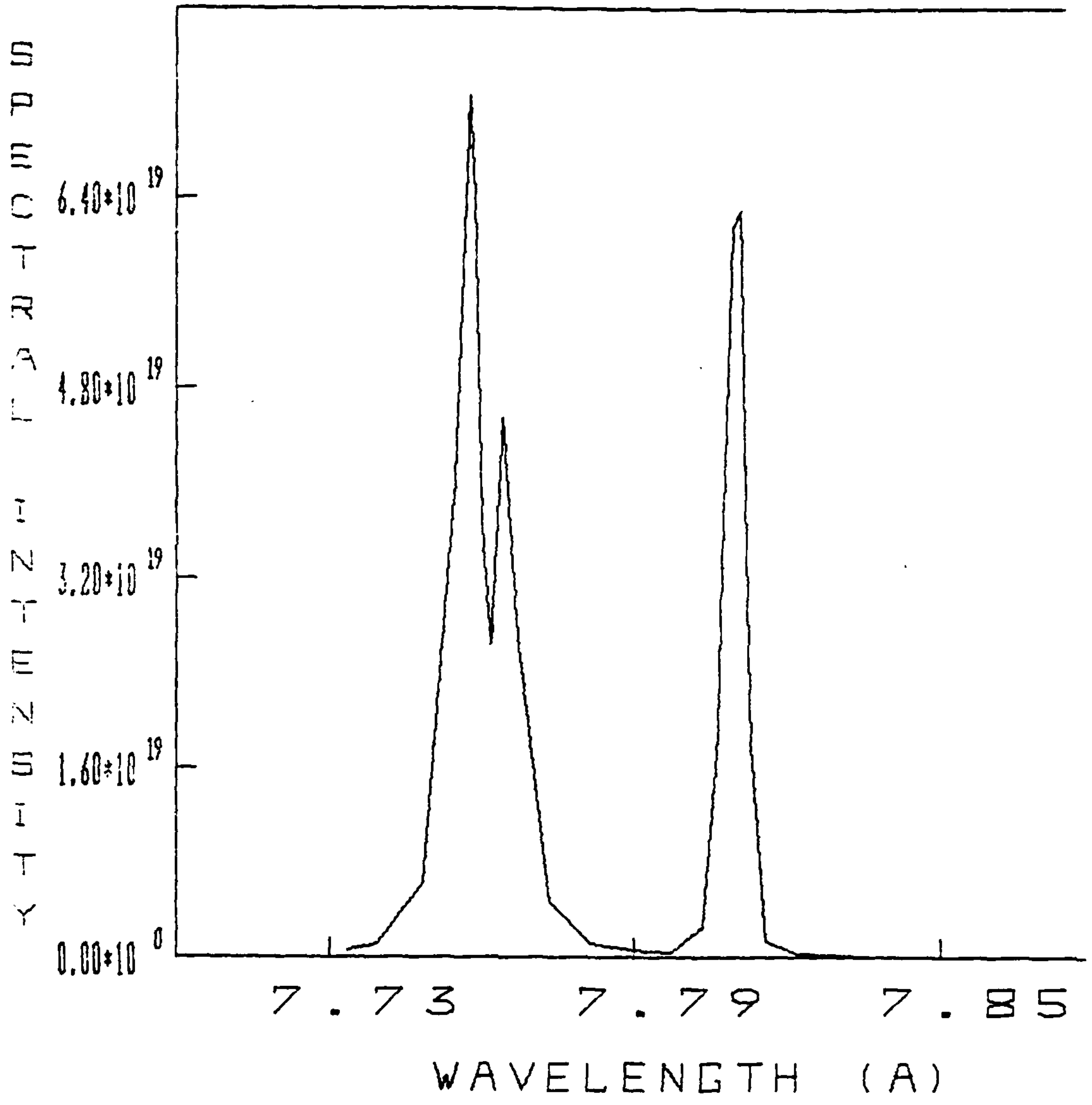
SPECTRAL INTENSITY
6.40*10^19
4.80*10^19
3.20*10^19
1.60*10^19
0.00*10^0
7.73
7.79
7.85
WAVELENGTH (A)

Figure 8

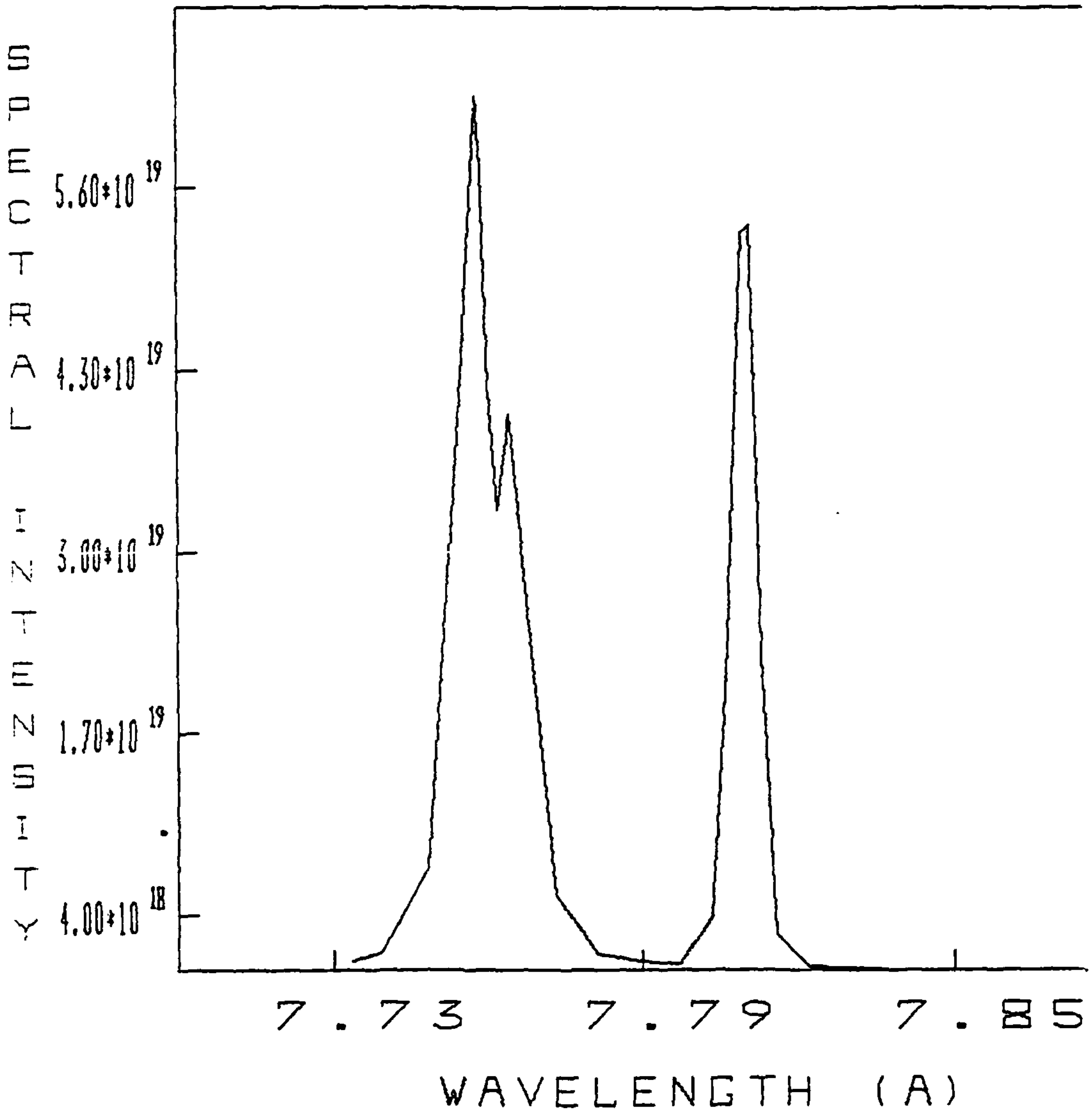
SPECTRAL INTENSITY
5.60*10^19
4.30*10^19
3.00*10^19
1.70*10^19
4.00*10^18
7.73
7.79
7.85
WAVELENGTH (A)

Figure 9

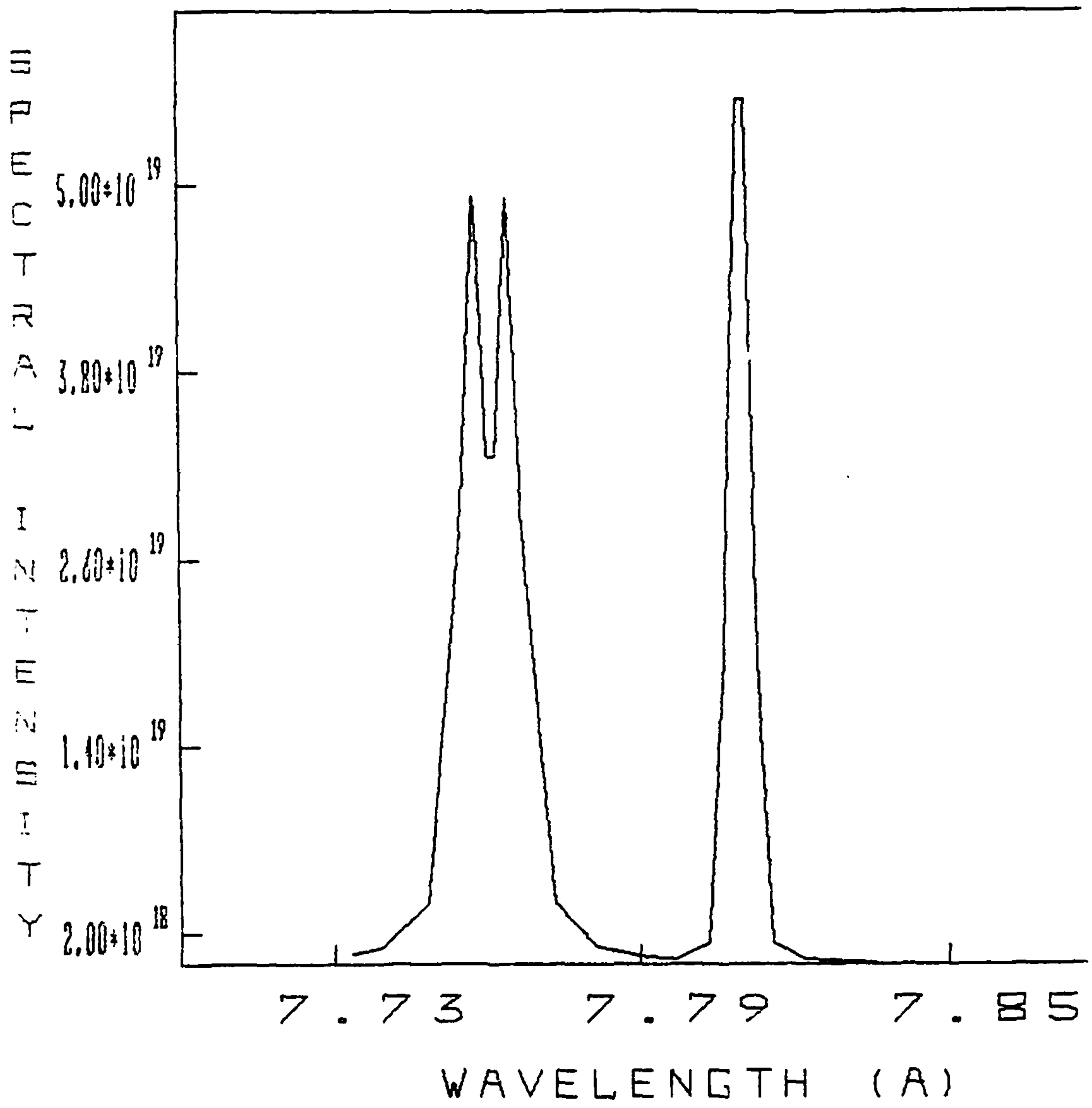
SPECTRAL INTENSITY
5.00*10^19
3.80*10^19
2.60*10^19
1.40*10^19
2.00*10^18
7.73
7.79
7.85
WAVELENGTH (A)

Figure 10

3. RADIATION HYDRODYNAMICS-COMPARATIVE TRANSIENT CALCULATIONS OF IMPLODING LOADS

Section 1

INTRODUCTION

It is generally accepted that cylindrical geometry is the most realistic simple geometry for modeling collapsing z-pinches. Substantial effort has been expended on the establishment of a 1-D radial collapsing z-pinch hydrodynamics code WHYRAD, which can model experiments initialized by wires, gas puffs or annular foils, employing a variety of ionization physics and radiation subroutines. This code is a significant improvement of an earlier model, WHYRAC.(1) A variety of initial radial distributions of particle number density and temperature, temporal variation of machine discharge voltage, and anomalous resistivity functions may be employed. Operational flexibility due to general re-start and improvement of computational vectorization was also incorporated. This report summarizes the analytical and numerical assumptions contained in the code development, illustrates subset benchmarks made to prove modeling adequacy, and applies the model to various aluminum and argon experimental conditions. Radiation yields and power are given in normalized magnitudes so as to maintain an unclassified status; direct yield values are given in a companion DNA final report which does not include some of the benchmark and test case development. Appendix D is also included in this unclassified version which documents the code structure by describing the function of the various subroutines.

Section II

PLASMA DYNAMIC MODEL

Analysis of the dynamics of a radiation coupled imploding z-pinch plasma depends on solutions of the time-dependent equations of mass, momentum, electron temperature and/or total internal energy, magnetic flux and the equations of state, as well as the specification of appropriate transport processes. The solution of the equations are linked, at every step and radial cell, to a radiative flux model in which both line and continuum emission and opacity are controlled by a probability of photon escape representation of cylindrical radiation transport solutions. Solution of these equations is also dependent on the coupling with the driving discharge circuit which in turn is altered by the changing plasma induction. The energy density of the plasma involves an adiabatic exponent containing the potential ionization energy; charge neutrality is also assumed.

The WHYRAD System solves the following fluid conservation equations:

$$\underline{\text{Mass}}: \quad \frac{\partial \rho}{\partial t} + \frac{1}{r}\frac{\partial}{\partial r}(r\rho v) = 0 \qquad (1)$$

Momentum:

$$\frac{\partial(\rho v)}{\partial t} + \frac{1}{r}\frac{\partial}{\partial r}\left(r\rho v^2\right) = -\frac{\partial P}{\partial r} - \frac{jB}{c} \qquad (2)$$

Total Internal Energy:

$$\frac{\partial E}{\partial t} + \frac{1}{r}\frac{\partial}{\partial r}\left\{r(E+p)v + rq_e\right\} = j\varepsilon + P_{RAD} \qquad (3)$$

Electron Temperature:

$$\frac{n_e}{\gamma - 1}\frac{\partial T_e}{\partial t} + \frac{n_e}{\gamma - 1} v \frac{\partial T_e}{\partial r} + \frac{1}{r}\left\{p_e \frac{\partial(rv)}{\partial r} + \frac{\partial(rq_e)}{\partial r}\right\} = Q_e + P_{RAD} \qquad (4)$$

Ion Temperature for Total Internal Energy Balance (optional):

$$kT_I = \frac{2}{3n_I}\left\{E - \frac{1}{2}\rho v^2 - \frac{n_e\, kT_e}{\gamma - 1}\right\} \qquad (5)$$

The dependent variables in the above conservation equations are ρ, plasma mixture density ($\approx$ ion density); v, radial plasma velocity; p, plasma pressure; j, axial current (z-direction); B, azimuthal (θ-direction) magnetic field; E, total plasma internal energy; ε, axial electric field; P_{RAD}, total radiative power; n_e, p_e, T_e, electron number density, pressure, and temperature, respectively.

Q_e and q_e are non-radiative thermal flux terms, given below. The adiabatic exponent, γ, which is a function of electron temperature, number density and ionization number {see Eq. (37)}, is assumed uniform over an individual spatial cell or time step such that its gradients are neglected. It is conceivably possible that a stable iterative solution, including the T_e, n_e, and Z_I gradients in the γ expression, within each cell and time step, may be constructed; however, D. Colombant (private communication) found in work with the WHYRAC code that numerical instabilities seemed to be quickly generated with this modeling. In addition, computational run times would rapidly increase so that practical considerations forced the abandonment of this refinement.

The Q_e term in Eq. (4) is given by

$$Q_e = j \left\{ \varepsilon - \frac{vB}{c} \right\} + \frac{3m_e}{m_I} \frac{n_e}{\tau_{eI}} \left\{ T_I - T_e \right\} , \qquad (6)$$

where τ_{eI} is the electron-ion equilibration time. For the general non-temperature equilibrated situation incorporation of the second term in Eq. (6) is performed by a subsequent T_e evaluation at the end of each time-step cycle, i.e., a solution of

$$\frac{\partial T_e}{\partial t} = \frac{3(\gamma - 1) m_e}{\tau_{eI} \, m_I} (T_I - T_e) . \qquad (7)$$

This relationship, Eq. (7), represents a common scheme employed in explicit convective hydrodynamic codes; certain flux terms have to be treated in a time-split manner and solved after the convective solution for T_e, so that one updating of T_e within a time step involves the separate solution of Eq. (7). A solution of Eq. (7) for T_e in terms of the explicitly-obtained T_e and the ion temperature T_I is given in Ref. 1; however, T_I values computed from Eq. (5) seem to be excessively high indicating that future calculations should employ a full two-temperature pair of energy equations including the equilibration term, Eq. (6). Almost all the solutions illustrated in this report assume equal electron and ion temperatures so that

$$Q_e = j \left\{ \varepsilon - \frac{vB}{c} \right\} . \tag{8}$$

The q_e electron thermal flux term is (ion thermal fluxes are neglected) given by:

$$q_e = - K_{e_\perp} \frac{\partial T_e}{\partial r} + \beta \left\{ \frac{BU_z}{|B|} \right\} \tag{9}$$

where $K_{e_\perp}$ and β are given by$^{(2)}$

$$K_{e_\perp} = \frac{n_e T_e \tau_e}{m_e} \frac{\gamma_1'(\omega_e\tau_e)^2 + \gamma_0'}{(\omega_e\tau_e)^4 + \delta_1(\omega_e\tau_e)^2 + \delta_0} \tag{9a}$$

$$\beta = n_e T_e \frac{\omega_e\tau_e\left\{\beta_1''(\omega_e\tau_e)^2 + \beta_0''\right\}}{(\omega_e\tau_e)^4 + \delta_1(\omega_e\tau_e)^2 + \delta_0} \tag{9b}$$

τ_e is given by Eq. (40a), which is employed equivalently to τ_{eI} in Ref. 2. The δ, γ', β'' coefficients are functions of Z_I, the average plasma ion number. Braginskii(2) gives their magnitudes at five Z_I values between 1 and → ∞: quadratic fits have been constructed which are within a few percent accuracy for $Z_I > 3$. The results are:

$$\delta_0 = 0.31652 - 0.01441\, Z_I + 2.2032 \times 10^{-4}\, Z_I^2$$

$$\delta_1 = 9.110 - 0.1360\, Z_I + 2.800 \times 10^{-3}\, Z_I^2$$

$$\beta_0'' = 1.282 - 0.0242\, Z_I + 3.600 \times 10^{-4}\, Z_I^2$$

$$\beta_1'' = 1.5$$

$$\gamma_0' = 3.350 - 0.17833\, Z_I + 3.667 \times 10^{-3}\, Z_I^2$$

$$\gamma_1' = 3.622 - 0.0222\, Z_I + 3.600 \times 10^{-4}\, Z_I^2$$

The axial current velocity (drift speed) is given by

$$U_z = -j/en_e\ . \tag{10}$$

Thermally perfect state expressions for electron pressure and total pressure and the charge neutral plasma electron density are given by

$$P_e = n_e \, k \, T_e \tag{11a}$$

$$P = (n_e k T_e + n_I k T_I) \tag{11b}$$

$$n_e = n_I \, Z_I . \tag{11c}$$

Also, $$n_I \simeq \rho / m_I . \tag{11d}$$

Equations (1) through (4), not including the $r^{-1}\partial(rK_{e\perp}\partial T_e/\partial r)/\partial r$ thermal diffusion and the temperature equilibration terms, are solved by the explicit Flux-Corrected-Transport algorithm ETBFCT.$^{(3)}$ The plasma is allowed to flow between the individual cells, but the outer boundary of the grid conforms to the displacement specified by a mean velocity over the high density cells, over that time step. The details of the outer boundary displacement and other aspects of the rezoning algorithm are given at the end of this section. The FCT method solves a general continuity relation of the form

$$\frac{\partial\psi}{\partial t} = - \frac{1}{r} \frac{\partial}{\partial r} (r\psi v) + \frac{1}{r} \frac{\partial}{\partial r} (rD_1) + c_2 \frac{\partial D_2}{\partial r} + D_3 , \tag{12}$$

where the last three terms on the right hand side would model a variety of source function representations. The algorithm is basically an improvement of the Lax-Wendroff technique whereby strong shocks or high fluid gradients are preserved and appropriately convected through the fluid. It adds a diffusion term during convective transport, and subtracts it out over most of the flow field in the antidiffusive phase (second half) of each time step. Any residual diffusion is sufficient to prevent dispersive ripples, and ensure positivity of the fluid density function ι. The ETBFCT algorithm is not restricted to a strict fixed grid Eulerian setup or uniform cell widths, so no basic coding difficulty is present, although too large a change of the mesh over a time step will destroy the accuracy of the algorithm. Equations (1) through (4) have convective densities of ρ, ρv, E, and T_e while the source terms describing pressure gradient, Lorentz force, Joule heating, radiation transport, and magnetic field dependent thermal fluxes fit into the above forms.

Incorporation of the $\kappa_{e_\perp} \partial T_e / \partial r$ part of the thermal conductivity is also by a time-split evaluation at the end of each time-step cycle, i.e., after successive calculations of T_e employing convective FCT and electron-ion equilibration (when desired), then the thermal diffusion influenced T_e is obtained by fully implicit solution of

$$\frac{\partial(\delta T_e)}{\partial t} = \frac{(\gamma - 1)}{n_e} \frac{1}{r} \frac{\partial}{\partial r} \left\{ r \, \kappa_{e_\perp} \frac{\partial(\delta T_e)}{\partial r} \right\}$$

using a tridiagonal method. Here δT_e is the addition to the FCT and equilibration results. Comparison of Eqs. (3) and (4) show that the related internal energy change is given as

$$\delta E = \left\{ n_e / (\gamma - 1) \right\} \quad \delta(k\ T_e)$$

(with T_e in eV and E in erg/cm^3). As indicated previously, the adiabatic exponent is assumed uniform over a cell and time step such that gradients of its functional dependency on T_e, n_e and Z_i are neglected. This assumption facilitates the above proportionality between δE and δT_e although it is an approximation.

Before considering the boundary conditions on these conservation equations it is necessary to specify the magnetic flux induction equation. The $\partial \underset{\sim}{B}/\partial t = -c\nabla \times \underset{\sim}{\varepsilon}$ Faraday equation is combined with a generalized Ohm's law relating the electric field to electric current, Lorentz force, pressure and temperature gradient contributions. It is assumed that the induced field is represented by

$$\frac{\partial B}{\partial t} = - \frac{\partial}{\partial r} (vB) + \frac{c^2}{4\pi} \frac{\partial}{\partial r} \left\{ \frac{\eta}{r} \frac{\partial (rB)}{\partial r} \right\} + \frac{c}{e} \frac{\partial}{\partial r} \left\{ \frac{\beta}{n_e} \frac{\partial T_e}{\partial r} \right\} \tag{13}$$

where the last two terms incorporate magnetic flux and thermal diffusion contribution. The function η is an assumed resistivity. Solution of this relation is also by a fully implicit tridiagonal algorithm due to B-field propagation swiftness with non-zero values of η. The T_e distribution used in Eq. (13) is the result from the previous time step as the B field has to be computed prior to the hydrodynamic conservation equations; as no back and forth iteration solution between B and T_e was attempted it was deemed necessary to incorporate a more stringent time step criteria employing a restrictive change to the total internal energy, Eq. (25d). Iterative close coupling between T_e and B, to ensure that they propagate exactly together is desirable but the computational time penalty for large cell number hydrodynamics was not considered warranted for either WHYRAC or WHYRAD.

The boundary conditions on the system of equations are (R is the outer boundary of the implosion):

$$\left.\frac{\partial \rho}{\partial r}\right|_R = \left.\frac{\partial \rho}{\partial r}\right|_0 = 0 \tag{14a}$$

$$\left.\frac{\partial (\rho v)}{\partial r}\right|_R = 0 , \quad \left.(\rho v)\right|_0 = 0 \tag{14b}$$

$$\left.\frac{\partial E}{\partial r}\right|_R = \left.\frac{\partial E}{\partial r}\right|_0 = 0 \tag{14c}$$

$$\left.\frac{\partial T_e}{\partial r}\right|_R = \left.\frac{\partial T_e}{\partial r}\right|_0 = 0 \tag{14d}$$

$$B|_0 = 0 \ , \ B|_R = \frac{2I(t)}{Rc} \ . \tag{14e}$$

Establishment of the radially integrated total discharge current I(t) yields the outer boundary condition on the B field, leading to its solution and the specification of the Lorentz force and Joule heating source functions. Therefore, appropriate coupling into the external driving circuit is crucial; denoting the external circuit impedance by Z_g, inductance by L_g, driving voltage by $V_g(t)$ and effective voltage across the plasma by $V_p(t)$ we have that

$$\frac{dI}{dt} + \left(\frac{Z_g}{L_g}\right) I = \frac{V_g(t) - V_p(t)}{L_g} \ . \tag{15}$$

$V_p(t)$ is obtained by integration of

$$\nabla \times \underset{\sim}{\mathcal{E}} = -(1/c)(\partial \underset{\sim}{B}/\partial t) \tag{16}$$

or $$\frac{\partial \mathcal{E}}{\partial r} = \frac{1}{c}\frac{\partial B}{\partial t} \tag{16a}$$

across a loop along a perfectly conducting outer shell {at a radius $r_w >> R(t)$} and cathode end plate, through the plasma at a general radius r, and across the V_p voltage drop at one end of the discharge (see Figure 1). The axial integral of the electric field is determined from the generalized Ohm's law

$$\underset{\sim}{\varepsilon} = - \frac{\underset{\sim}{v} \times \underset{\sim}{B}}{c} - \frac{1}{n_e e} \left\{ \begin{array}{l} \nabla P_e - \dfrac{m_e Z_I}{m_I} \nabla P_I + \beta_\perp \nabla_\perp T_e \\ \\ + \beta \dfrac{\underset{\sim}{B}}{B} \times \nabla T_e - \dfrac{\underset{\sim}{j} \times \underset{\sim}{B}}{c} \end{array} \right\} + \eta \underset{\sim}{j} \ . \quad (17)$$

The axial integral of Eq. (17) is

$$\int_0^L \varepsilon dz = - \frac{v(r)B(r)}{c} L - \frac{L\beta \ \nabla T_e}{n_e e} - \eta(r)j(r)L \ . \qquad (18)$$

Insertion of Eq. (18) into the axial integration of Eq. (16a) over z between o and L gives

$$\frac{\partial}{\partial r} \left\{ - \frac{v(r)B(r)L}{c} - \frac{L\beta}{n_e e} \nabla T_e - \eta(r)j(r)L \right\} = \frac{L}{c} \frac{\partial B}{\partial t} \ . \qquad (19)$$

Integrating Eq. (19) over r from 0 to r gives

$$V_p(r,t) = - \frac{v(r)B(r)L}{c} - \frac{L\beta}{n_e e} \nabla T_e + \eta(r)j(r)L \qquad (20a)$$

$$+ \frac{L}{c} \int_r^{r_w} \frac{\partial B(r',t)}{\partial t} dr' \ ,$$

where V_p, the plasma voltage, is

$$V_p(r,t) = \eta(o)j(o)L + \frac{L}{c}\int_{o}^{r=r_w} \frac{\partial B}{\partial t}\, dr' \ . \qquad (20b)$$

Here r_w is the outer radial location of the perfectly conducting return current. The function $V_p(r,t)$ can equivalently be written as

$$V_p(r,t) = \varepsilon(r)L + \frac{L}{c}\int_{r}^{r_w} \frac{\partial B}{\partial t}\, dr' \ , \qquad (20c)$$

where the local electric field is

$$\varepsilon(r) = \eta(o)j(o) + \frac{1}{c}\int_{o}^{r} \frac{\partial B}{\partial t}\, dr' \ . \qquad (20d)$$

This expression for ε is consistent with a radial integration of the Faraday law, Eq. (16a), together with use of Eq. (17) at $r = 0$ and the $B|_{r=0} = 0$ boundary condition. Equation (20c) is a representation of the plasma voltage around the loop in Fig. 1. The major electrodyanmic assumption in the WHYRAC(1) model, and retained with some misgivings in the WHYRAD code, is that a single value of r, at the cell location where the current stops flowing for the previous time step ($r = R$), is employed to calculate V_p. Then Eq. (20c), can be solved to give

$$V_p(R,t) = \varepsilon^0(R)L - \frac{2L}{c^2}\left(\frac{dI}{dt}\right)\ln\left(\frac{r_w}{R}\right) \qquad (21)$$

with employment of $B|_R = 2I/Rc$ so that

$$\left.\frac{\partial B}{\partial t}\right|_R \simeq \frac{2}{rc}\frac{dI}{dt} .$$

$\varepsilon^0(R)$ is Eq. (17) evaluated at $r = R$ and at the previous time step,

$$\varepsilon^0(R) = -\frac{v(R)B(R)}{c} - \left(\frac{\varepsilon}{n_e e}\frac{\partial T_e}{\partial r}\right)_{r=R} \qquad (22)$$

with the current cutoff at $r = R$. It was originally considered in Ref. 1 to directly employ Eq. (17) in the calculation of $\varepsilon(r)$ for all r (not just at $r = R$). However, the resulting field was very choppy due to the influence of large variations of velocity, number density, and temperature. The best way to calculate $\varepsilon(r)$ is from direct radial integration of the Faraday law, Eq. (16a), after specification of the B-field (Eq. 20d). Insertion of Eq. (21) into Eq. (15) gives

$$\frac{dI}{dt}\left\{1 - \frac{2L}{L_g c^2}\ln\left(\frac{r_w}{R}\right)\right\} + I\left(\frac{R_g}{L_g}\right) = \frac{V_g(t)}{L_g} - \frac{L\varepsilon^0(R)}{L_g} \qquad (23)$$

which is numerically integrated in time to specify the total current and the outer boundary condition on the B field.

The local current is obtained from the Maxwell law in the MHD approximation

$$j = \frac{1}{4\pi}\,\frac{1}{r}\,\frac{\partial}{\partial r}\,(rB) \tag{24}$$

which is solved by a central finite difference representation of the gradient; as indicated above the ε field distribution is then obtained by employment of Eq. (20d). The electromagnetic field dependent source terms in the hydrodynamic equations are therefore determined.

Time step criteria is evaluated from the cell-dependent minimum of the following relations.

Courant:

$$\delta t^{C} = \min\left\{\frac{0.4\ \Delta r}{C_s + |v|}\right\},\quad C_s \equiv \sqrt{\frac{\gamma P}{\rho}} \tag{25a}$$

Joule Heating Energy Transfer:

$$\delta t^{J} = \min\left\{\frac{0.4 \times \max[n_e kT_e,\ 0.05E]}{(\gamma - 1)\,\varepsilon j}\right\} \tag{25b}$$

Radiative Energy Transfer:

$$\delta t^R = \min \left\{ \frac{0.4 \times \max[n_e kT_e,\ 0.05E]}{(\gamma-1)\ P_{RAD}} \right\} \qquad (25c)$$

Previous Time Step Internal Energy Change:

$$\delta t^{k-1}_{\Delta E} = \min \left\{ \frac{0.4 \times \max[n_e kT_e,\ 0.05E]}{|(E^k - E^{k-1})/\delta t^k|} \right\} . \qquad (25d)$$

Direct incorporation of the Alfven speed, $C_A = \sqrt{B^2/4\pi\rho}$, into a time step criterion such as Eq. (25a) is unwise as the presence of a large B field together with a low density in the outer regions of the implosion yields excessively small time steps. In this situation the time steps are chosen at a location which is far removed from the high density, high radiative regions of interest. The WHYRAC scheme of Ref. 1 is retained, whereby a term $B^2/4\pi(C^*_A)^2$ is added to the inertia in the low density region. C^*_A is an effective Alfven speed of reduced magnitude determined from the assumptions that

$$\delta t^A = \min \left\{ \frac{0.5\ \Delta r}{C_A} \right\} \qquad (25e)$$

together with, if $\delta t^A < \delta t$ from the other time step criteria,

$$C^*_A = 2.5\ \delta r(r=0)/\delta t\ .$$

This C_A^* ensures that the Alfven time scale is no faster than the hydrodynamic time scale. Even though this effect of the Alfven speed is included in the formalism it was decided in the construction of WHYRAD to include the internal energy change criteria, Eq. (25d), in addition to the first three criteria, thus practically yielding a significantly finer time step resolution. This last criteria was not included in WHYRAC. The absolute minimum over all the cells of the four functions, Eqs. (25a) through (25d) is selected, with time steps of 20% to 50% of the minimum Courant value normally computed.

For no rezoning the spatial increment widths are an assigned fraction of the total beam radius R, defined by (R ≡ RADR)

$$\mathrm{RADR} = \mathrm{RADRO} + \mathrm{VGM} \times \delta t^{1/2} \qquad (26)$$

where RADRO is the old, previous time step value of the total radius, $\delta t^{1/2}$ is the half time step (ETBFCT is applied twice successively over a full time step) and VGM is a velocity given by

$$\mathrm{VGM} = \left(\sum_{i=1}^{n} v_i \right) / N_X \qquad (26a)$$

where i is the cell number, N_N is the number of cells in the summation, and v_i is the individual cell velocity. The summation is not carried out over all cells, but only over those cells with a density at least 10% of the maximum density, which gives a weighting to the cells with maximum mass flux in the evaluation of the beam contraction.

A density-dependent rezoning option is also present in the code which assigns the minimum cell width at the maximum density and vica versa, thus increasing the cell density at regions of maximum radiation yield. With no rezoning

$$\Delta r_i = \mathrm{RADR}/\mathrm{NR} \equiv R/\mathrm{NR} \qquad (26b)$$

where NR is the total number of cells. Although more detailed consideration of the required cell number is given later in this report it should be noted that around 40 should be the minimum number to represent the j current and B field radial distributions. The rezoning option uses Eq. (26b) to define a representative uniform cell,

$$\Delta r^o = \mathrm{RADR}/\mathrm{NR} \ , \qquad (27a)$$

together with an average number density given by

$$n^o = \left\{ \sum_{i=1}^{\mathrm{NR}} (\Delta r_i \times n_i)_{t-\Delta t} \right\} / \mathrm{RADR} \ . \qquad (27b)$$

Then the rezoning is dictated by

$$\Delta r_i^* = \Delta r^o (n^o/n_i)^M , \qquad (27c)$$

where the power M, to be careful, should be << 1. Now.

$$\sum_{i=1}^{NR} \Delta r_i^* = \text{RADNEW}$$

which is not necessarily the same as RADR, previously obtained. Therefore, the Δr_i's are rescaled by

$$\Delta r_i = \Delta r_i^* \times (\text{RADR}/\text{RADNEW}) \qquad (27d)$$

which is the chosen rezoned cell width. In either cell distribution algorithm the cell-center locations are determined from

$$r_1 = 0.5\, \Delta r_1 \qquad (28a)$$

and $r_i = r_{i-1} + 0.5(\Delta r_i + \Delta r_{i-1})$, $i > 1$. (28b)

It is necessary to constrain the M power in Eq. (27c) to prevent rezoning-induced numerical instabilities. The function employed is

$$M = M^o \{1 - \exp [-D]\} \qquad (29)$$

where $D = \min \left\{ \frac{b}{|\delta \ln n^o|} , \frac{c}{1 - RE} \right\}$ (29a) the b and c coefficients have been determined, by numerical experimentation, to be of order 10^{-2}, $|\delta \ell n\, n^{o}|$ refers to the absolute value of the change, over a time step, of the logarithm of the average number density given by Eq. (27b), and RE is a function of the local energy balance ratio. Although more will be said later, an M^{o} value of 0.03-0.05 was employed in test cases. The energy balance ratio is the plasma internal energy at $t = 0$ plus the electromagnetic energy added up to the time in question minus magnetic field, emitted radiation and boundary flux energies, all divided by the plasma internal energy at that time. For complete energy balance this ratio should be unity. For the ratio > 1, RE = 1/ratio, for the ratio < 1, RE = ratio, while for complete energy balance the contribution of the second term in Eq. (29a) is neglected. The two damping contributions found in Eq. (29a) control the effects of the sudden number density and energy balance changes on the rezoning algorithm.

Section III

RADIATION, IONIZATION AND TRANSPORT PROCESSES

Three separate radiation-ionization packages have been employed in the implosion solutions; the first one is ATPHYS, a relatively simple ground plus one excited state ion balance with approximate radiation transport, TERRYS, a curve fit representation of the ionization-radiation package MCELL solutions with radiation transport assumed to be a double path probability of escape function out of the plasma volume from each individual radiating cell, and real time application of MCELL. MCELL is an ionization collisional-radiative equilibrium package which solves for the ground and excited state population densities; line, radiation recombination and Bremsstrahlung radiation transport are modeled with emission and absorption balanced out over the multi-cell radiation increment zones.

The ATPHYS modeling of argon was useful to establish the scheme of running the code, remove the numerous bugs and hardwired quantities present in the original WHYRAD source deck, and incorporate a number of the features of the WHYRAD development. No numerical results from ATPHYS calculations will be presented in this report, however. Real time employment of MCELL was the original intent of the computations; however, calculations with a many-line spectra aluminum model showed that in some cases 98% of the run time per time step was taken up by the radiation-ionization package and only 2% by the remaining hydro-induced B field-driving circuit algorithm. Even though this setup probably represents the ideal modeling of the nonequilibrium coupled hydrodynamic-radiation scheme, it was felt that running costs as well as an excessive number of restart inputs over a typical 3000 time step case prevents the present implementation of the full real time scheme. It is suggested that an energetically optimum MCELL code, tailored to run 10 times faster, would facilitate this highly desirable direct coupling. Nevertheless, post-processing at discrete time steps, using the full MCELL package, is useful and results are illustrated in section V.

The TERRYS radiation-ionization package utilizes R. Terry(4) curve fits to D. Duston's MCELL computed optically thin volume emission rates for aluminum or argon.(5,6) The radiation is divided into the categories of line L-shell with $h\nu < 1$ keV, line K-shell with $h\nu > 1$ keV, free bound continuum and free-free Bremsstrahlung continuum radiation. The optically thin line and free-bound emissions are fitted to the following functional relation:

$$P^{OT}(n_I^o, T_e) = \exp\left\{\sum_{k=1}^{M} b_k \left[\ln(T_e/N)\right]^{k-1}\right\} \quad \left(\frac{erg}{cm^3 sec}\right) \qquad (30)$$

where (for Aℓ) $N = 0.3$, $M = 16$ for L-shell line, $N = 0.7$, $M = 16$ for K-shell line, and $N = 0.5$, $M = 16$ for bound-free radiation. Here n_I^o is a reference density of 10^{19} cm^{-3}; the fit of Eq. (30) to the multicell Aℓ is made at this density. The b_k coefficients are a tabulated data input within the code.

For other densities the scaling laws (Aℓ)

$$P^{OT}_{L\text{-shell}} \sim (n_I/10^{16})^{1.5} \qquad \text{for } n_I > 10^{16} \text{ cm}^{-3} ,$$

$$P^{OT}_{L\text{-shell}} \sim (n_I/10^{16})^{2} \qquad \text{for } n_I < 10^{16} \text{ cm}^{-3} ,$$

$$P^{OT}_{K\text{-shell}} \sim (n_I/10^{18})^{1.5} \qquad \text{for } n_I > 10^{18} \text{ cm}^{-3} ,$$

$$P^{OT}_{K\text{-shell}} \sim (n_I/10^{18})^{2} \qquad \text{for } n_I < 10^{18} \text{ cm}^{-3} ,$$

$$P^{OT}_{BF} \sim (n_I/10^{18})^{2} \qquad \text{for all } n_I$$

are employed.

Free-free Bremsstrahlung emission, with opacity, is evaluated by a ten frequency sum:

$$P_{FF} = \frac{1}{2} \sum_{j=1}^{10} \varepsilon_j \, (\Delta\nu)_j \left\{e^{-\tau_{s,j}} + e^{-\tau_{\ell,j}}\right\} \qquad (51)$$

where τ_s and τ_ℓ are short and long path optical depths, described below. The optically thin j frequency emission coefficient is

$$\varepsilon_j = 6.35 \times 10^{-40} T_e^{-1/2} Z_I^2 n_e n_I e^{-h\nu_j/kT_e} \qquad (31a)$$

and
$$\Delta\nu_j = \frac{1}{2} \left\{ (\nu_j - \nu_{j-1}) + (\nu_{j+1} - \nu_j) \right\} . \qquad (31b)$$

ν_j and $\Delta\nu_j$ are entered as a table for $10^{14} < \nu_j < 10^{19}$ Hz.

The j-frequency optical depth, for either path length, is given by, for emission at the i^{th} cell,

$$\tau_j = \int_{i_{cell}}^{Surface} k_{ij} \, d\ell \qquad (31c)$$

where $k_{ij} = 3.43 \times 10^6 \nu_j^{-3} T_{e,i}^{-1/2} Z_I^2 n_e n_I (1 - e^{-h\nu_j/kT_{e,i}})$ (31d)

is the absorption coefficient. In performing the τ_j integration the variability of T_e, n_e, n_I, and Z_I is accounted for along the path lengths by employment of the previous time step's solution parameters.

The short and long optical depth path integrations are carried out from the individual cell in two opposing directions to the boundary of the cylindrical plasma. The same idea in estimating opacity is also used for line and bound-free continuum transport:

$$\tau_i^{K,L,BF} = \int_{i\ \mathrm{cell}}^{\mathrm{Surface}} \sigma(T_e)\, n_i(\xi)\, d\xi\ , \qquad (32)$$

for either path length. The Doppler broadened cross section is used for line transport:

$$\sigma^{K,L} = 1.76 \times 10^{-13}\, \lambda \left(\frac{m_I c^2}{kT_e}\right)^{1/2} . \qquad (32a)$$

For K-shell radiation it is assumed that the wavelength is evaluated at a single value of 2.0 keV photons and for L-shell radiation it is assumed that 0.5 keV single wavelength emission is appropriate. Bound-free opacity is usually small for the conditions of interest; the cross section used is

$$\sigma_{BF} = 2 \times 10^{-17}\, e^{-f(Z_I)} \qquad (32b)$$

where $f(Z_I)$ is a polynomial function of the ion number: it has been determined by a fit to multi-cell input data.

The opacity of a cylindrical plasma affects the resulting net radiant emission by removal of photons prior to their escape through the plasma boundary. Probability of escape functions of optical depth are fits to solutions of the radiation transport equation(7,8) and are of good accuracy for cylindrical transport over a wide range of τ. The total loss from all radiant modes at each cell is then

$$P_{RAD} = P_{FF} + P_{BF}^{OT} \times \frac{1}{2} \left\{ P^{BF}(\tau_s) + P^{BF}(\tau_\ell) \right\}$$

$$+ P_K^{OT} \times \frac{1}{2} \left\{ P^K(\tau_s) + P^K(\tau_\ell) \right\} \qquad (33)$$

$$+ P_L^{OT} \times \frac{1}{2} \left\{ P^L(\tau_s) + P^L(\tau_\ell) \right\} \quad ,$$

where $P(\tau)$ are the probability of escape functions defined for bound-free radiation by the following (from R. Terry, private communication)

$$P_{s,\ell}^{BF} = 0.9027 \, \tau_{s,\ell}^{-2.3} \qquad \text{for } \tau^{BF} \geq 3.0 \ , \qquad (33a)$$

$$P_{s,\ell}^{BF} = (1.0 + 8.268 \times 10^{-3} \, \tau_{s,\ell})/(1.0 + 0.426 \, \tau) \qquad (33b)$$

$$\text{for } \tau^{BF} < 3.0 \ .$$

For line radiation the Doppler profile results of Ref. 8 (Appendix A) are utilized by R. Terry in the form

$$P_{s,\ell}^{K,L} = 1.0/\left\{1.0 + a[(1.0/\varepsilon) - 1.0]\right\} \qquad (33c)$$

with $a = n_I/(n_I + 10^{22})$ and

$$\varepsilon = 0.547/(\tau_{s,\ell}\sqrt{\ln \tau_{s,\ell}}) \qquad \text{for } \tau_{s,\ell} > 5.18 \ ,$$

$$\varepsilon = 1.0/(1.0 + \tau_{s,\ell}[0.29 \, \tau_{s,\ell} + 0.65])$$

$$\text{for } \tau_{s,\ell} \leq 5.18.$$

The ionization model utilizes the near-coronal model Shearer-Barnes(9) expression (T_e in eV)

$$Z_I = 26.0 \left\{ \frac{T_e/1000.0}{1 + (26.0/ZA)^2 (T_e/1000.0)} \right\}^{1/2} \qquad (34)$$

for the ionization number, where ZA is the element atomic number, while the internal electron energy, given by

$$E_e = \frac{3}{2} n_e k T_e + E_{TCP} \, . \qquad (35)$$

utilizes a hydrogenic assumption for the total chemical potential E_{TCP}, i.e.,

$$\begin{aligned} E_{TCP} &= n_I \sum_{i=1}^{Z_I} IP(Z_I) \simeq n_I \int_0^{Z_I} R_y Z_I'^2 \, dZ_I' \\ &= \frac{n_I}{3} R_y Z_I^3 \end{aligned} \qquad (36)$$

where R_y = 13.6 eV. The ionization level, given by Eq. (34), is accurate up to $n_I = 10^{20}$ cm^{-3} but should be close enough for densities perhaps a factor of 5 higher than this, covering the range of collapse conditions found in Blackjack III or V shots. The γ adiabatic exponent is defined in terms of the electron thermal plus ionization energy by

$$\gamma = 1 + \frac{n_e\ k\ T_e}{\frac{3}{2}\ n_e k T_e + E_{TCP}}\ . \qquad (37)$$

As stated in section II the adiabatic exponent is evaluated from the temperature and ionization number locally at each spatial cell and timestep for utilization in the conservation of electron temperature and total internal energy equations; the possible influence of spatial and temporal gradients of γ evaluated from the respective T_e and Z_I gradients is not taken into account.

Most of the computations illustrated in this report assume microscopic classical transport processes although some consideration is given to anomalous transport, especially resistivity. The classical resistivity is(10)

$$\eta^{C\ell} = 1.15 \times 10^{-14}\ Z_I\ T_e^{-3/2}\ \ln\Lambda \quad \text{(sec)} \qquad (38)$$

where(2)

$$\ln\Lambda = 23.4 - 1.15\ \log_{10}(n_e) + 3.45\ \log_{10}(T_e)$$

$$\text{for } T_e \leq 50 \text{ eV}\ ,$$

$$\ln\Lambda = 25.3 - 1.15\ \log_{10}(n_e) + 2.3\ \log_{10}(T_e)$$

$$\text{for } T_e > 50 \text{ eV}\ .$$

Initial implementation of anomalous resistivity in the WHYRAC code assumed that non-classical effects could be represented by a radially uniform multiplier of $\eta^{c\ell}$ (11); it would seem to be better to introduce a multiplier that attains its maximum value in the outer low density coronal region of the implosion and approaches unity near the relatively high density pinch center. The approach is nevertheless highly empirical and qualitative. The function chosen is

$$\eta^{an} = \eta^{c\ell}\left\{1.0 + g(t)(r/R)^2\right\} \tag{39}$$

with a g(t) growth factor of

$$g(t) = A(t/t_{pulse})^B \ . \tag{39a}$$

A and B are empirical coefficients and t_{pulse} is the total pulse time. The core limit of $\eta^{an} \rightarrow \eta^{c\ell}$ as $r \rightarrow 0$ is maintained as well as the initial condition $\eta^{an} \rightarrow \eta^{c\ell}$ as $t \rightarrow 0$ for any r.

A. Mondelli has incorporated a plasma instability model due to Sagdeev for the calculation of anomalous processes within the WHYRAD code; it represents resistivity, $\omega\tau$, and $K_{e\perp}$ in terms of an anomalous collision time τ_{eI}^{an}. In this formulation

$$\eta^{an} = m_e/(e^2\ n_e\ \tau_{el}^{an}) \tag{40}$$

where τ_{eI}^{an} is the classical value(10)

$$\tau_{eI}^{c\ell} = 3.44 \times 10^5 \; T_e^{3/2}/(n_e Z_I \ln\Lambda) \qquad \text{(sec)} \qquad (40a)$$

if the ion sound speed

$$C_I = c\sqrt{\frac{T_I + Z_I T_e}{m_I c^2}} \qquad (40b)$$

is greater than the absolute value of the drift speed U_Z, given by Eq. (10), and $T_e < T_I$. However, if the opposite conditions prevail at a local radial cell the τ_{eI} is calculated from

$$\tau_{eI}^{an} = \left\{\frac{1}{\tau_{eI}^{c\ell}} + \min\left[10^{-2}\,\omega_{p,I}\left(\frac{T_e}{T_I}\right)\left(\frac{|U_Z|}{C_I}\right)\;;\;\omega_{p,I}\right]\right\}^{-1} \qquad (40c)$$

where $\omega_{p,I}$, the ion plasma frequency, is

$$\omega_{p,I} = \left\{\frac{4\pi\, n_I\, e^2}{m_I}\right\}^{1/2} . \qquad (40d)$$

Although this formulation is superior to the previous resisitivty multiplier scheme the inability of the code to yield very realistic ion temperatures independent of the electron values has prevented its use for more than a few test cases (Section IV).

Section IV

BENCHMARK CALCULATIONS

Included in this section are ideal gas cylindrical diaphragm implosion as well as magnetic field diffusion benchmark results. In addition, some comparative implosion results, with and without radiative coupling or rezoning, are illustrated. It was decided to perform these calculations using interesting subsets of the complete model so as to strengthen the level of confidence in the full code. The first illustrated benchmark is the hydrodynamic-only subset where the voltage discharge and induced magnetic field contributions are removed. The driver of the fluid dynamics is t=0 radial distributions of density and pressure. Implosion is generated by the so-called cylindrical diaphragm problem with an assumed step density and pressure rise of a factor of four outside of a half-maximum radial point.

Criteria to observe within the implosion are whether temperature, pressure, and density jumps across the inwardly propagating shock and contact discontinuities are correctly transported by the FCT algorithm; these jumps can be calculated from steady planar one-dimensional theory coordinate propagating with respect to the discontinuity) before the advancing shock gets reasonably close to the cylindrical centerline. Beyond that comparison has to be made with established numerical solutions in the literature, such as Lapidus.(12) The solved equation subset comprises Eq. (1), Eq. (2) without the jB/c term, Eq. (3) without the $j\varepsilon$ and P_{RAD} terms, the single specie internal energy balance

$$E = \frac{1}{2}\rho v^2 + \frac{p}{\gamma - 1} \tag{41}$$

and $p = \rho RT$, for the five unknown ρ, v, E, p and T. Illustrated in Figures 2 through 5 are normalized radial pressure and density distributions evaluated at four different normalized times. Normalization, for density and pressure, (ρ^*, p^*) is to the respective $t=0$, $r=0$ magnitudes, while for time (t^*) it is to the unit diaphragm radius divided by the sound speed at $t=r=0$. Included in Figures 3 and 5 are the artifical viscosity, $\gamma = 1.4$ Lax-Wendroff finite difference solutions obtained, with a Cartesian x-y mesh, by Lapidus.(12) Correlation is reasonably good within the inner range of the implosion; as the FCT code employs an outer boundary condition of $\partial/\partial r\{\rho v\} = 0$ while the Ref. 12 solution considers $\rho v = 0$ here, considerable discrepancy in the outer region is understandable. The zero gradient boundary condition is more correct for z-pinch implosions.

What is of most interest is the shape and inward progression of the pressure and density shock and contact discontinuity fronts; the FCT calculated results are slightly more spread out than the Ref. 12 solutions. The difference is largely due to the factor of five decrease in Δr increment size; the relatively coarse mesh is still adequate to illustrate the disturbance propagation. The FCT implosion is also slightly slower in running into the centerline than the Lapidus model results; the outer zero gradient boundary condition on ρv, leading to some mass blowoff, would retard the inward progression. It seems as though the Ref. 12 pressure and density results do not line up as well as they could and that the Lapidus density calculations are running a bit ahead of the corresponding pressure profiles. The FCT density profiles may therefore be more accurate even with the reduced number of computation points.

For planar flow initiated by the bursting of a diaphragm, where subscript 1 denotes the region ahead of the propagation shock, subscript 2 the region immediately behind the shock, subscript 3 the region behind a contact discontinuity and subscript 4 the ambient region behind an isentropic expansion fan, the p_4/p_1 ratio is given by(13)

$$\frac{p_4}{p_1} = \frac{p_2}{p_1}\left\{1 - \frac{(\gamma-1)(p_2/p_1-1)}{\sqrt{2\gamma}\sqrt{2\gamma + (\gamma+1)(p_2/p_1-1)}}\right\}^{-\frac{2\gamma}{\gamma-1}} . \qquad (42)$$

p_4/p_1, the initial pressure ratio across the diaphragm, is given a value of 4.0; assuming $\gamma = 1.4$ yields, upon an iterative solution of Eq. (42), $p_2/p_1 = 1.93$. Successive employment is then made of

$$\frac{T_2}{T_1} = \frac{1 + \frac{\gamma-1}{\gamma+1}\frac{p_2}{p_1}}{1 + \frac{\gamma-1}{\gamma+1}\frac{p_1}{p_2}} , \qquad (42a)$$

obtained from the Rankine-Hugoniot relations, the perfect gas expression

$$\rho_2/\rho_1 = p_2T_1/p_1T_2 , \qquad (42b)$$

as well as

$$T_3/T_1 = \left(\frac{p_2/p_1}{p_4/p_1}\right)^{\frac{\gamma-1}{\gamma}} , \qquad (42c)$$

which is obtained from the facts that pressure is uniform across the contact surface ($p_2 = p_3$), there is an isentropic change between regions 3 and 4, and $T_4 = T_1$ from the initial conditions. Finally, for the perfect gas

$$\rho_3/\rho_1 = (p_2/p_1)(T_1/T_3) \ . \qquad (42d)$$

Included in the bottom row of Table 1 are the numerical magnitudes obtained from Eqs. (42) through (42d). The other rows of Table 1 collect results at four t* normalized times, given by the numerical solution to the conservation equations. Any discrepancies with the above results are due to cylindrical coordinate geometric focusing and the likelihood that a mesh with only 39 points is slightly coarse. The numerical results are, as would be expected, higher than the planar solution but are close enough to indicate a suitable numerical hydro-only algorithm.

Table 1

t*	(p_2/p_1)	(T_2/T_1)	(ρ_2/ρ_1)	(T_3/T_1)	(ρ_3/ρ_1)
0.197	2.20	1.33	1.65	0.849	2.57
0.326	2.29	1.32	1.74	0.873	2.46
0.393	2.13	1.37	1.56	0.848	2.62
0.493	2.25	1.32	1.69	0.864	2.72
Planar Flow	1.93	1.217	1.586	0.812	2.38

The next subset of the program to benchmark is the diffusion of azimuthal B-field, described by Eq. (13). Hydrodynamic plus B-field solutions will first explore the diffusionless limit of $r = \xi = 0$, i.e., both infinite conductivity and $\omega_e \tau_{eI}$. The resulting magnetic flux equation,

$$\frac{\partial B}{\partial t} = - \frac{\partial}{\partial r} (vB) \tag{43}$$

is of similar form to the planar mass conservation expression

$$\frac{\partial \rho}{\partial t} = - \frac{\partial}{\partial r} (\rho v) \ . \tag{44}$$

Numerical solution comparisons will only be made with analytical estimates across a plane-propagating wavefront. The shock relation corresponding to Eq. (43) is

$$B_1 v_1 = B_2 v_2 \tag{45}$$

while mass conservation through the shock surface is given by

$$\rho_1 v_1 = \rho_2 v_2 \tag{46}$$

Combination of the above two relations gives

$$B_2 = B_1 (\rho_2 / \rho_1) \tag{47}$$

Likewise, letting $B = a\rho$, where a is to be determined, we find that Eq. (43) becomes, with employment of Eq. (44),

$$\frac{\partial a}{\partial t} + v \frac{\partial a}{\partial r} = \frac{Da}{Dt} = 0 \ . \tag{48}$$

Therefore, $a = B/\rho$ should be constant in the diffusionless limit with respect to a coordinate system fixed at the shock. The wave propagation solutions will be the same as the previous cylindrical diaphragm model except that, at $t=0$, a radially uniform 10^3 Gauss magnetic field is imposed (both within and outside the diaphragm location). It is first of interest to see whether ρ and the B field tangential to the wave surface are numerically propagated in a similar manner, in particular behind the initial shock front. Due to the rapidity of B field propagation induced by the electrical resistivity and temperature gradient contributions Eq. (13) is solved implicitly while the cylindrical version of Eq. (44) is solved by explicit FCT. The diffusionless limit, Eq. (43), is also solved implicitly so some discrepancy may enter here.

Plotted in Fig. 6 is $a \equiv B/\rho$ which, from Eq. (48), should be constant in the diffusionless limit with respect to a coordinate system fixed at the shock. As is seen the variability of a over much of the time scale is not too large so that implicit B-propagation is adequate. The similarity breaks down at longer times, as the front nears the axis; numerically the cylindrical form of mass conservation is employed rather than Eq. (44). From Eq. (47) $B_2/\rho_2 = 3.15 \times 10^{7}$ Gauss cm^3/gm for all times so that the cylindrical numerical solution averages about 8% beneath this value up to 2.5×10^{-6} sec.

A significantly different temporal post-shock B-field distribution occurs when classical magnitudes of resistivity and thermal flux influence are incorporated. As shown in Table 2, the B magnitude rapidly drops, with some degree of oscillation, due to the small time scale of the diffusion process.

Table 2

$t(10^{-6}$ sec)	B_2/ρ_2 $\left(\frac{\text{Gauss cm}^3}{\text{gm}}\right)$	$t(10^{-6}$ sec)	B_2/ρ_2 $\left(\frac{\text{Gauss cm}^3}{\text{gm}}\right)$
0.587	1.346×10^6	1.950	-1.195×10^3
0.798	-2.449×10^4	2.140	-4.478×10^2
0.998	-1.523×10^3	2.320	-2.304×10^2
1.200	9.130×10^3	2.500	-1.299×10^2
1.390	-5.961×10^4	2.680	-60.4
1.580	2.479×10^4	2.860	-25.3
1.770	-2.310×10^3	3.050	-9.26

The magnetic diffusivity $c^2\eta/4\pi$ is of order 10^6(sec cm^2/sec^2), so that appreciable B-field changes occur in $\Delta t \sim 10^{-6}$ $(\Delta r)^2$ sec time scales. This rapid field change is appropriately represented in the numerical solution.

Plotted in Fig. 7 are the radial pressure distributions at three of the Figs. 2 and 4 times, both with and without the initially imposed 10^3 Gauss B-field. The field included solutions are for $r = 0$. The differences between the near equal time pressure profiles are relatively small except ahead of the pulse leading edge: here there is a precursor pressure perturbation that grows slightly with time.

The next set of benchmark computations involves the combination of the full B-field equation, Eq. (13), and the mass, momentum, internal energy and electron temperature equations, Eqs. (1), (2), (3) and (4). A constant $\gamma = 1.67$ adiabatic exponent is assumed with no radiation transport; however, there is an induced $\underset{\sim}{E}$ field resulting from a discharge-generated hydrodynamic collapse. n_e and T_I are calculated from Eqs. (11c) and (34), respectively. The idealized voltage—time shape illustrated in Fig. 8 is employed, similar to the one used in the Ref. 11 simulations, and the the three resistivity models—classical, corona multiplier {Eqs. (39) and (39a) with A = 49 and $B = 10^{-4}$}, and the Sagdeev instability form {Eqs. (40), (40c)} are utilized.

The initial conditions are radially uniform electron and ion temperatures of 1 eV, and an initial annular Gaussian distribution of ion number density

$$n_I = n_{I,max} \exp\left\{- (r-r_o)^2/R^2\right\} \qquad (49)$$

where the assumed conditions are $n_{I,max} = 10^{18}$ cm^{-3} and 5×10^{18} cm^{-3}, $r_o = 0.85$ cm and R = 0.25 cm. The discharge length is 5.0 cm and the plasma is assumed to be Ar with γ remaining at 1.67. The resistance and inductance of the external circuit are assumed to be 0.8 ohm and 1.5×10^{-8} henries, respectively, values characteristic of the Pithon machine at Physics International.

Figure 9 illustrates the maximum radially-dependent plasma density out to a maximum time of 200 nsec for the three resistivity models and two maximum n_I values. With $n_{I,max} = 5 \times 10^{18}$ cm^{-3} the initial mass per unit length is 6.98×10^{-4} gm/cm while with $n_{I,max} = 10^{18}$ cm^{-3} the mass per unit length is 1.39×10^{-4} gm/cm, which is comparable to the Ref. 11 value and of an appropriate magnitude for a maximum "tailored" implosion for these machine parameters. The smaller mass yields an implosion within the time span of the voltage pulse while a tendency towards collapse for the larger mass only occurs after pulse cessation. The ion temperature, calculated from Eq. (5), is, for the most part near or somewhat larger than T_e, so that the Sagdeev model yields η values usually of the classical magnitude; however, the density peak is close to the 50 times classical corona multiplier model. This anomalous resistivity multiplier model yields an implosion as dynamic as the classical η solution; indeed, for the smaller mass case the η^{an} implosion is 17 nsec more rapid although the peak density is somewhat reduced. This result is, however, in contrast to the softer implosions produced with resistivity multiplier solutions when radiation transport is included (Ref. 11 and Section V).

Illustrated in Fig. 10 are the radial distributions of T_e for the lower mass distribution at the times of maximum compression (depending on η). The temperature peaks in this radiationless calculation are immediately outside the region of rapid density fall-off, as seen by comparison of Figs. 10 and 11. Maximum attained densities are not as high or the width of the collapsed zone not as narrow as would be found in a coupled radiation emission solution, however. In contrast, the higher mass level (Fig. 12) weakly implodes the discharge resulting in a relatively ineffective collapse. It is of interest to note that the lack of significant collapse enables the 202 nsec time span to be covered with 500 minimum Courant condition time steps while a maximum of 160 nsec is spanned with 950 Courant condition steps when a collapse is achieved. It is noted that the inclusion of radiation and the generally more restrictive internal energy change timestep, Eq. (25d), results in roughly a tripling of the timestep number (Section V).

Referring again to Fig. 9 we see that the implosion time for the five times heavier mass is about 40% greater than the implosion time for the lighter mass (measured from the beginning of collapse). It is of interest to see whether a simple dynamic pinch model, suggested by A. Mondelli, yields anything like this value. If we assume that the discharge acts through a cylindrical plasma annulus of thickness δ, length L, and radius r, such that $\rho = (M/L)/(2\pi r\delta)$, $J = I/2\pi r\delta$ and $B = 2I/cr$, then

$$\rho \frac{d^2 \underset{\sim}{r}}{dt^2} = \frac{\underset{\sim}{J} \times \underset{\sim}{B}}{c} \qquad (50)$$

yields, upon collapse from $r = r_0$ to $r = 0$ over a timespan t,

$$t = r_0 \sqrt{\frac{M}{L}}\, \frac{c\sqrt{\pi}}{2I} \; . \qquad (51)$$

The implosion time ratio is then proportional to the square root of the mass ratio, within this simple model. As the actual correlation is closer to the 0.25 power of the mass ratio, simple modeling of these implosions is of more qualitative rather than quantitative value.

Test calculations evaluating the suitability of dynamic rezoning are performed using the Physics International Pithon Shot #1400 Argon gas puff. The TERRYS two-path radiation package is employed, contrary to the employment of the ATPHYS routine on the same data last year. The argon fits to the optically thin radiation parameters are as follows, from R. Terry (private communication). In Eq. (50)

$N = 0.60$, $M = 14$ for L-shell line radiation,

$N = 2.50$, $M = 12$ for K-shell line radiation,

$N = 0.80$, $M = 14$ for bound-free radiation,

$n_I^o = 10^{19}\ \text{cm}^{-3}$.

$$P^{OT}_{L\text{-shell}} \sim (n_I/10^{18})^{1.4722} \quad \text{for } n_I > 10^{18}\ \text{cm}^{-3}$$

$$P^{OT}_{L\text{-shell}} \sim (n_I/10^{18})^{2.0} \quad \text{for } n_I < 10^{18}\ \text{cm}^{-3}$$

$$P^{OT}_{K\text{-shell,BF}} \sim (n_I/10^{18})^{2.0} \quad \text{for all } n_I.$$

Unfortunately, the complex spectra L-shell radiation for argon is, at present, incompletely modeled. Therefore, the Ar calculations should be considered as useful comparisons between Eulerian uniform mesh and dynamic rezoned mesh information, not as absolute results. It is assumed that all the transport coefficients, especially resistivity, are of microscopic classical magnitude.

The temporal voltage distribution, of a maximum magnitude of 3.89×10^6 V and pulse time of 300 nsec, is (Table 3)

Table 3

t/t_{pulse}	V_g (volts)	t/t_{pulse}	V_g (volts)
0.0000	100.0	0.4600	2.90×10^6
0.0500	1.0×10^5	0.4833	2.60×10^6
0.0733	5.0×10^5	0.5267	2.45×10^6
0.1000	1.50×10^6	0.5900	1.70×10^6
0.1500	2.50×10^6	0.6567	5.00×10^5
0.2067	3.50×10^6	0.7133	-2.30×10^5
0.2667	3.75×10^6	0.7400	-2.50×10^5
0.3333	3.89×10^6	0.7667	1.00×10^2
0.3533	3.83×10^6	0.8333	3.00×10^5
0.4067	3.50×10^6	1.0000	6.00×10^5

The t=0, 5 cm long initial gas puff ion number density, over the 39 cells of the computation, is illustrated in Fig. 13. The dashed line near the outer edge is an extrapolation past the last measured data point. Input is by simple specification of $\rho \approx n_I m_I$ at the 39 cell midpoints. The radially uniform temperature at t=0, for both electrons and ions, is 1.0 eV.

The first presented calculations assume the spatially uniform cell case. Plotted, at the two times of 81.7 and 101.2 nsec, are n_I, n_e, T_e and normalized P_{RAD} (total) as a function of radius. Also plotted, as a function of time, is the total normalized radiated energy per unit discharge length out to t = 125.7 nsec. Figure 14 illustrates the number density distributions at both times. The peak of the number density distributions has not moved appreciably inward at 81.67 nsec but the magnitudes at and within the peak radii have increased somewhat at the expense of the outer zones. The first complete implosion, defined at the point beyond which the net velocity begins to reverse itself near the discharge centerline, occurs at near 101.2 nsec. It is seen that steep centerline density peaks, extending only a few cells in width, have formed at this point. Actually these sudden centerline peaks have formed only over the previous 3-4 nsec of implosion time. The density steps are largely due to the retention of perturbations which is a feature of the FCT algorithm, as well as a slightly insufficient cell number. The relatively flat floors of density are essentially imposed at a magnitude that is 5×10^{-3} of the average value over the total discharge width. A comparatively high centerline density (within an order of magnitude of the illustrated values) is maintained for at least 25 nsec beyond the 101.2 nsec point; however, the radial velocity distribution becomes quite discontinuous with probable formation of hydrodynamic instabilities.

Figure 15 shows the electron temperature distributions at the same times. It is seen that the outer zones of the implosion heat up to more than 10 keV coronal temperatures; densities are, for the most part, correspondingly low at these positions. Near the maximum compression the high density centerline material heats up to over 1 keV temperatures, yielding the maximum radiative output.

Figure 16 illustrates the radial normalized total radiative power distributions at the same times. The radiative peak, at 81.67 nsec, is at near the maximum n_I location, with a T_e value of about 400 eV. The maximum radiative location is the centerline at the 101.2 nsec initial compression time. Figure 17 shows the total normalized radiant energy per unit length for both the uniform cell width case and a rezoning results, discussed later. It is seen that E_{RAD} increases at a relatively slow rate after the first collapse, although running out several hundred more steps (it took 629 steps to reach 81.67 nsec, 1119 steps to get to 101.2 nsec, and 2000 steps to reach 125.7 nsec) beyond the 125.7 nsec stop may attain a measurable E_{RAD} increase. However, as indicated before, discontinuities in the radial velocity profile point to an unstable compressed region, with a 1-D modeling being questionable.

Illustrated in Figs. 17 through 21 are the results of a rezoned calculation with $M^{o} = 0.025$, $b = 0.05$, $c = 0.05$ {in Eq. (29)}. The solution remains stable with a maximum divergence from energy balance of 2% (after 900 time steps the error is significantly smaller). Going first to Fig. 18 we see the cell width distributions at $t = 82.01$ and 100.7 nsec. These times are comparable to those chosen in the uniform increment solution, but it is interesting to note the different number of time steps required to reach these times (1124 and 1649 versus 629 and 1119 for the uniform cells). Comparison of the Δr distributions in Fig. 18 with the associated n_I distributions in Fig. 19 show that appropriate tracking (smallest cells with largest density and vice versa) is produced. The average cell width is calculated from Eq. (27a). At the same implosion times the computed outer radius of the discharge is about 10% smaller in the rezoned solution compared with the uniform cell model.

Comparison of the Figs. 14 and Fig. 19 number density shape distributions show general similarity but sufficient differences to indicate some cell width effects. In particular, the rezoned maximum centerline n_I at the collapse point is about 50% higher than the uniform cell result. Curiously enough, as the rezoned centerline temperature is somewhat lower the radiated power at this point is about the same, irrespective of the model (Figs. 16 and 21). The narrowness of the maximum density distribution near the center is not really reduced with rezoning, although it should be noted that the extreme density "spike" is largely formed in the last 2 nsec before the collpase; prior to this the density and radiation distributions are somewhat less peaked near the center.

Returning to Fig. 17 we see that the radiated energy output obtained with the rezoned mesh is comparable with the previous result; however, at times beyond the collapse the rezoned magnitudes can be up to 20% below that obtained with the uniform mesh. In summary, comparison of Figs. 14 and 19 for number density, Figs. 15 and 20 for electron temperature, 16 and 21 for radiative power and the separate energy distributions on Fig. 17 illustrates the influence of a moderate rezoning algorithm.

In conclusion, the varous subsets of the code—cylindrical implosion dynamics, magnetic flux generation, dynamic cell rezoning, nonequilibrium radiation coupling, and resistivity transport modeling have been checked out separately and in some combination; it is felt that full modeling with realistic input data can give suitable theoretical-experimental correlation.

Section V

SAMPLE CALCULATIONS

The coupled hydrodynamic-radiation calculations are illustrated for two separate situations. The first is a comparison with the SPLAT code implosion results due to R. Terry(4), following the original analysis of Tidman(14); in this code the plasma produced in the discharge through an Aℓ wire cage is modeled by a radially isothermal analysis with radially integrated representations of mass, momentum, and energy across an assumed core and corona zoning. This is a so-called zero-dimension transient analysis in contrast to the one-dimensional solutions illustrated here. The second comparison set is a numerical representation of a Maxwell Laboratory Blackjack V experimental configuration; a variation of plasma mass, for both Aℓ and Ar, is employed so as to compare the space and time integrated radiation yields. In addition, radial distributions of temperature, radiative power, and density are illustrated for near the optimum mass at the pinch collapse time.

Figure 22 shows the voltage-time profile employed in the SPLAT calculations. The maximum voltage is 4.5×10^6 V, attained in 150 nsec. The quantities would be experimentally maximum, and indicate an optimistically energetic profile. External circuit parameters are a 0.5 Ω generator impedance Z_g and a 13.5 x 10^{-9} h diode inductance. Although a variety of original wire cage radii were investigated in Ref. 4, ranging from R^0 = 0.7 to 1.6 cm, only R^0 = 1.0 cm will be explored here. It is assumed in all the wire calculations that there is an azimuthal symmetry in the plasma prior to an appreciable implosive collapse. The calculations assume three different masses, made up of 6, 12, and 24 wires of 1 mil diameter and 3 cm length. The mass/wire of Aℓ wire is 4.10 x 10^{-5} gm so that the three separate masses analyzed are 2.46 x 10^{-4}, 4.92 x 10^{-4}, and 9.85 x 10^{-4} gm, respectively. It is assumed that a 39 cell numerical analysis is adequate and that most of the initial plasma density is included into the two cells nearest r = 1 cm, the total computation radial extent being near 2 cm at t = 0. The initial six wire plasma density distribution is then 1.0 x 10^{-7} gm/cm^3 for $.0256 \le r_c \le 0.8977$ cm, 1.28 x 10^{-4} gm/cm^3 for $.949 \le r_c \le 1.000$ cm, and 1.0 x 10^{-7} gm/cm^3 for $1.0516 \le r_c \le 1.975$ cm, r_c denoting the cell center location. Twelve and 24 wire cages are corresponding multiples of the $.949 \le r_c \le 1.000$ cm density value. A small amount of mass is therefore assumed to have diffused over the entire $0 \le r \le 2.0$ cm computational extent at the initialization of calculations.

It is assumed that uniform cell width, no density-dependent rezoning, is adequate for these computations. The initial radially uniform temperature is 10 eV. Illustrated in Fig. 25 is the temporal distribution of normalized energy for the three wire numbers; computations were stopped when excessive velocity discontinuities occur and energy balance begins to break down. The same energy magnitude normalization is used for this case as is employed in the subsequent Blackjack V representations.

Table 4 shows the time to collapse (pulse time) for the three masses as calculated by the R. Terry SPLAT code and the WHYRAD results; the WHYRAD computed time is the location of the first peak of cross-sectionally integrated radiative power, simultaneous to the maximum yield located near the centerline. Also included in Table 4 are the ratios of total radiated energy at these times divided by the six wire value for the WHYRAD calculations, as well as the ratios of the K-shell line radiation magnitudes for both SPLAT and WHYRAD computations.

Table 4

Wire No.	SPLAT Pulse Time (nsec)	Δt	WHYRAD Pulse Time (nsec)	Δt	WHYRAD E_{RAD}/E^6_{RAD}	K-Shell WHYRAD E_{RAD}/E^6_{RAD}	K-Shell SPLAT E_{RAD}/E^6_{RAD}
6	98.9		111.6		1.0	1.0	1.0
		15.8		10.2			
12	114.7		121.8		1.688	1.415	2.02
		8.4		19.0			
24	123.1		140.8		4.196	1.910	2.67

Direct comparison between the WHYRAD and SPLAT results could be better; in particular, the incremental time change between successively massive collapses is nearer to a linear function of wire number with WHYRAD while its a sharply decreasing function of wire number with SPLAT. The K-shell line WHYRAD yield ratios are somewhat lower than the comparable SPLAT results, although the total radiation yield as obtained from WHYRAD steeply increases for 24 wires due to continuum and L-shell line contributions. Nevertheless, there is a steady yield increase with both codes as the wire number increases, and the wire cage is not yet too massive so as to be weakly collapsible.

Figure 24 shows radial electron and ion number density distributions at the 12 wire collapse point, t = 125.8 nsec. This is a few nsec beyond the time selected for the illustration of comparative yield. Figure 25 illustrates the radial distributions of normalized total radiative power and electron temperature at the same time. The temperature near the centerline is relatively high at this time; the local yield of radiant energy subsequently cools these cells to under 100 eV with eventual reheating due to thermal conduction.

The Blackjack V representations illustrated here have been presented at the 1981 APS Plasma Physics meeting.(15) So as to show the comparative flexibility of the WHYRAD program it was decided to run both Aℓ and Ar implosion examples, using the same voltage-time profile over a range of discharge medium masses. The Maxwell Blackjack V machine conditions, as applied to an Ar gas puff, were presented in a memo by Richardson, et al.(16); while more general machine information (external circuit inductance, impedance) is contained in an R&D Associates report by Fisher and Sze.(17)

The initial radial temperature distribution is assumed to be a uniform 1 eV, while the timewise diode voltage distribution is given in Table 5:

Table 5

t (nsec)	V_g (10^6 V)	t(nsec)	V_g (10^6 V)
0.0	0.0	85.0	1.50
42.0	1.5	95.0	1.30
50.0	2.0	112.0	0.60
60.0	2.75	122.0	0.40
64.0	2.80	125.0	0.00
68.0	2.75	140.0	-0.75
75.0	2.37	150.0	-1.00
77.0	2.00	175.0	-0.50
80.0	1.90	200.0	-0.10

Linear interpolation between these points accurately models the Blackjack V voltage pulse of the Richardson, et al., experiments. Figure 26 illustrates both the voltage and

current distributions. The machine impedance and inductance are 0.58 Ω and 2 x 10^{-9} henries, respectively, while the diode inductance varies from 15 x 10^{-9} to 27 x 10^{-9} henries, depending on diode geometry. Wayne Clark (private communication) at Maxwell has indicated that the appropriate diode inductance is 21 x 10^{-9} henries, so that with the open circuit prior to crowbarring being in series,
L_g = 23 x 10^{-9} henries.

The Ref. 16 initial Ar gas puff pressure (or density) distributions are very qualitative, so it was decided to assume a general Gaussian relation for the t = 0 density distribution:

$$\rho = \rho^{MAX} \exp\left\{-B(r-1.0)^2\right\} \tag{52}$$

where 1.0 cm is the annular radius of the gas puff maximum density in the Richardson, et al. experiments. The density is not really symmetric about this point as more material is initally present throughout the outer zones; however, this distribution is suitable for comparative calculation with an Aℓ wire cage located at the same radius. This, of course, also assumes that the wire plasma, upon formation, collects in an azimuthal direction prior to any appreciable radial collapse. It is assumed that, for the same mass, the Aℓ plasma distribution is somewhat narrower around the Gaussian peak at t = 0 than the Ar gas puff so that $B_{A\ell} = 5$, $B_{Ar} = 3$. Four separate masses are employed for Aℓ and a subset of two separate masses for Ar; the four masses are

$$M = 50,\ 10,\ 150 \text{ and } 300\ \mu\text{gm},$$

the lowest mass being a bit small for wires (≃ 2 Aℓ wires), while the highest mass is representative of a 12 wire cage or a rather dense Ar puff. With the specification of the total mass then ρ^{MAX}, in Eq. (51), is determined by numerical integration of

$$\rho^{MAX} = (M/L)\left\{2\pi \int_{0}^{R^{O}} e^{-B(r-1.0)^2}\, r dr\right\}^{-1}, \qquad (52)$$

where R^{O} is assumed to be 2.0 cm. L = 3.0 cm is the diode spacing.

The flow is divided into 45 cells out to a total initial radius of 2 cm, six more than previously, so as to hopefully yield a bit more accuracy near the maximum collapse. In this regard the M^{O} power in the density-cell width rezoning algorithm is assumed to have the value 0.025 so as to obtain a 30-40% maximum cell width differential (probably as much as can be obtained with the present code). Classical transport, including the resistivity, will be assumed in the initial group of calculations.

Figure 27 shows aluminum ion and electron number density radial distributions at t = 0 and two subsequent times for M/L = 5 x 10^{-5} gm/cm (M = 150 μgm). This mass magnitude, as will be shown later, is about the optimum implosion value. The 105.7 nsec time is prior to the rapid pinch collapse, with resulting energetic radiation yield, while 118.5 nsec is after the collapse. The dynamic sweeping in of n_I between these two times is evident. The collapsed high density region diameter of about 1 mm is realistic as is the 10^{20} cm^{-3} ion density and 10^{21} cm^{-3} electron density. Illustrated in Figure 28 are the temperature and normalized radiative power radial distributions at the same mass level and implosion times; the arrows point to the ordinate associated with the particular curve. The centerline temperatures heat up to near 1 keV (from the initial 1 eV uniform temperature) while low density corona temperatures are > 10 keV. The radiative power yield after collapse is strongly peaked near the axis, however, as the density is so low in the corona.

Figures 29 and 30 show the time dependencies of the cross-sectional integrated normalized radiative powers for the four masses of interest (M/L = 1.667, 3.333, 5.0 and 10 x 10^{-5} gm/cm). These distributions show a multiple peaking behavior; upon compression there is a heating up of the inner cells resulting in large radiation outputs with subsequent cooling. The radiative output in this high density region then falls; however, thermal diffusion processes subsequently induce a reheating with an eventual repetition of the radiative peaking. It is possible that incorporation of viscous momentum transport and energy dissipation would have some damping effect on the radiative peaking. It is seen that the initial collapse, illustrated by the first power peak, progresses back from 90 nsec to 140 nsec as the mass is increased. If it is assumed that an optimum tailored implosion is at the maximum current point then, from Figure 26, the initial power peak should be about 110-120 nsec. The M/L = 5.0 x 10^{-5} gm/cm case would seem to be the most optimum although, as is illustrated in Figure 31, the normalized radiant energy is slightly maximized with the 3.33 x 10^{-5} gm/cm mass case. As indicated in the previous computations the radial velocity distribution becomes highly discontinuous in the past-initial collapse phase and the accuracy of the hydrodynamic solution rapidly decreases. They dynamics of the 10^{-4} gm/cm collapse is rather weak; probably doubling this value would prevent any collapse at all.

The maximum computed energy yields, as given in the classified DNA final report, are somewhat smaller than recent experimental results (private communication from

J. Pearlman and W. Clark); however, the experimentally optimum tailored mass seems to be about 150 μgm or a little greater. A theoretical yield increase could be obtained by further heating of the center two or three cells upon collapse; relatively modest temperature increases would significantly raise the radiation level. It is possible that incorporation of viscous dissipation in the energy equations would also help in this regard, and it is also possible that evaluation of axially dependent hot spots by two dimensional modeling would yield substantially higher radiant energy magnitudes. These avenues of investigation should be pursued in future work.

Figures 32, 33 and 34 illustrate area integrated radiative powers and radiative energies (both normalized) for Aℓ and Ar, considering the lower two masses. As was mentioned in Section IV the L-shell Ar radiation is, at present, incomplete; therefore, comparison between the two elements is illustrated by removing the L-shell contribution from Aℓ. It is interesting to note that the temporal dependencies of the integrated radiative powers are similar for both elements; Aℓ has a higher peak at collapse, however, with neglect of the L-shell radiation. It is also interesting to note the collapse times for the two Aℓ masses, ~90 nsec and 103 nsec, are the same as the previously illustrated Aℓ collapse times, including the

L-shell radiative contribution. Therefore, any reasonably modest alteration of the radiative modeling and the resulting yields would fortunately not have too much of an effect on the relative mass tailoring illustrated here. The multiple peaking behavior, illustrated in the previous power-time distributions (Figs. 29 and 30), is also present, in particular, for Aℓ (Figs. 32 and 33). The actions of thermal diffusion and radiative transport are an explanation. Neglect of the Ar L-shell radiation seems to produce a less oscillatory radiative distribution with a more rapid post-initial compression drop.

Figure 35 compares, for an $M/L = 3.333 \times 10^{-5}$ gm/cm Aℓ implosion, the effects of anomalous resistivity in the normalized radiant energy. Although the anomalous resistivity multiplier model initially yields a higher radiant energy the end result is a somewhat softer implosion with a 50% reduction in total yield.

Figures 36 through 43 illustrate L and K-shell aluminum spectra, line plus continuum, as obtained from post-processing at the two separate time steps shown in Figures 27 and 28, for the $M/L = 5.0 \times 10^{-5}$ gm/cm mass value. The individual temperature and density distributions, over a sufficient number of inner cells, were inserted into the full MCELL multicell coupled radiation and population density routine by D. Duston. The R_s value is the radial extent of the computational cells inserted into MCELL; radial extension beyond this value is unnecessary due to the optical thinness and reduced emission of the low density corona.

The L-shell spectra, prior to the initial collapse, is shown in Figures 36 and 37 over the photon energy range from 0.03 to 0.42 keV. The same normalization intensity value, in $(W/cm^2/keV)_0$ is used in all the spectral distributions. Most of the energetic L-shell lines are $A\ell^{XI}$ Li-like; it is seen from Figure 37 that a normalized intensity of 0.5 is reached with the 2s-3p Li-like line at 0.256 keV photon energies. The 2p-3d line is only a little less energetic. Figure 38 illustrates the pre-collapse less complex K-shell spectra made up of $A\ell^{XIII}$ H-like and $A\ell^{XII}$ He-like lines as well as the continuum intensity distributions. The most intense Lyman-α line gets up to a normalized intensity value of 0.6 at 1.728 keV photon energy. Figure 39 is a integrated spectrum that ideally should be seen by X-ray diodes; for example, a diode opaque to all radiation below 1 keV would present a spectrum having the illustrated shape for E > 1 keV.

The post collapse spectra at t = 118.5 nsec is illustrated in Figures 40 through 43; a number of individual line intensities are markedly increased upon collapse. As an example, the H-like 2p-3d line now emits a normalized intensity of about 15.0 at $h\nu$ = 0.31986 keV. For K-shell radiation the L_α line puts out a normalized intensity of about 120.0, which is 200 times the L_α intensity prior to the collapse. A similar intensity increase of about two orders of magnitude would be presented by XRD's, as is seen when comparing Figures 39 and 43.

Summarization of the Blackjack V - simulated numerical representations should include the following statements:

Centerline ion number densities implode to the order of 10^{20} cm^{-3} with near 1 keV temperatures at the same location. The computed high density region is around 1 mm in diameter upon collapse.

Collapse times, as illustrated by temporal variations of the radially averaged radiative power as well as the radiative energy may be directly compared against the peak of the experimental total current distribution.

The 100 μgm and 150 μgm Aℓ mass implosions present optimum tailoring for the Blackjack V simulations. The 300 μgm case is too massive, and while eventually imploding at ≃ 140 nsec, the yield is somewhat reduced.

The energy yields exhibit a rapid rise of 3-5 nsec immediately prior to collapse, indicating a fast creation of the centerline density peak. Although not specifically illustrated, the computed centerline temperature values fluctuate in time, falling to temporarily low values (~50 eV) immediately after a high power yield peak, with subsequent reheating.

Continuation of the solution to times much beyond the initial collapse is of reduced practicality due to calculated sharp discontinuities of the radial velocity profile; beam instabilities would predominate.

Comparison of continuum plus K-shell Argon and aluminum implosions indicate fairly close temporal power and energy distributions with Al eventually attaining a larger magnitude with a more sudden energy jump upon collapse.

Incorporation of a multiplicative anomalous resistivity in the coronal region of the plasma yields a softer implosion with a reduced total energy output.

Line radiation intensities exhibit a rapid increase upon collapse with the hydrogen-like Lyman lines producing at least two orders of magnitude jumps within a 10 nsec or so time span. Post processing of the coupled hydrodynamic-approximate radiation solutions with a detailed MCELL computation furnishes an effective comparison diagnostic with fast time scale experimental pulse spectral measurements.

Section VI

CONCLUSION

This section has covered the basic modeling behind WHYRAD with its application to a wide range of cylindrically imploding benchmarks and two physically plausible test cases. The test cases were primarily treated to observe the effects of a range of wire or gas puff masses. The code realistically predicts imploded region diameters, collapse times, comparative solution magnitudes resulting from a variation of the total pinch mass, maximum centerline ion and electron densities, peak centerline temperatures, and the radial region of extent of radiation emission. The total radiation yield is low, requiring a higher average temperature near the centerline and/or the incorporation of axially-dependent hot spots. Nevertheless, the presented results show quantitative realism of many parameters, and a moderate amount of code alteration should improve radiation representation.

Section VII

REFERENCES

1. D. G. Colombant, M. Lampe, and H. W. Bloomberg, NRL Memorandum Report 3726 (1978).
2. S. I. Braginskii in *Reviews of Plasma Physics*, edited by M. A. Leontovich (Consultants Bureau, New York, 1965), p. 205.
3. J. P. Boris, NRL Memorandum Report 3237 (1976).
4. R. E. Terry and J. U. Guillory, JAYCOR Report No. TPD200-80-012, October 1980.
5. D. Duston and J. Davis, Physical Rev. A, Vol. 23, No. 5, p. 2602 (1981).
6. D. Duston and J. Davis, "Density Effects on the Spectral Emission of a High Temperature Argon Plasma," NRL Memo, to be published.
7. J. Apruzese, J. Davis, D. Duston and K. G. Whitney J. Quant. Spect. Radiat. Transfer, Vol. 23, p. 479 (1980).
8. J. Apruzese, J. Quant. Spect. Radiat. Transfer, Vol. 25, p. 419 (1981).
9. J. W. Shearer and W. S. Barnes, in *First Workshop on Laser Interaction and Related Plasma Phenomena*, Vol. 1, p. 307, ed. by H. Schwarz and H. Hora, Plenum Press (1971).

10. D. Book, NRL Memorandum Report 3332 (1977).

11. D. G. Colombant, M. Lampe, J. Davis, and H. W. Bloomberg, NRL Memorandum Report 3840 (1978).

12. A. Lapidus, J. Computational Phys. 8, p. 106, (1971).

13. H. W. Liepmann and A. Roshko, Elements of Gasdynamics, J. Wiley and Sons Pub. (1957).

14. D. A. Tidman, Final Report on Exploding Wires and Advanced Concepts Theory, JAYCOR Contract with Naval Research Laboratory, Contract No. N00173-79-C-0407, January 1979.

15. E. L. Kane and D. Duston, Numerical Comparison of Ar and Aℓ Z-Pinch Implosion Parameters, Bulletin of the American Physical Society, Vol. 26, No. 7, September 1981.

16. R. Richardson, W. Clark, M. Gersten, and M. Wilkinson, unpublished Maxwell Laboratory Argon Gas Jet Implosion Experiments, 1981.

17. G. P. Fisher and H. M. Sze, DNA Pulsed Power User's Manual, R&D Associates, RDA-TR-113301-001, January 1980.

AD-A113 597   SCIENCE APPLICATIONS INC MCLEAN VA   F/G 20/9
RADIATION FROM HIGH TEMPERATURE PLASMAS.(U)
FEB 82 E KANE, J APRUZESE   N00173-80-C-0493
UNCLASSIFIED SAI-82-686-WA   NL

2 OF 3
AD A
113597

Section VIII

FIGURE CAPTIONS

1. Schematic of the coupled discharge-diode circuit.
2. WHYRAD pressure solution for the cylindrical imploding diaphragm problem, $\gamma = 1.4$, 4 to 1 pressure ratio, 39 finite difference cells.
3. Lapidus (Ref. 12) pressure solution for the cylindrical imploding diaphragm problem, $\gamma = 1.4$, 4 to 1 pressure ratio, 199 finite difference cells.
4. WHYRAD density solution, same conditions as Fig. 2.
5. Lapidus density solution, same conditions as Fig. 3.
6. WHYRAD magnetic field-density ratio solution for the imploding cylindrical shock with an initially uniform 10^5 Gauss field parallel to the shock surface; other parameters same as Fig. 2. Infinite plasma conductivity.
7. WHYRAD pressure solution for the cylindrical imploding diaphragm problem, with and without tangential B-field. Infinite plasma conductivity and other parameters same as Fig. 2.
8. Simple benchmark timewise voltage distribution for radiationless, $\gamma = 1.67$ implosions.

9. Timewise distribution of radially maximum density for $\gamma = 1.67$ Ar with no radiation. $n_I^{max}(t=0) = 5 \times 10^{18}$ cm^{-3} and 10^{18} cm^{-3} with classical, 50 times multiplier and Sagdeev resistivities.

10. Radial distribution of T_e for $\gamma = 1.67$, $n_I^{max}(t=0) = 10^{18}$ cm^{-3} argon at t = 133 nsec (classical η) and t = 138 nsec (50 x multiplier η).

11. Radial distributions of n_I for the same conditions as Fig. 10.

12. Radial distributions of n_I for $\gamma = 1.67$, $n_I^{max}(t=0) = 5 \times 10^{18}$ cm^{-3} Argon at t = 180 nsec (50 x multiplier η) and t = 182 nsec (Sagdeev η).

13. Radial distribution of ion number density, at t = 0, measured from the Physics International Pithon Shot No. 1440.

14. Radial distributions of n_e and n_I at t = 81.67 and 101.2 nsec, assuming a uniform width, 39 cell mesh with Ar, T(t=0) = 1 eV, the n_I distribution of Fig. 13, and the voltage distribution of Table 3.

15. Radial distributions of T_e for the conditions of Fig. 14.

16. Radial distribution of radiant power for the conditions of Fig. 14.

17. Timewise distribution of radiant energy per unit length for the conditions of Fig. 14, assuming both uniform cellwidth and rezoned meshes.

18. $M^c = 0.025$ rezoned cell widths, at $t = 82.01$ and 100.7 nsec, for a 39 cell mesh with Ar, $T(t=0) = 1$ eV, the n_I distribution of Fig. 13 and the voltage distribution of Table 3.

19. Radial distribution of n_e and n_I at $t = 82.01$ and 100.7 nsec, assuming a $M^c = 0.025$ rezoned 39 cell mesh.

20. Radial distributions of T_e for the conditions of Fig. 18.

21. Radial distribution of normalized radiant power for the conditions of Fig. 18.

22. Voltage-time profile employed in the SPLAT and comparative WHYRAD calculations.

23. Timewise distribution of radiant energy for 6, 12, and 24 one mil Al wires of 3 cm length, employing the voltage profile of Fig. 22 with $T(t=0) = 10$ eV.

24. Radial n_e and n_I distributions at $t = 125.8$ nsec, $n_I(t=0)$ distribution for 12 wires.

25. Radial T_e and normalized radiant power distributions at $t = 125.8$ nsec, $T_e(t=0)$ distribution for 12 wires.

26. Timewise voltage and current distributions for a Maxwell Laboratory Blackjack V pulse.

27. Radial Aℓ ion and electron number densities at t = 105.7 and 118.5 nsec for M = 150 μgm, with the Fig. 26 Blackjack V voltage driver.

28. Radial Aℓ T_e and normalized radiant power distributions at the same conditions of Fig. 27.

29. Timewise cross sectionally-averaged normalized radiative power distributions for M = 50 and 100 μgm, with the Fig. 26 Blackjack V voltage driver.

30. Timewise cross sectionally-averaged normalized radiative power distributions for M = 150 and 300 μgm, with the Fig. 26 Blackjack V voltage driver.

31. Timewise distribution of the total normalized radiation energy for M = 50, 100, 150 and 300 μgm, using the Fig. 26 voltage driver.

32. Timewise cross sectionally-averaged normalized radiative power distributions for M = 50 μgm Aℓ and Ar, no-L shell line contributions, with the Fig. 26 voltage driver.

33. Timewise cross sectionally-average normalized radiative power distributions for M = 100 μgm Aℓ and Ar, no-L shell line contributions, with the Fig. 26 voltage driver.

34. Timewise distributions of the total normalized radiation energy for M = 100 μgm Aℓ and Ar, no-L shell line contributions, with the Fig. 26 voltage driver.

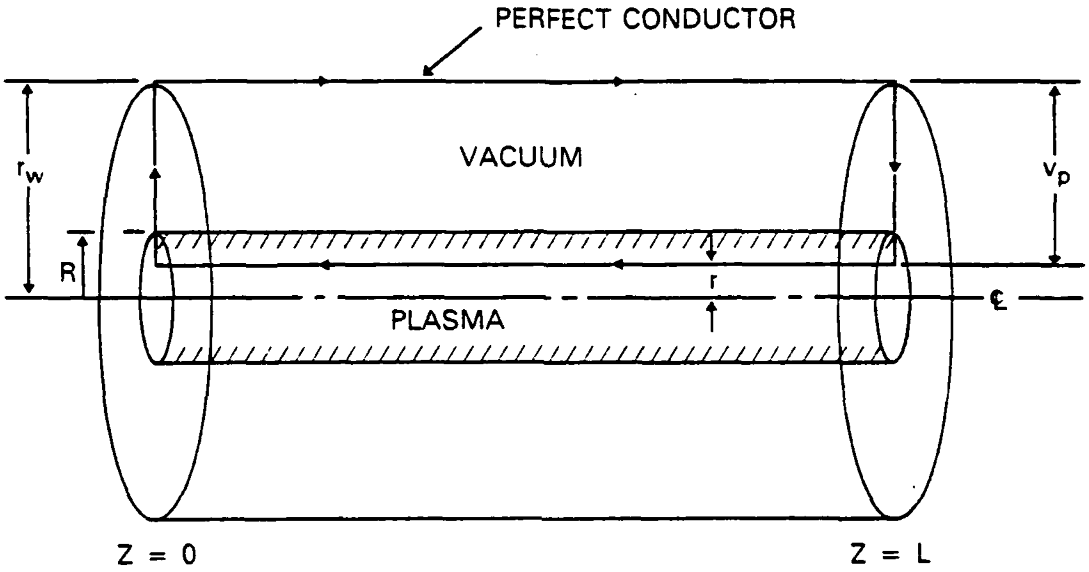

IMPLOSION CONFIGURATION

Figure 1

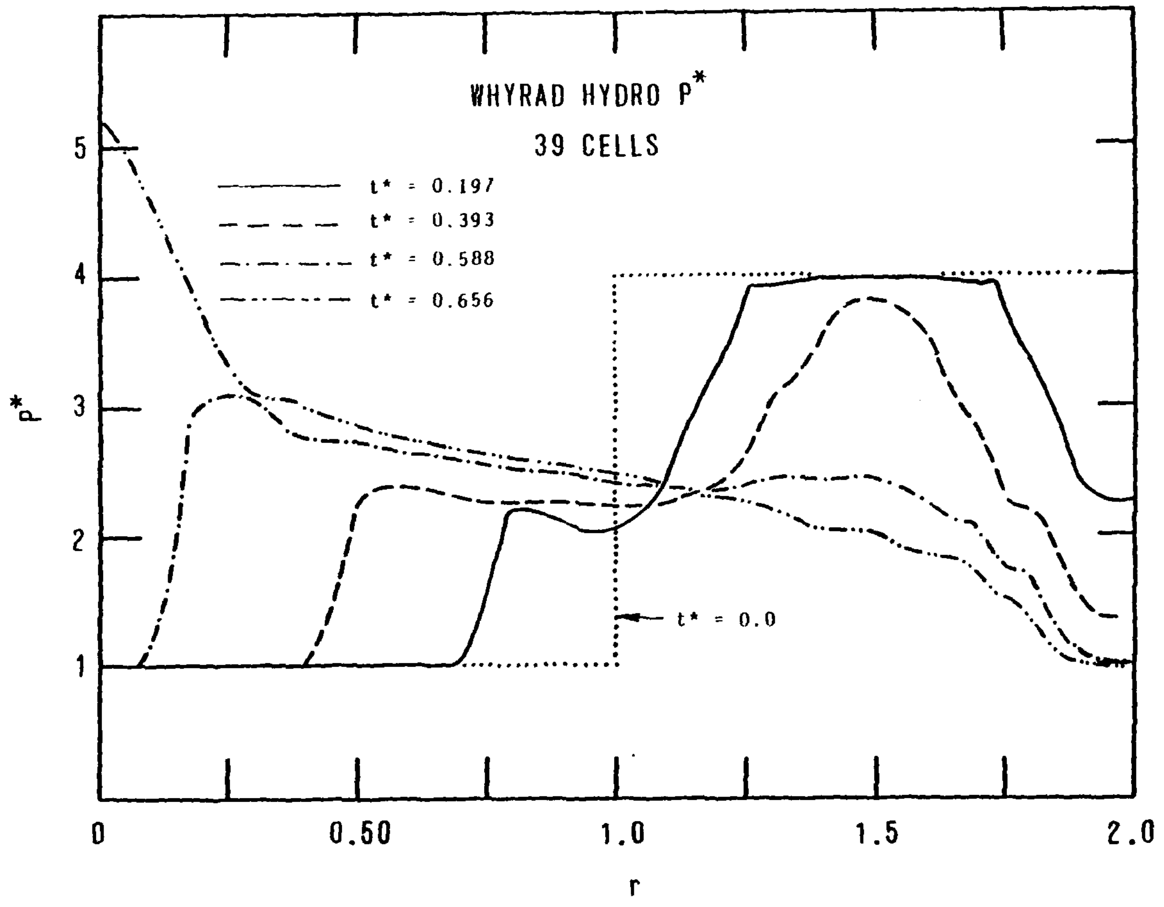
WHYRAD HYDRO P^*
39 CELLS
t* = 0.197
t* = 0.393
t* = 0.588
t* = 0.656
t* = 0.0
P^*
5
4
3
2
1
0
0.50
1.0
1.5
2.0
r

Figure 2

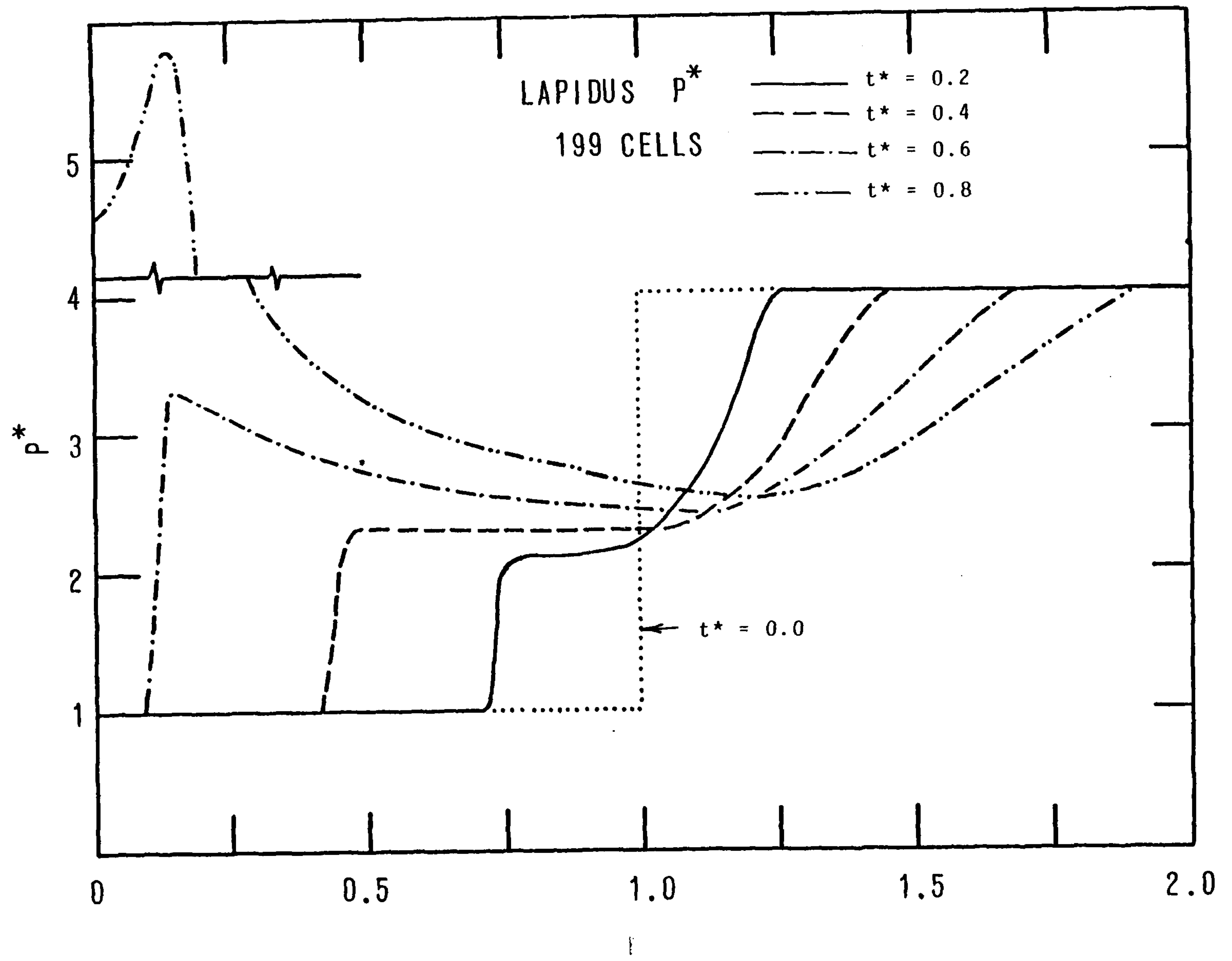

Figure 3

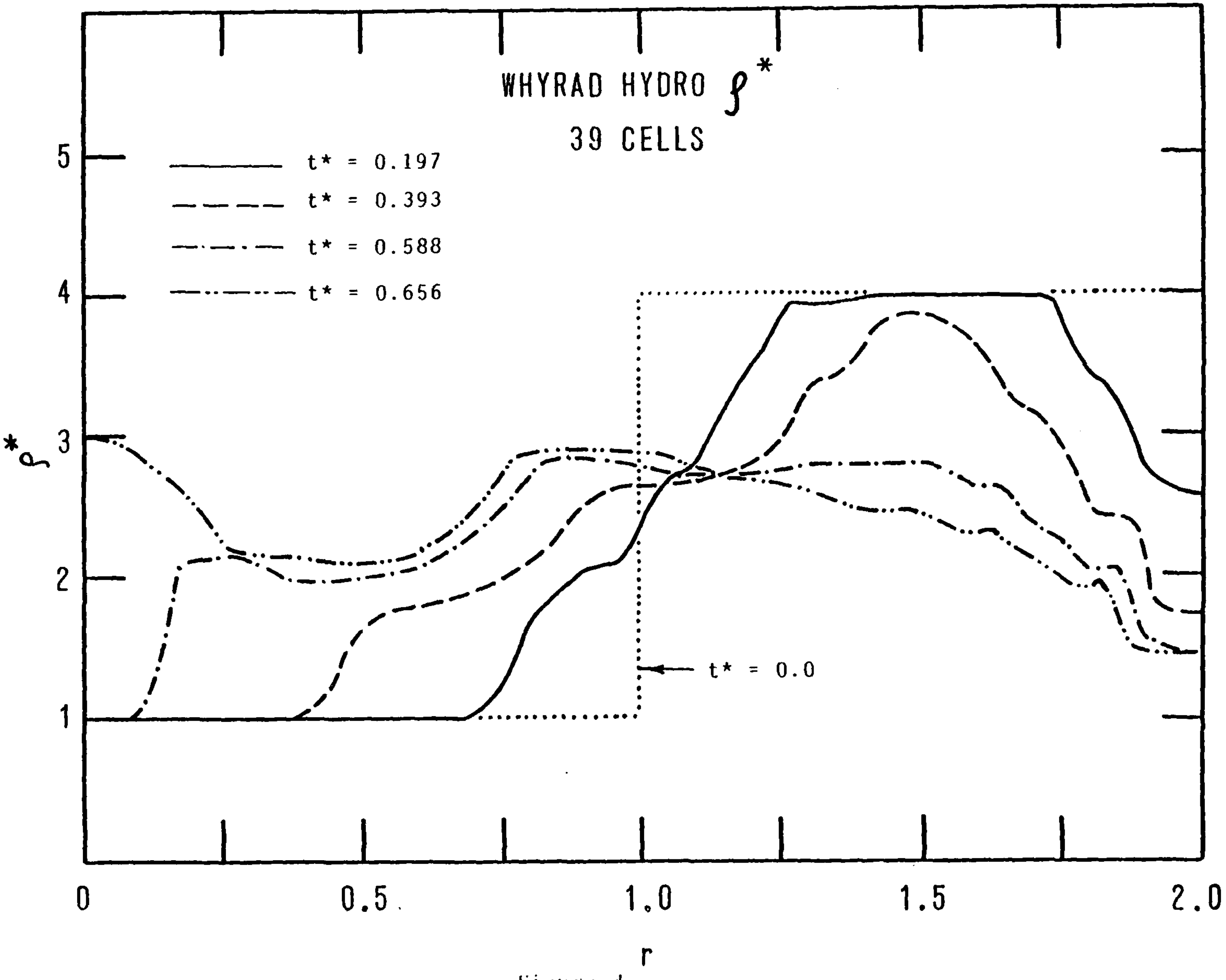
WHYRAD HYDRO ρ*
39 CELLS
t* = 0.197
t* = 0.393
t* = 0.588
t* = 0.656
t* = 0.0
ρ*
5
4
3
2
1
0
0.5
1.0
1.5
2.0
r

Figure 4

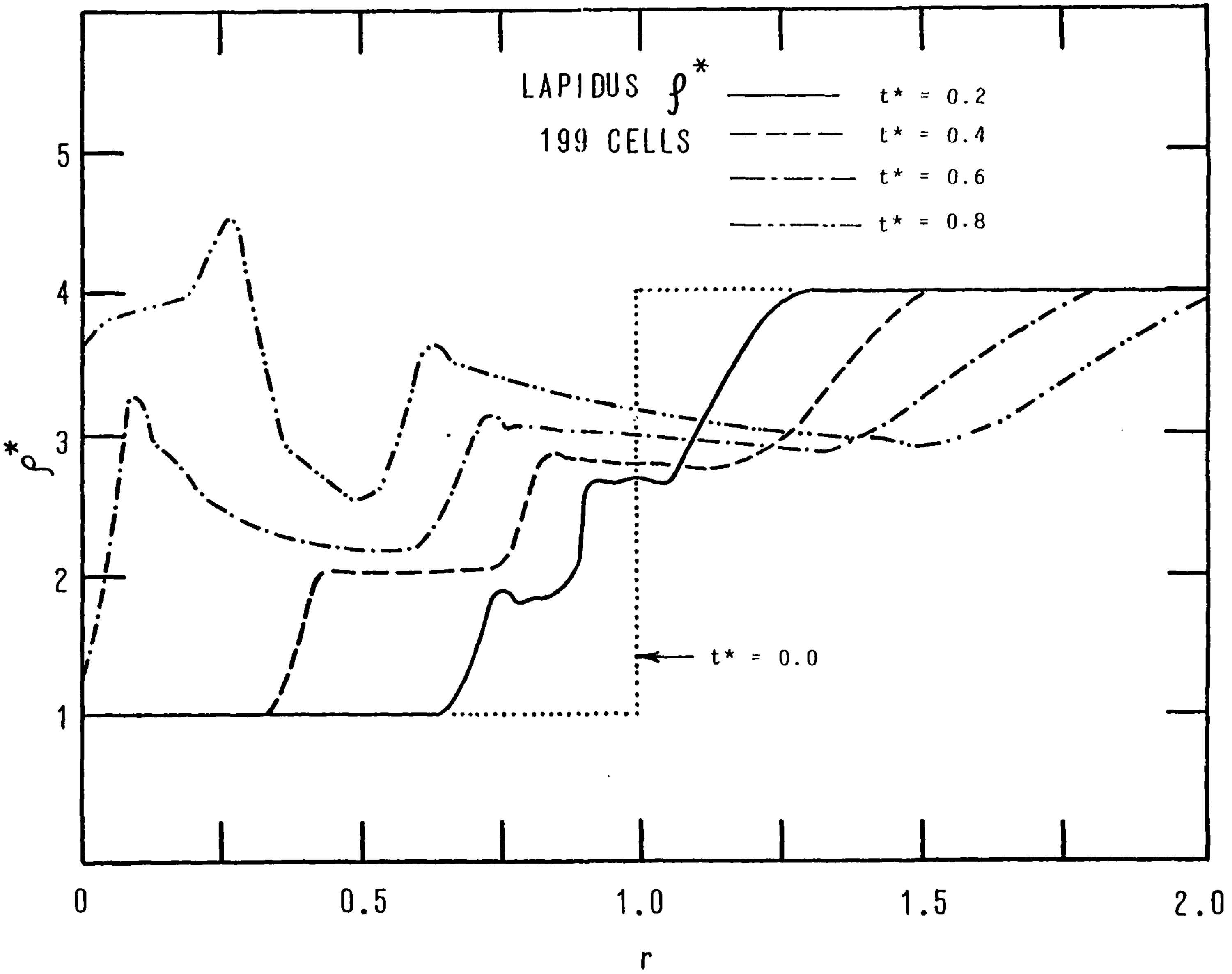
LAPIDUS ρ^*
199 CELLS
t* = 0.2
t* = 0.4
t* = 0.6
t* = 0.8
t* = 0.0
ρ^*
5
4
3
2
1
0
0.5
1.0
1.5
2.0
r

Figure 5

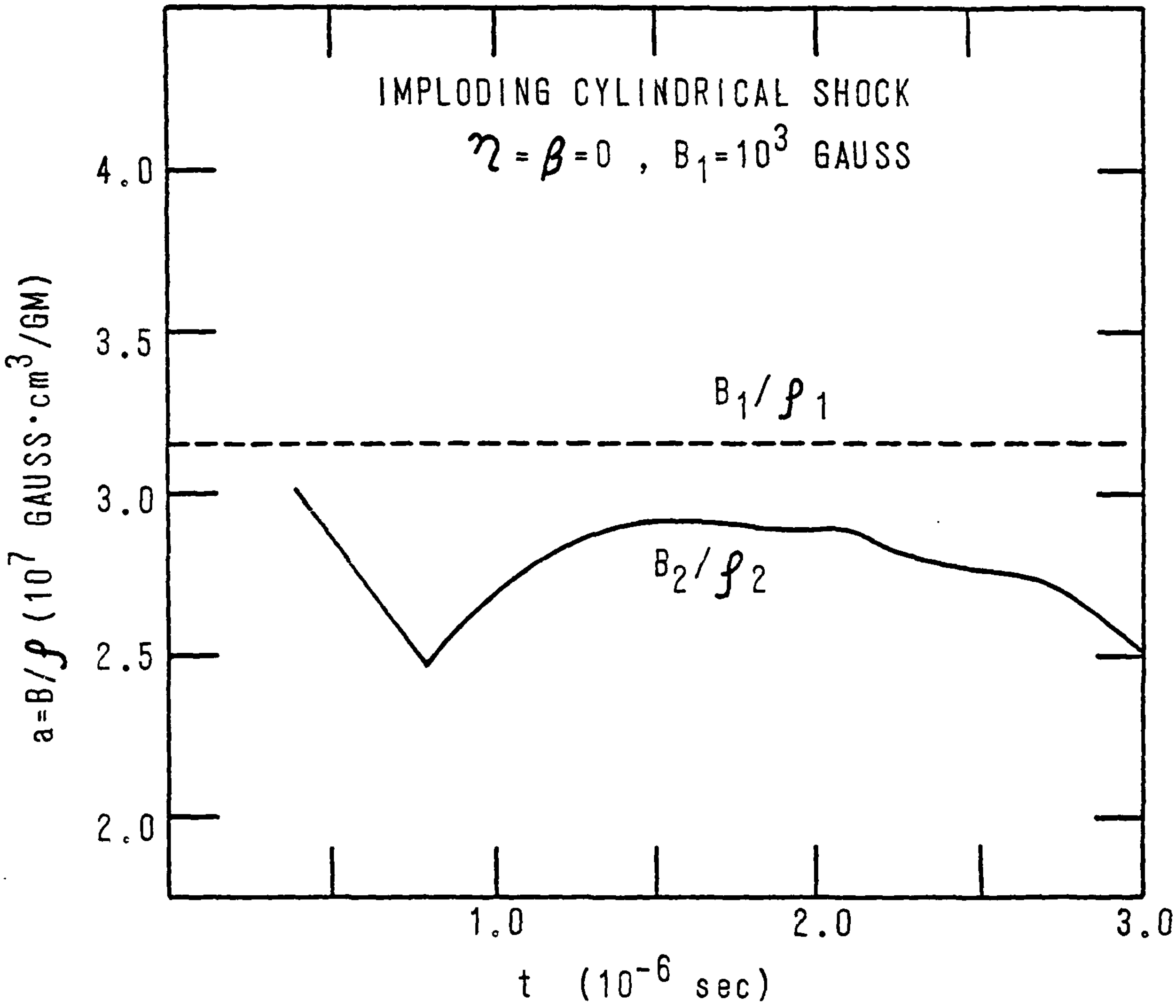
IMPLODING CYLINDRICAL SHOCK
$\eta = \beta = 0$, $B_1 = 10^3$ GAUSS
B_1/ρ_1
B_2/ρ_2
4.0
3.5
3.0
2.5
2.0
$a = B/\rho$ (10^7 GAUSS·cm^3/GM)
1.0
2.0
3.0
t (10^{-6} sec)

Figure 6

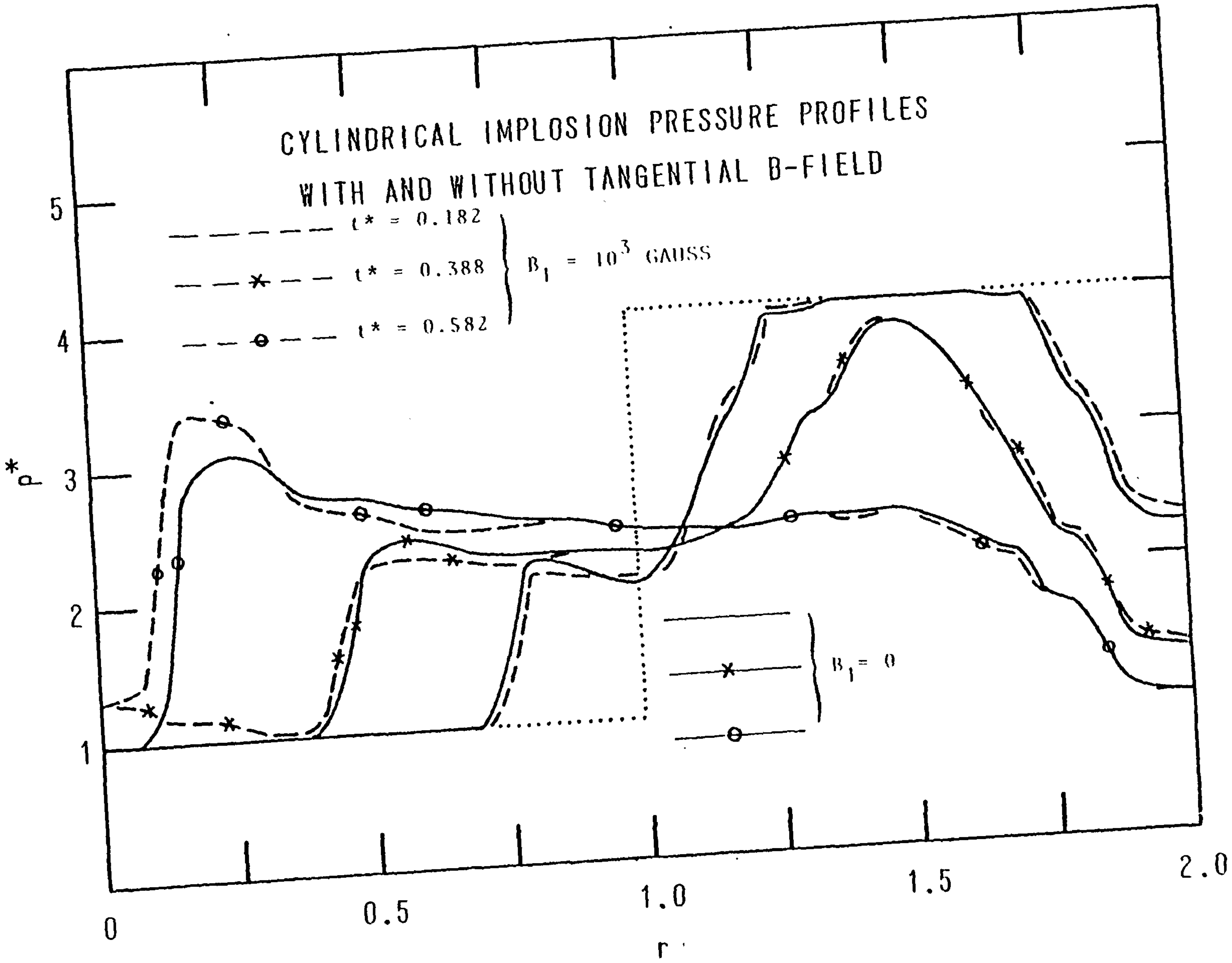
CYLINDRICAL IMPLOSION PRESSURE PROFILES
WITH AND WITHOUT TANGENTIAL B-FIELD
t* = 0.182
t* = 0.388
t* = 0.582
$B_1 = 10^3$ GAUSS
$B_1 = 0$
p^*
1
2
3
4
5
0
0.5
1.0
1.5
2.0
r

Figure 7

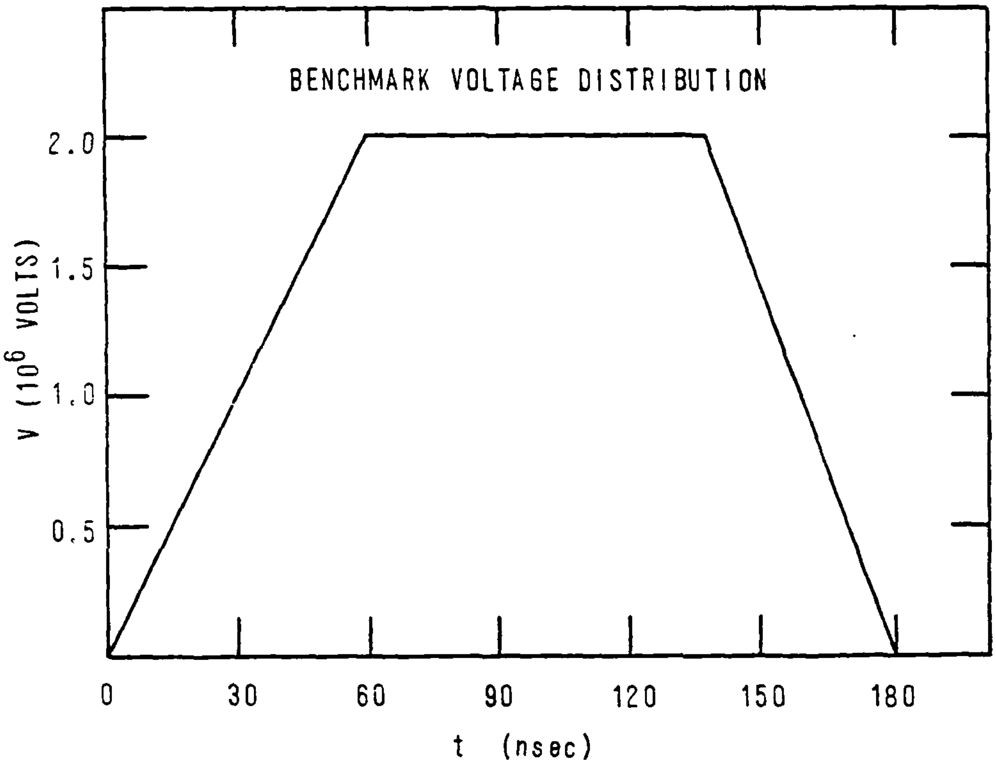
BENCHMARK VOLTAGE DISTRIBUTION
V (10^6 VOLTS)
2.0
1.5
1.0
0.5
0
30
60
90
120
150
180
t (nsec)

Figure 8

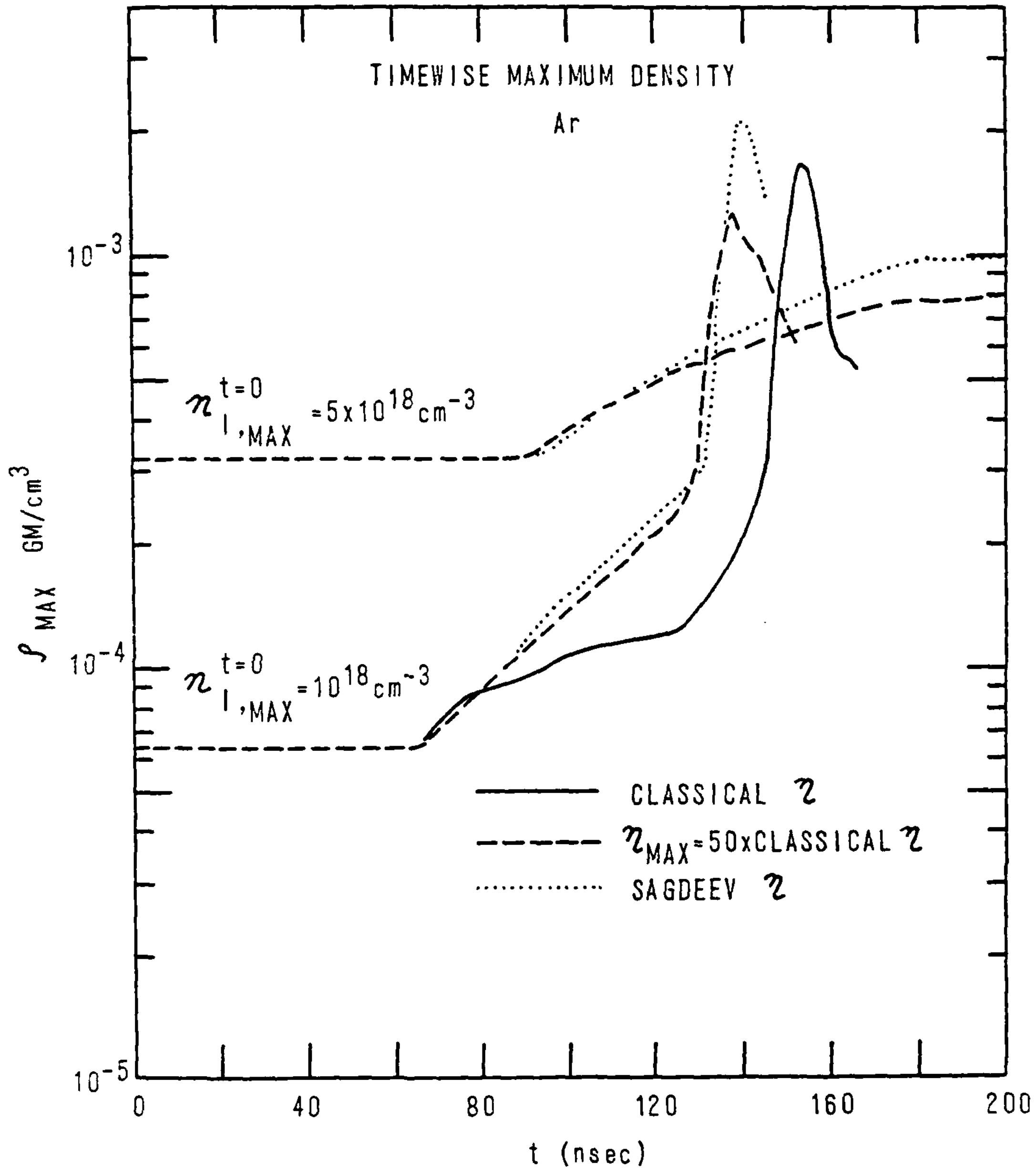
TIMEWISE MAXIMUM DENSITY
Ar
$\eta^{t=0}_{I,MAX} = 5\times10^{18}\,cm^{-3}$
$\eta^{t=0}_{I,MAX} = 10^{18}\,cm^{-3}$
ρ_{MAX} GM/cm^3
10^{-3}
10^{-4}
10^{-5}
0
40
80
120
160
200
t (nsec)
CLASSICAL η
η_{MAX}=50xCLASSICAL η
SAGDEEV η

Figure 9

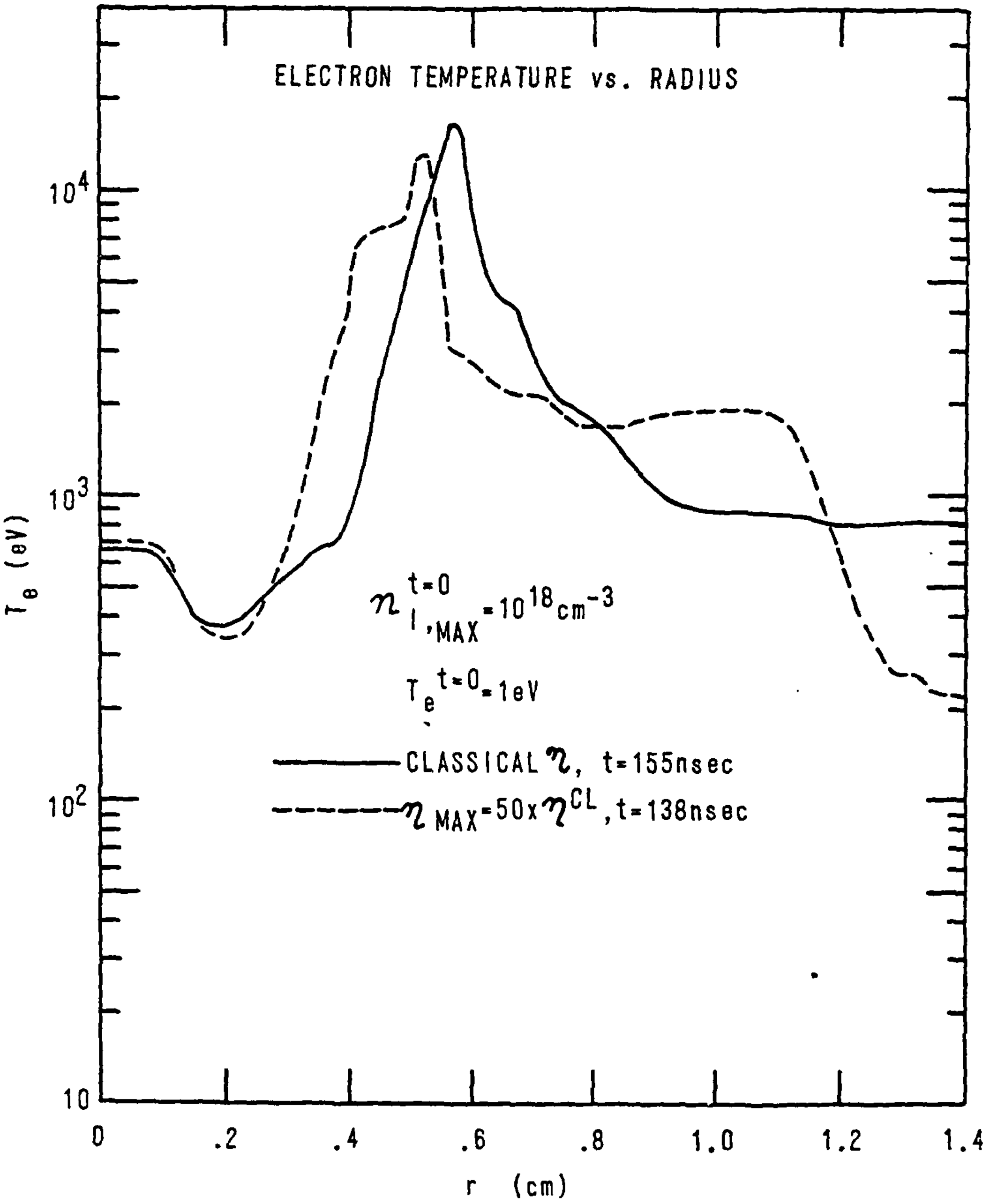

ELECTRON TEMPERATURE vs. RADIUS
T_e (eV)
10
10^2
10^3
10^4
0
.2
.4
.6
.8
1.0
1.2
1.4
r (cm)
$n_{I,MAX}^{t=0} = 10^{18} cm^{-3}$
$T_e^{t=0} = 1 eV$
CLASSICAL η, t=155nsec
$\eta_{MAX} = 50 \times \eta^{CL}$, t=138nsec

Figure 10

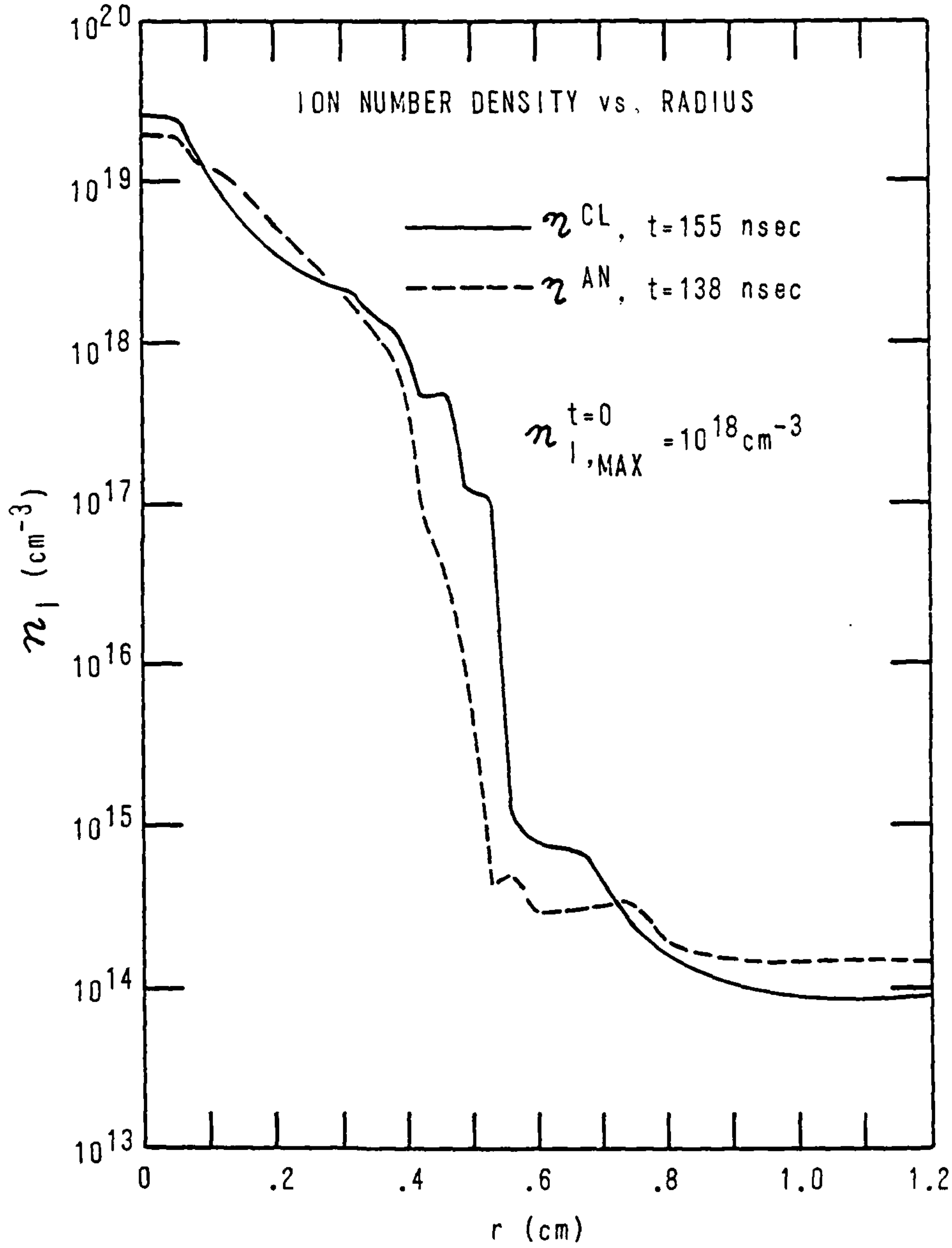
ION NUMBER DENSITY vs. RADIUS
n^{CL}, t=155 nsec
n^{AN}, t=138 nsec
$n_{I,MAX}^{t=0} = 10^{18} cm^{-3}$
n_I (cm^{-3})
10^{20}
10^{19}
10^{18}
10^{17}
10^{16}
10^{15}
10^{14}
10^{13}
0
.2
.4
.6
.8
1.0
1.2
r (cm)

Figure 17

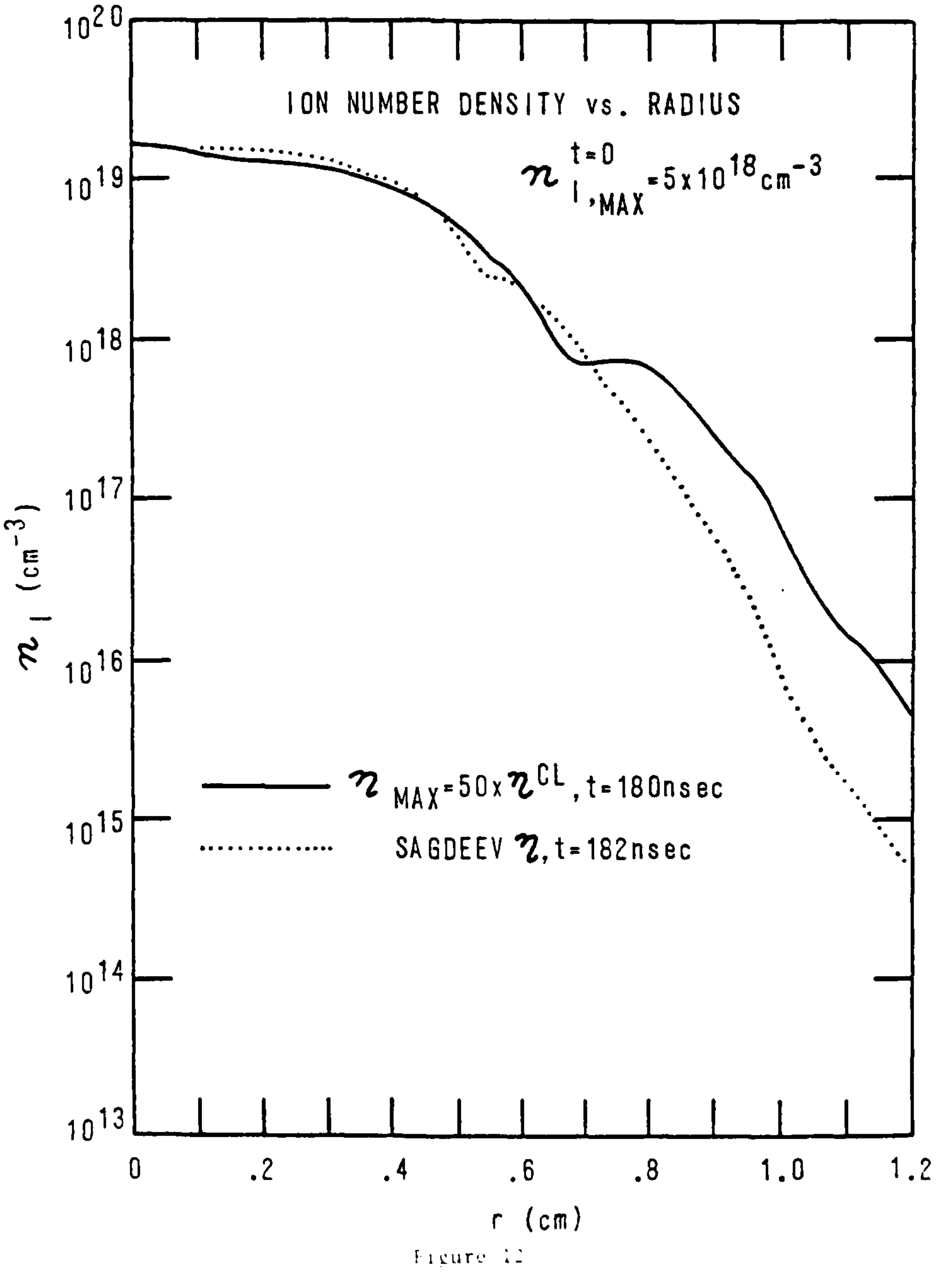
ION NUMBER DENSITY vs. RADIUS
$n_{I,MAX}^{t=0}=5\times10^{18}cm^{-3}$
$n_{MAX}=50\times n^{CL}$, t=180nsec
SAGDEEV n, t=182nsec
10^{20}
10^{19}
10^{18}
10^{17}
10^{16}
10^{15}
10^{14}
10^{13}
n_I (cm^{-3})
0
.2
.4
.6
.8
1.0
1.2
r (cm)

Figure 12

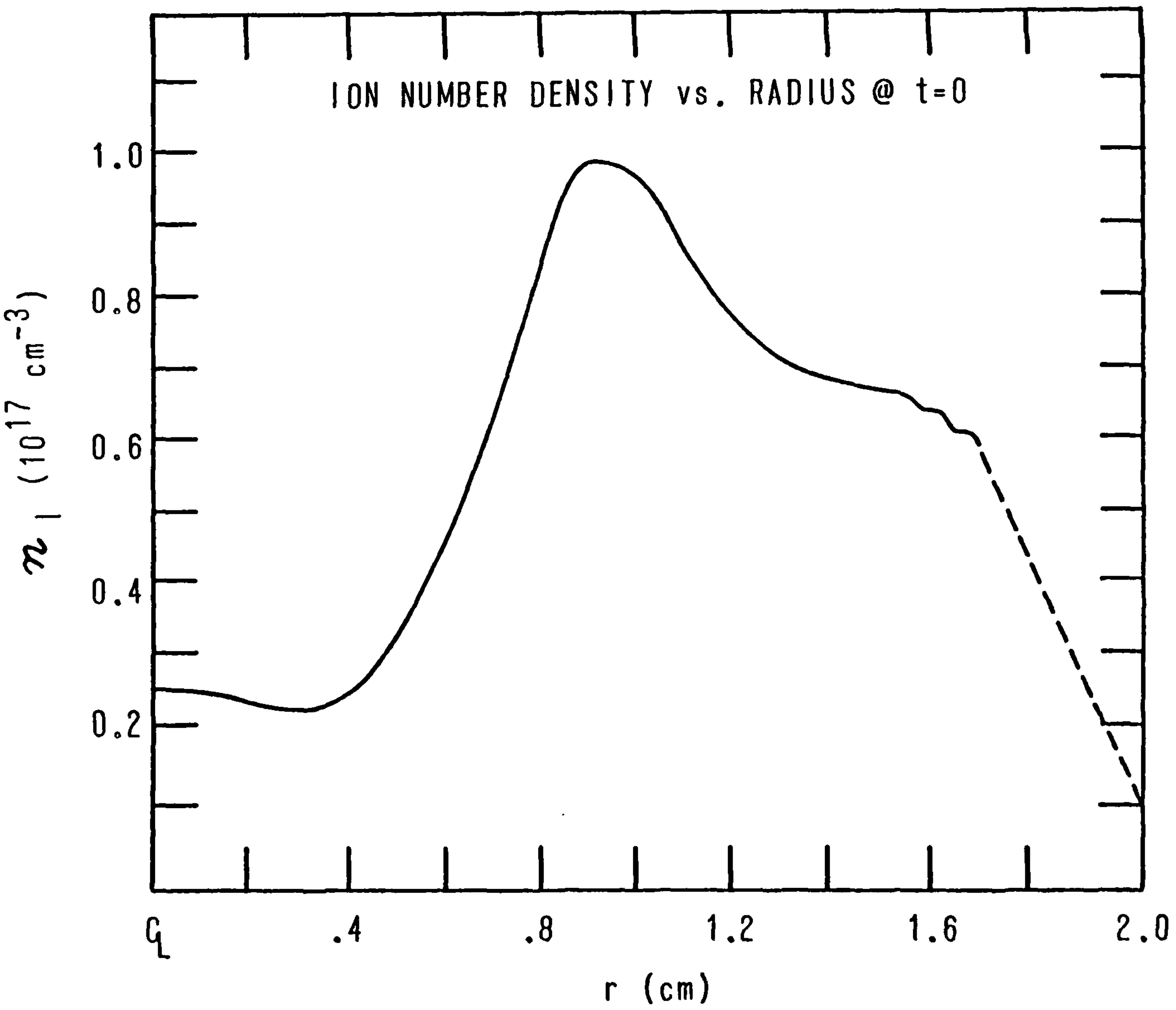
ION NUMBER DENSITY vs. RADIUS @ t=0
$n_I\ (10^{17}\ \mathrm{cm}^{-3})$
1.0
0.8
0.6
0.4
0.2
℄
.4
.8
1.2
1.6
2.0
r (cm)

Figure 13

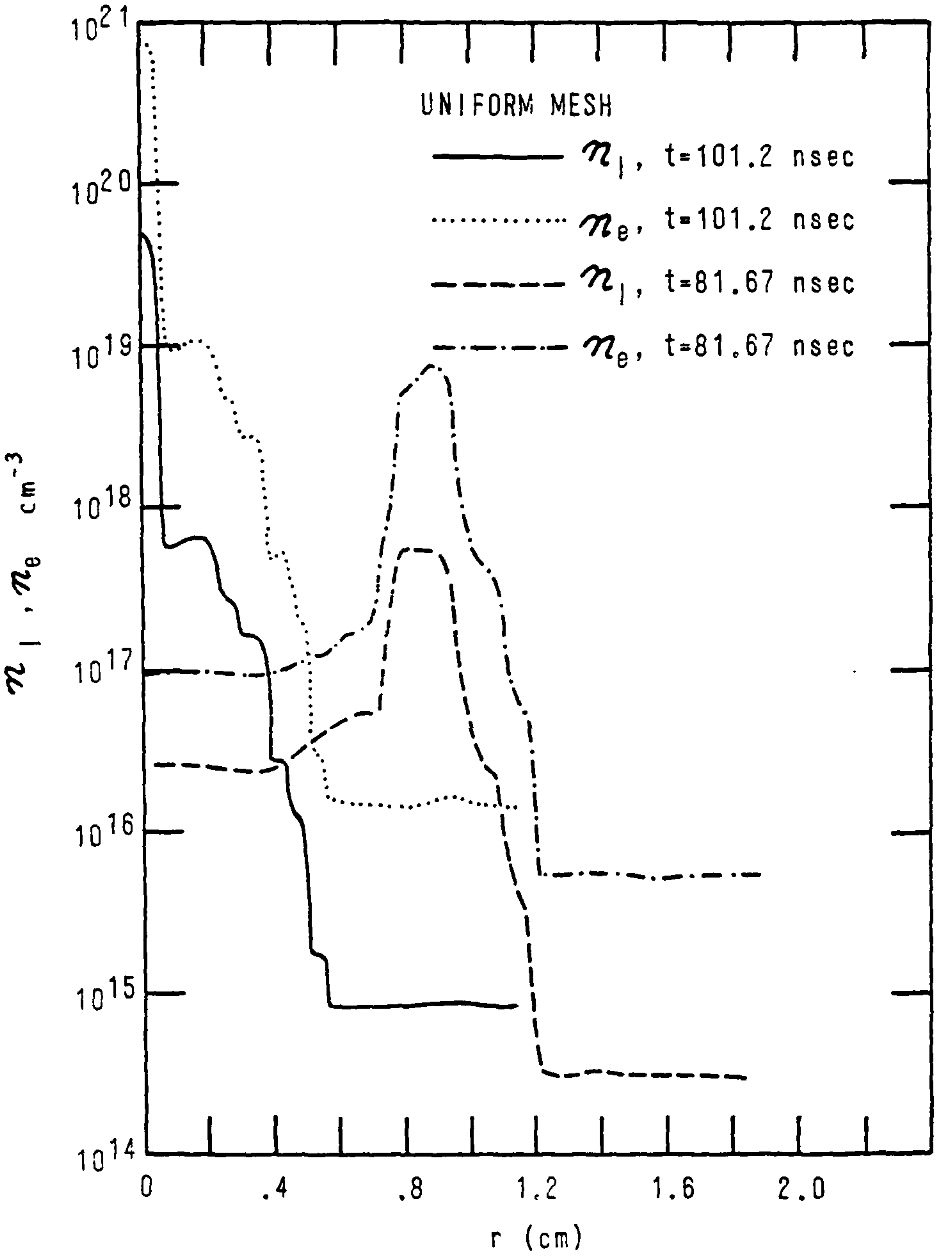
UNIFORM MESH
n_I, t=101.2 nsec
n_e, t=101.2 nsec
n_I, t=81.67 nsec
n_e, t=81.67 nsec
10^{21}
10^{20}
10^{19}
10^{18}
10^{17}
10^{16}
10^{15}
10^{14}
n_I, n_e cm^{-3}
0
.4
.8
1.2
1.6
2.0
r (cm)

Figure 14

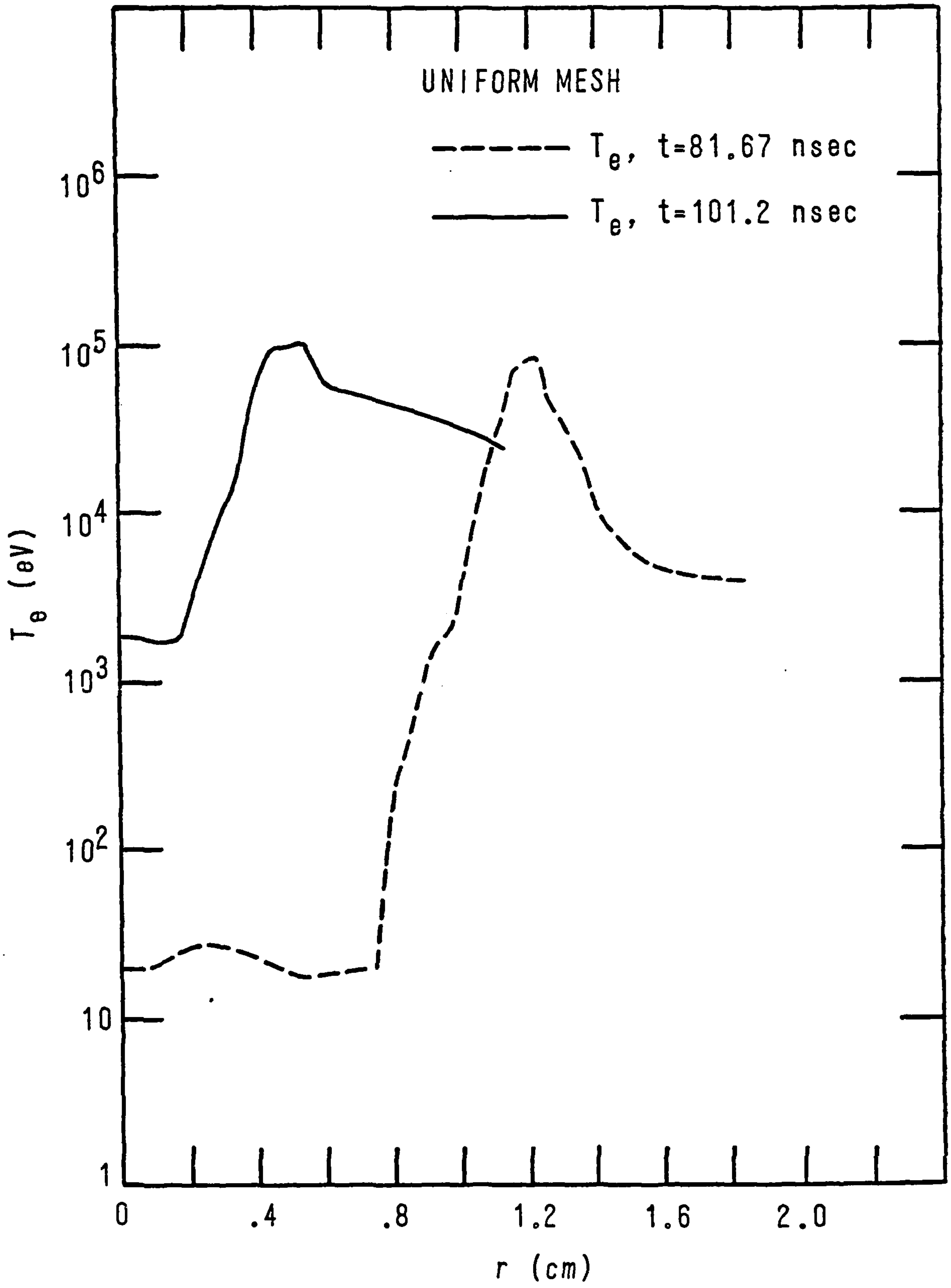
UNIFORM MESH
T_e, t=81.67 nsec
T_e, t=101.2 nsec
10^6
10^5
10^4
10^3
10^2
10
1
T_e (eV)
0
.4
.8
1.2
1.6
2.0
r (cm)

Figure 15

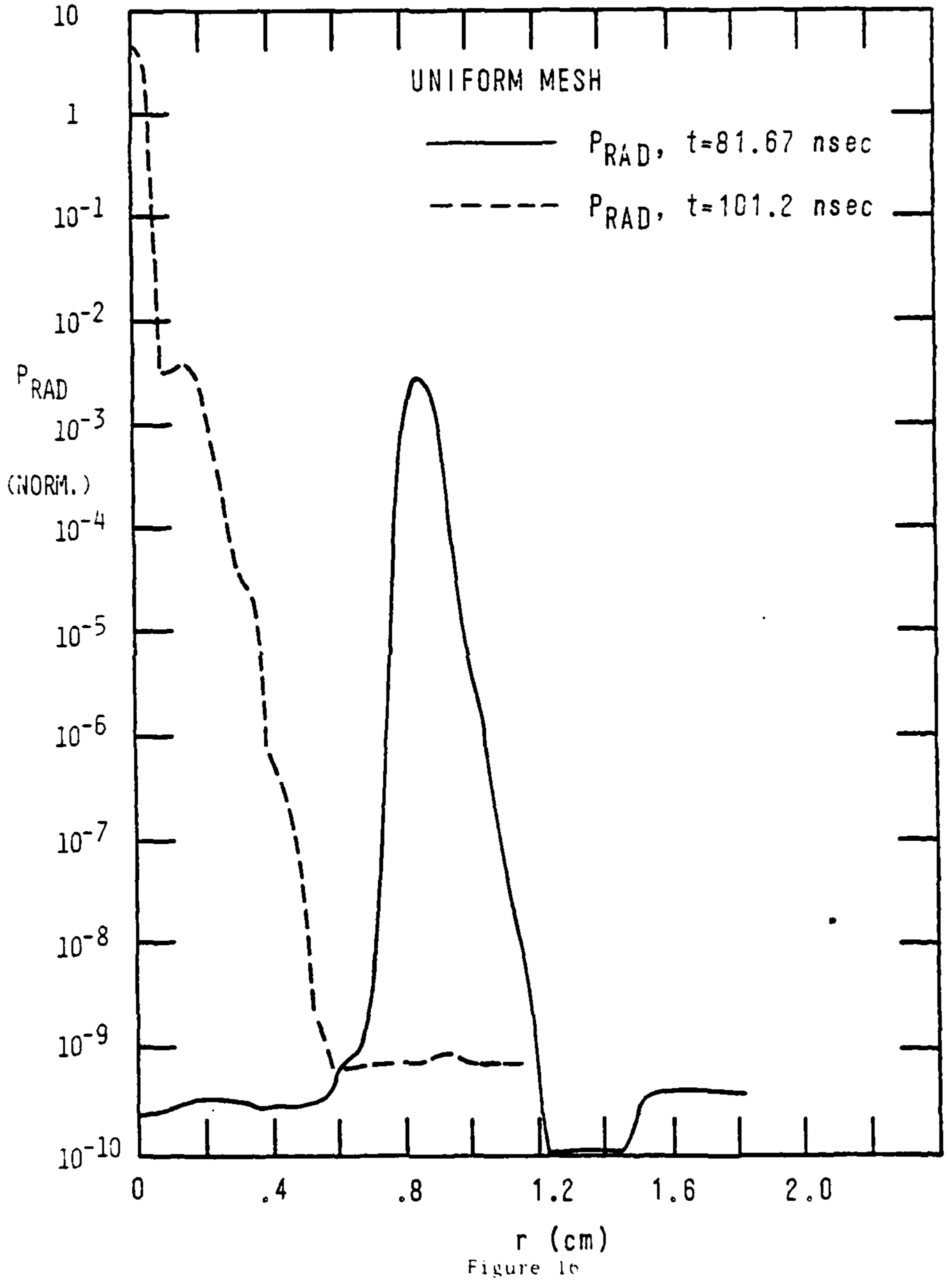
UNIFORM MESH
P_{RAD}, t=81.67 nsec
P_{RAD}, t=101.2 nsec
10
1
10^{-1}
10^{-2}
P_{RAD}
10^{-3}
(NORM.)
10^{-4}
10^{-5}
10^{-6}
10^{-7}
10^{-8}
10^{-9}
10^{-10}
0
.4
.8
1.2
1.6
2.0
r (cm)

Figure 1c

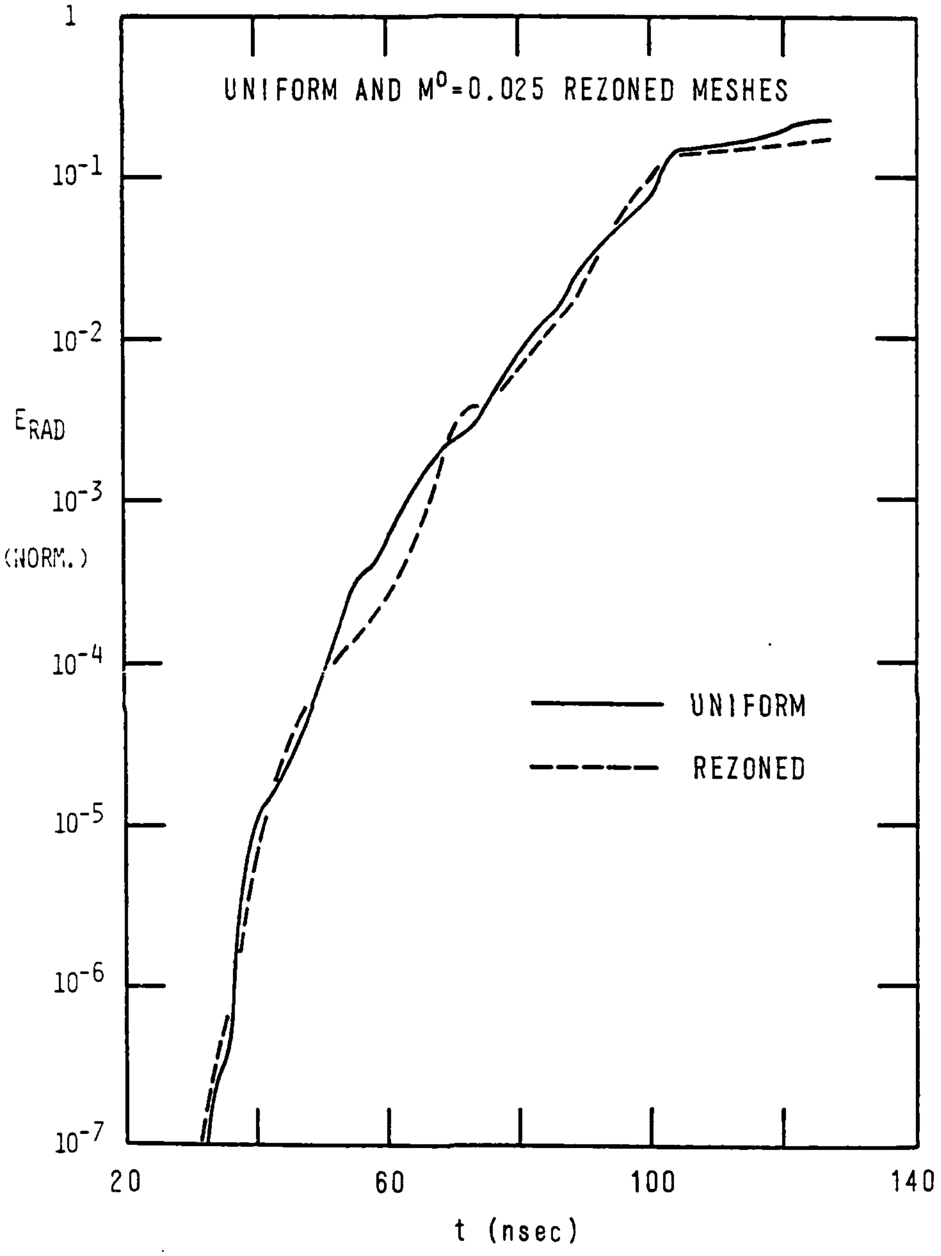
UNIFORM AND $M^0=0.025$ REZONED MESHES
1
10^{-1}
10^{-2}
E_{RAD}
10^{-3}
(NORM.)
10^{-4}
10^{-5}
10^{-6}
10^{-7}
UNIFORM
REZONED
20
60
100
140
t (nsec)

Figure 17

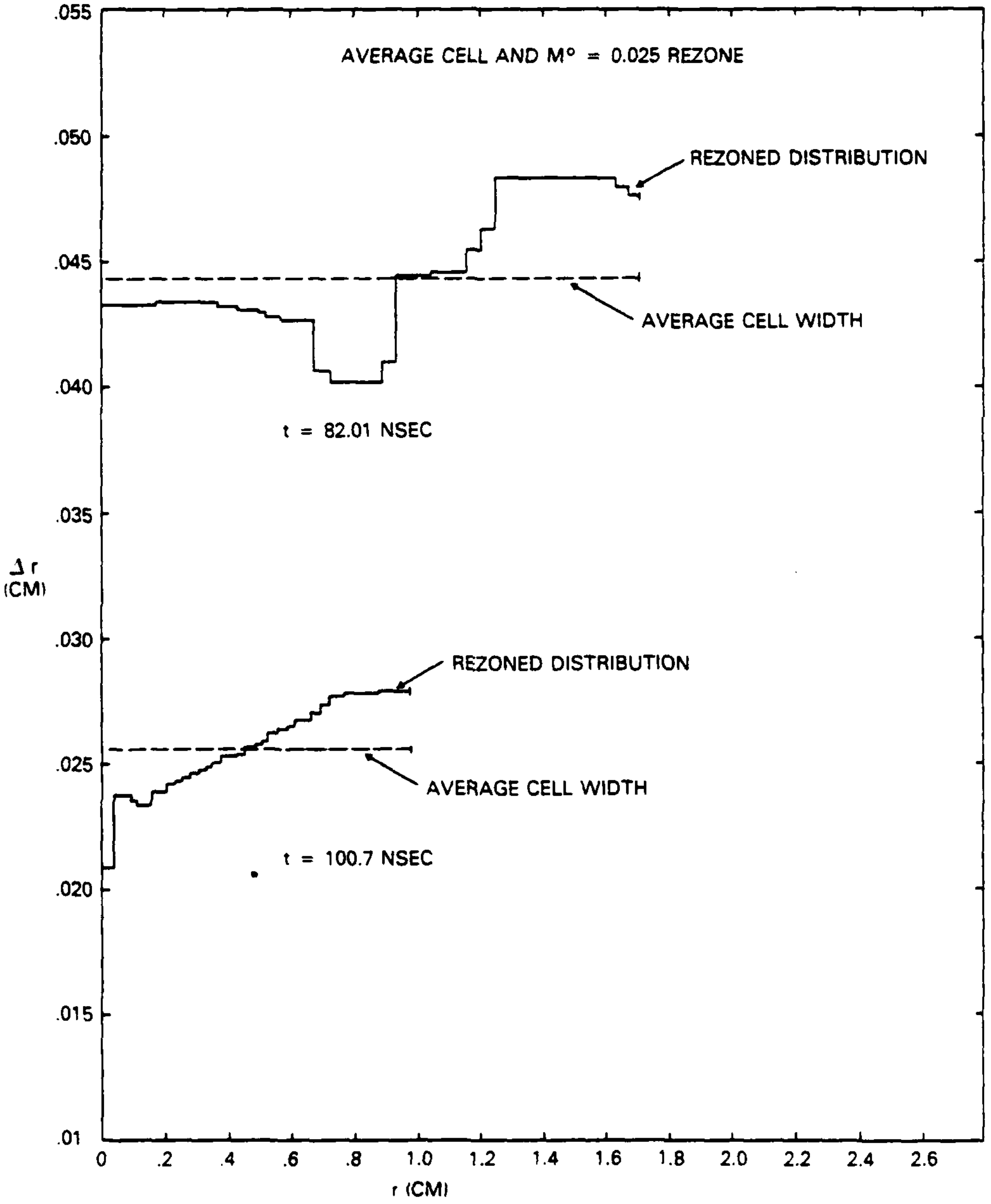
AVERAGE CELL AND M° = 0.025 REZONE
REZONED DISTRIBUTION
AVERAGE CELL WIDTH
t = 82.01 NSEC
REZONED DISTRIBUTION
AVERAGE CELL WIDTH
t = 100.7 NSEC
Δr (CM)
.055
.050
.045
.040
.035
.030
.025
.020
.015
.01
0
.2
.4
.6
.8
1.0
1.2
1.4
1.6
1.8
2.0
2.2
2.4
2.6
r (CM)

Figure 18

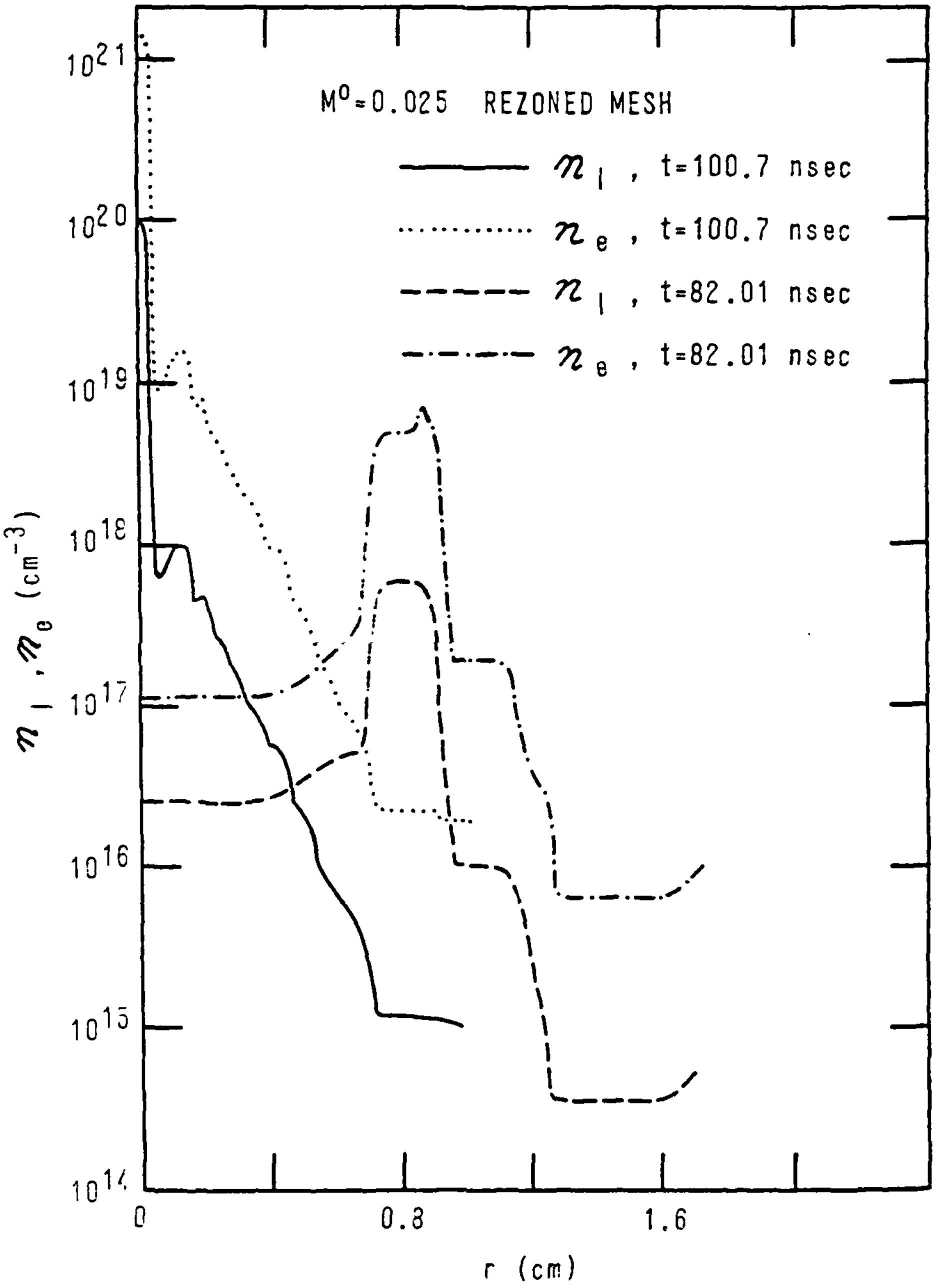
M^0=0.025 REZONED MESH
n_I , t=100.7 nsec
n_e , t=100.7 nsec
n_I , t=82.01 nsec
n_e , t=82.01 nsec
10^{21}
10^{20}
10^{19}
10^{18}
10^{17}
10^{16}
10^{15}
10^{14}
n_I , n_e (cm^{-3})
0
0.8
1.6
r (cm)

Figure 13

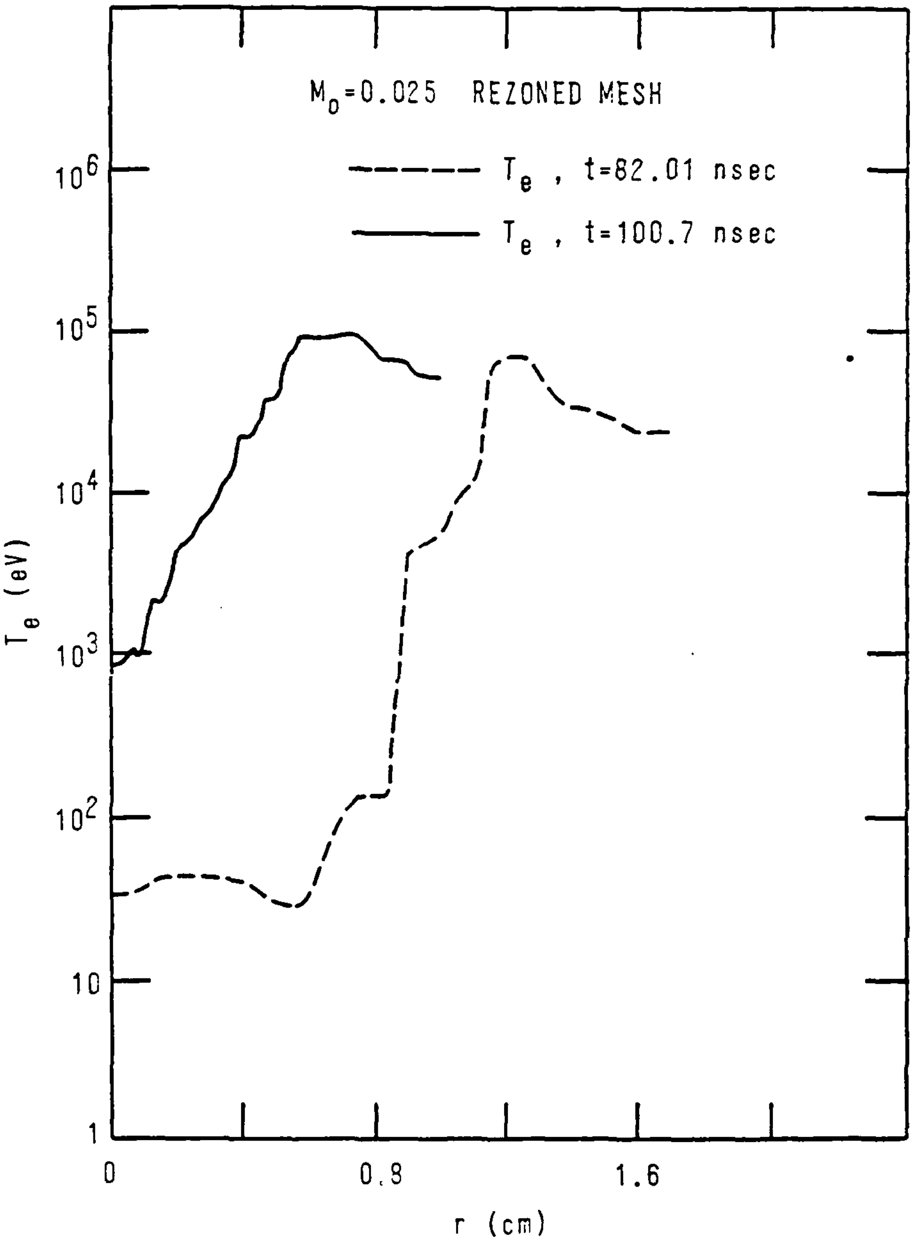
M_0=0.025 REZONED MESH
T_e , t=82.01 nsec
T_e , t=100.7 nsec
10^6
10^5
10^4
10^3
10^2
10
1
T_e (eV)
0
0.8
1.6
r (cm)

Figure 2[illegible]

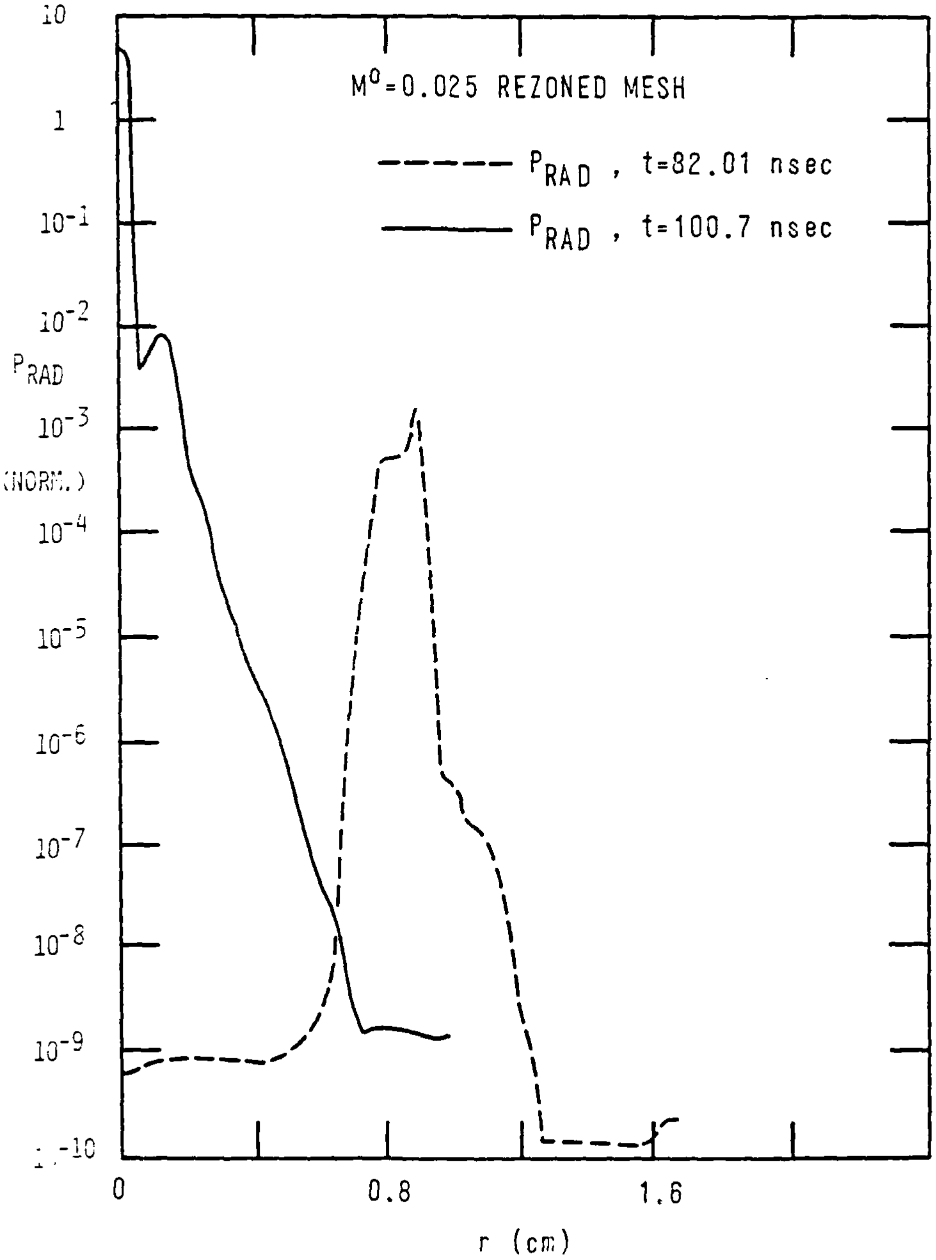

M^0=0.025 REZONED MESH
P_{RAD}, t=82.01 nsec
P_{RAD}, t=100.7 nsec
P_{RAD} (NORM.)
10
1
10^{-1}
10^{-2}
10^{-3}
10^{-4}
10^{-5}
10^{-6}
10^{-7}
10^{-8}
10^{-9}
10^{-10}
0
0.8
1.6
r (cm)

Figure 21

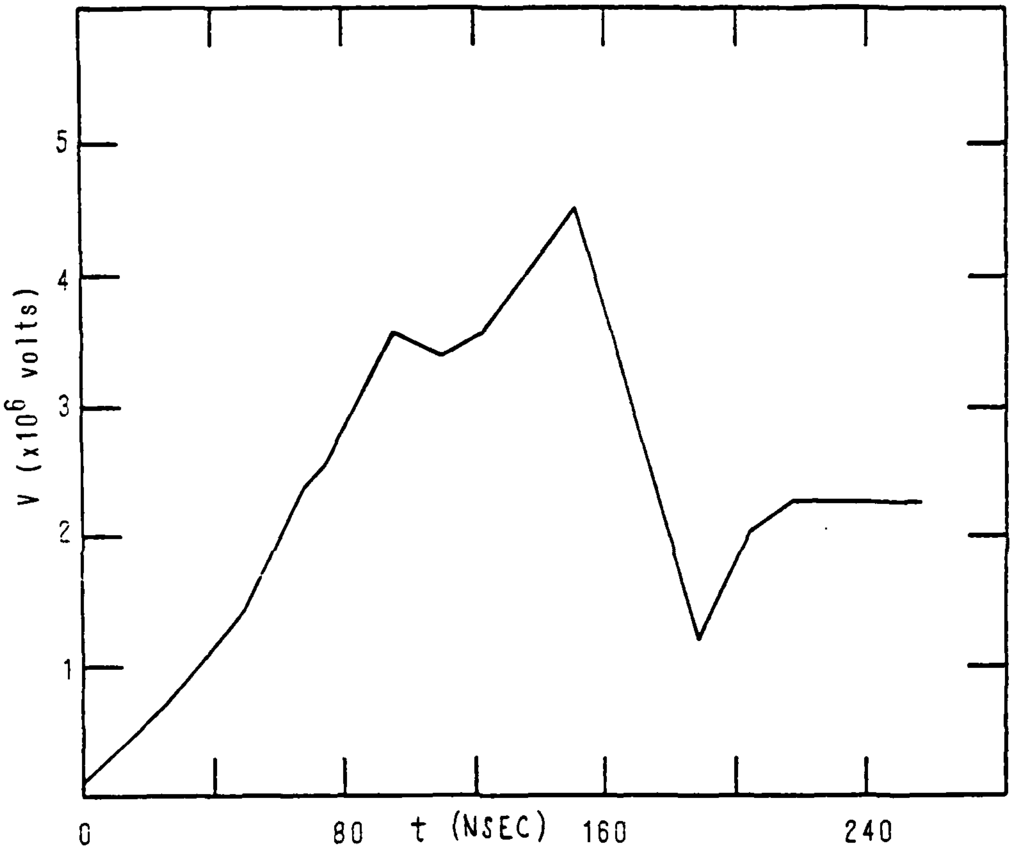

SPLAT MODEL VOLTAGE PROFILE

Figure 11

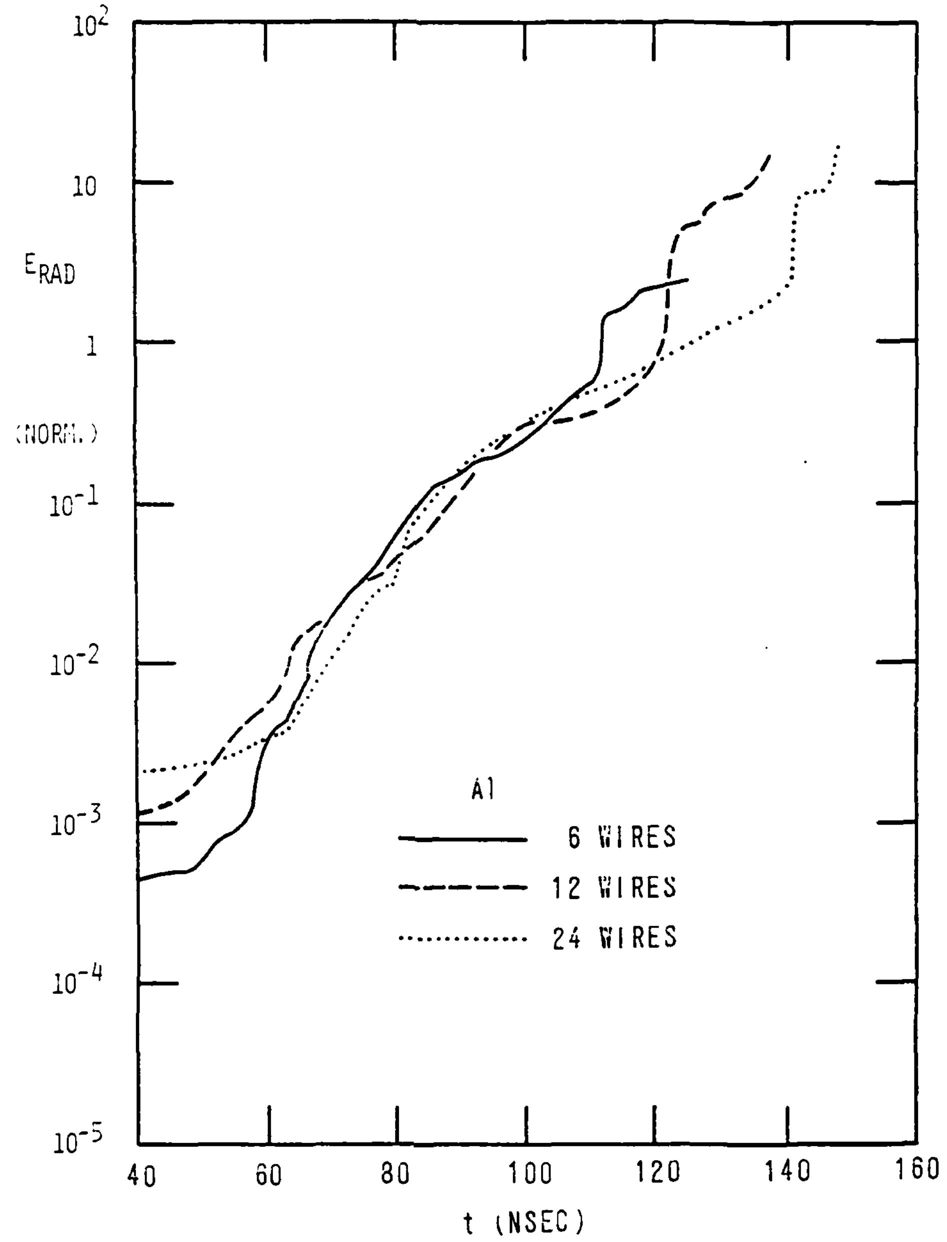
10^2
10
E_{RAD}
1
(NORM.)
10^{-1}
10^{-2}
10^{-3}
10^{-4}
10^{-5}
40
60
80
100
120
140
160
t (NSEC)
Al
6 WIRES
12 WIRES
24 WIRES

Figure 27

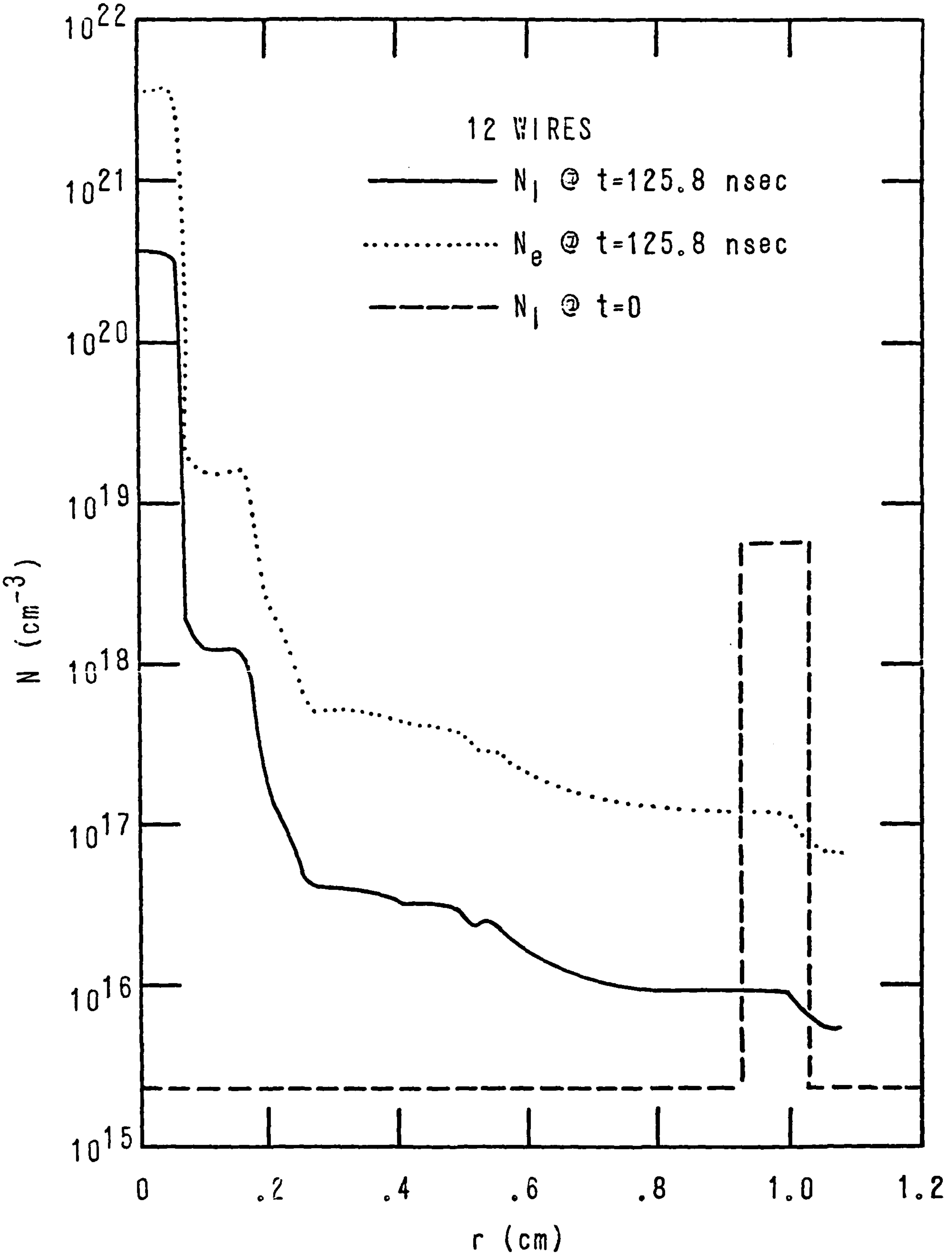

10^{22}
10^{21}
10^{20}
10^{19}
10^{18}
10^{17}
10^{16}
10^{15}
N (cm^{-3})
12 WIRES
N_I @ t=125.8 nsec
N_e @ t=125.8 nsec
N_I @ t=0
0
.2
.4
.6
.8
1.0
1.2
r (cm)

Figure 24

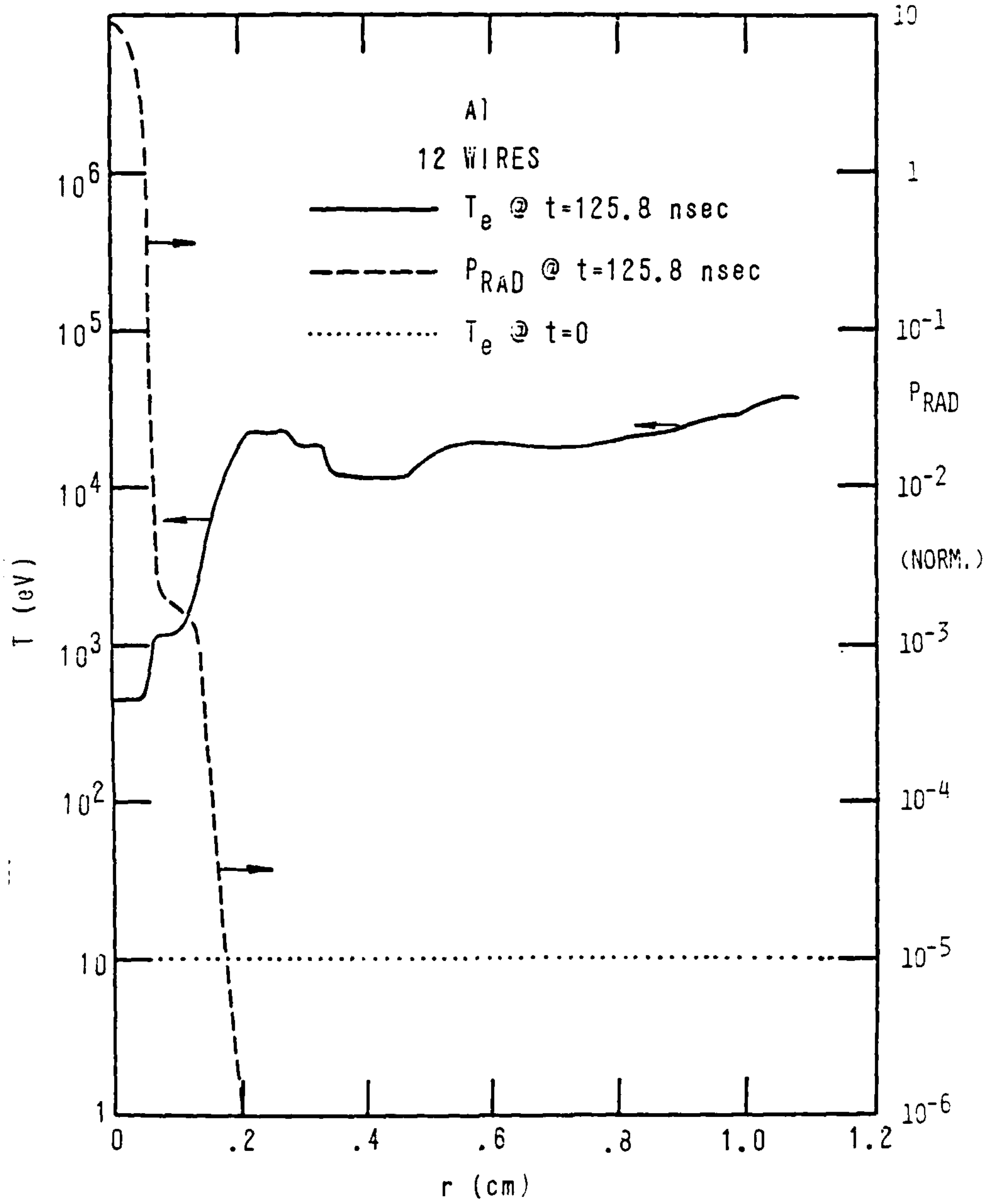
Al
12 WIRES
T_e @ t=125.8 nsec
P_{RAD} @ t=125.8 nsec
T_e @ t=0
T (eV)
1
10
10^2
10^3
10^4
10^5
10^6
P_{RAD} (NORM.)
10^{-6}
10^{-5}
10^{-4}
10^{-3}
10^{-2}
10^{-1}
1
10
0
.2
.4
.6
.8
1.0
1.2
r (cm)

Figure 25

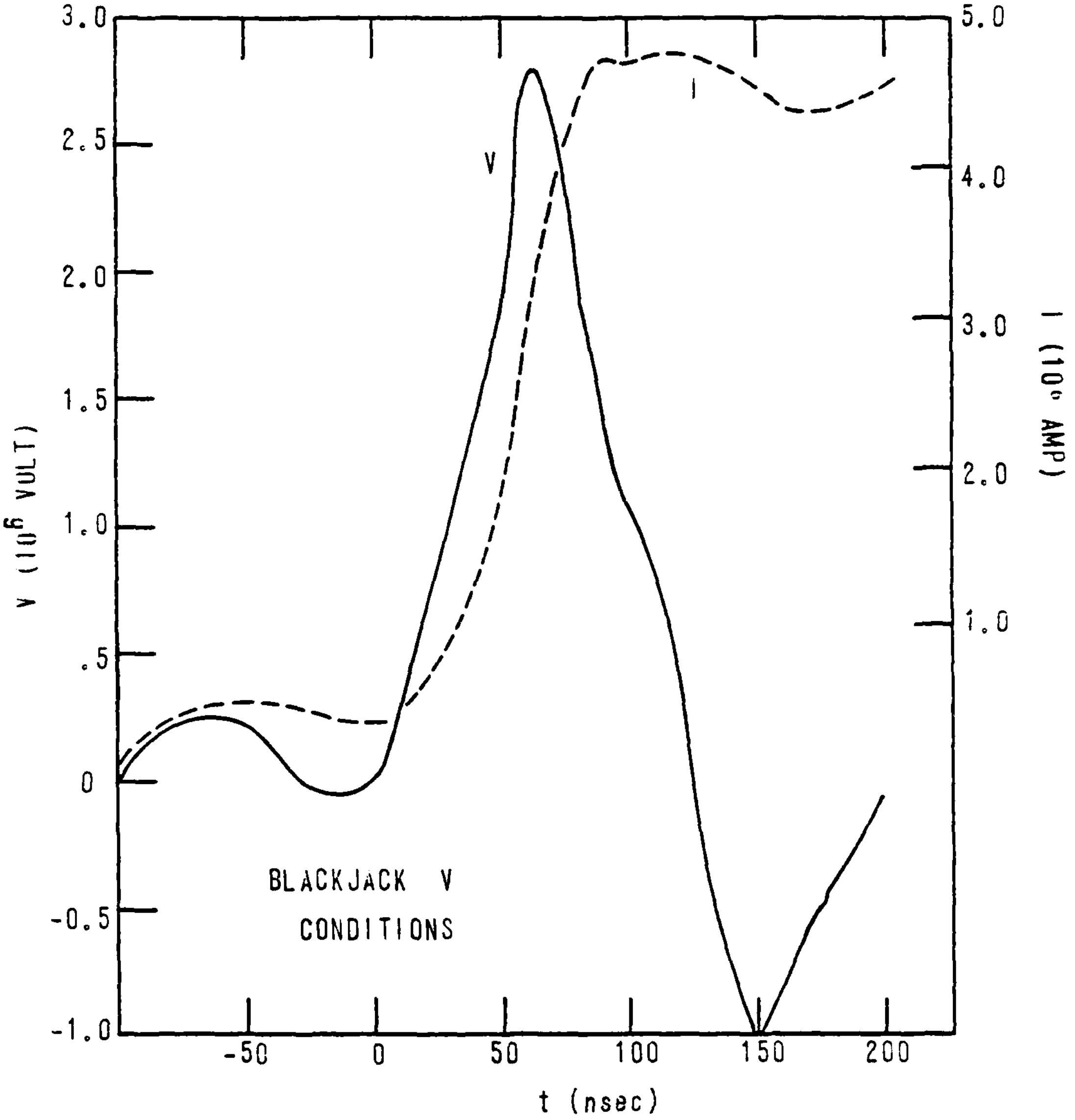
3.0
2.5
2.0
1.5
1.0
.5
0
-0.5
-1.0
V (10^6 VOLT)
5.0
4.0
3.0
2.0
1.0
I (10^6 AMP)
-50
0
50
100
150
200
t (nsec)
V
I
BLACKJACK V
CONDITIONS

Figure 26

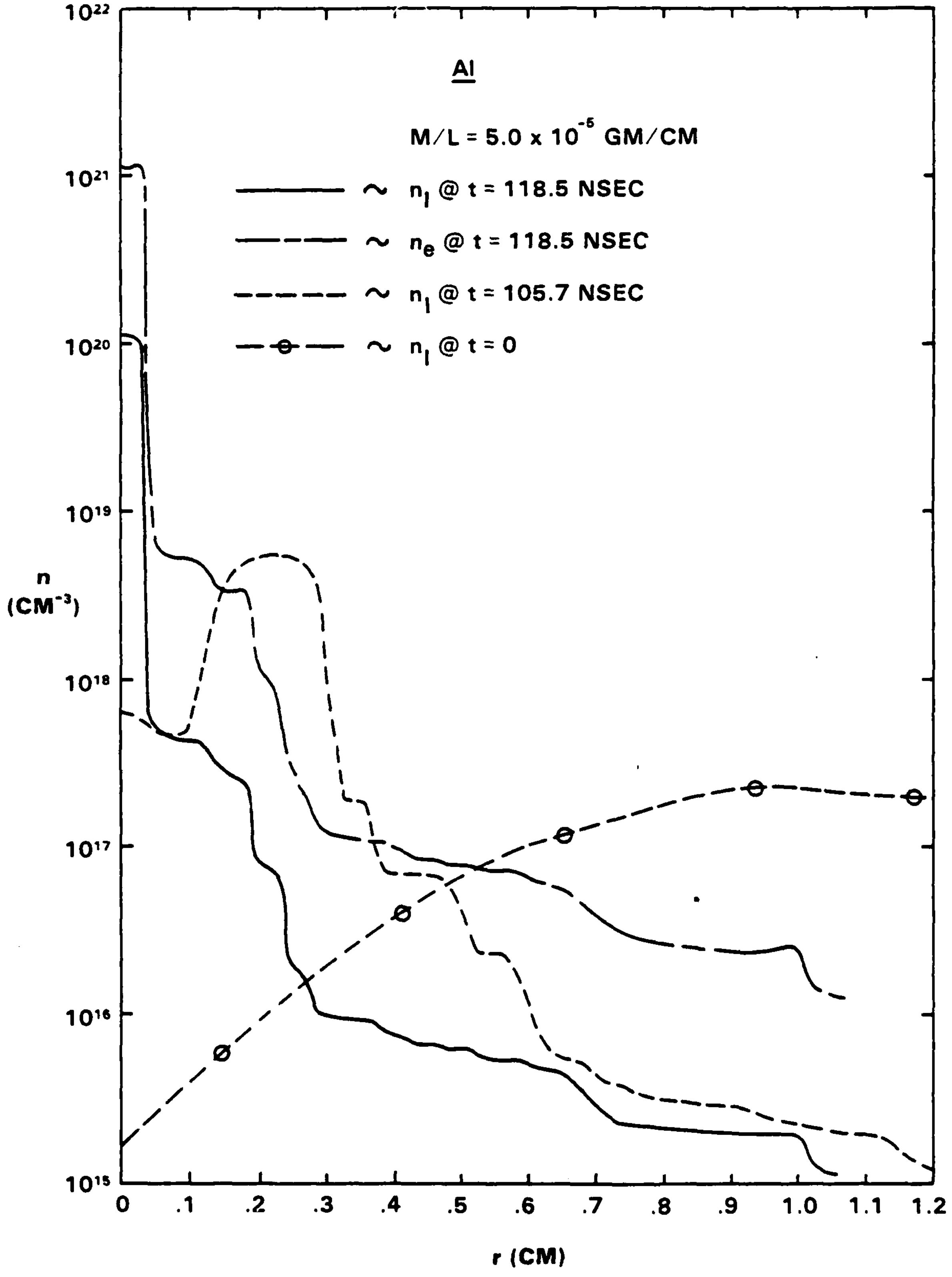
Al
M/L = 5.0 x 10^-5 GM/CM
~ n_I @ t = 118.5 NSEC
~ n_e @ t = 118.5 NSEC
~ n_I @ t = 105.7 NSEC
~ n_I @ t = 0
n (CM^-3)
10^22
10^21
10^20
10^19
10^18
10^17
10^16
10^15
0
.1
.2
.3
.4
.5
.6
.7
.8
.9
1.0
1.1
1.2
r (CM)

Figure 27

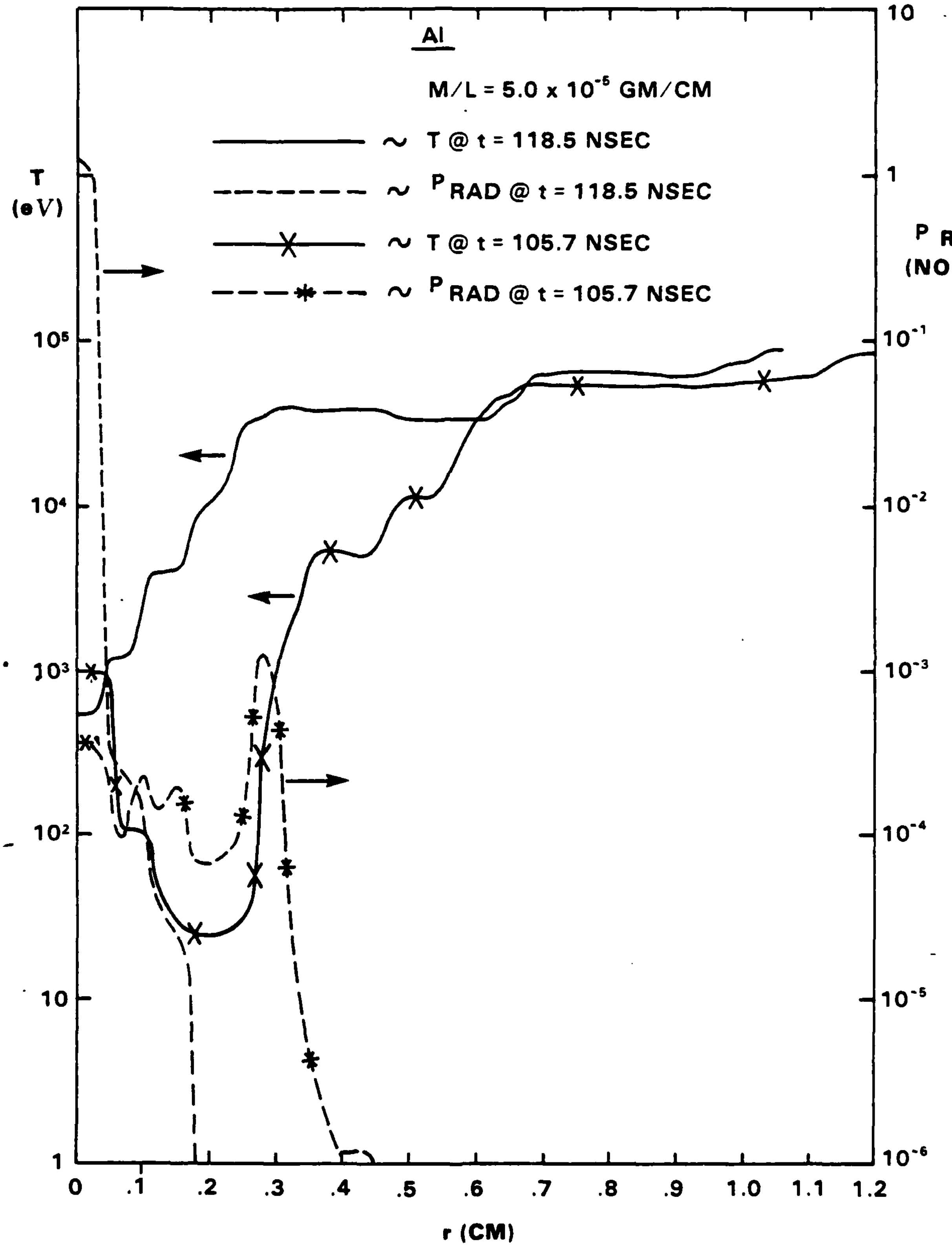
Al
M/L = 5.0 x 10⁻⁵ GM/CM
~ T @ t = 118.5 NSEC
~ P RAD @ t = 118.5 NSEC
~ T @ t = 105.7 NSEC
~ P RAD @ t = 105.7 NSEC
T (eV)
10⁵
10⁴
10³
10²
10
1
10
1
10⁻¹
10⁻²
10⁻³
10⁻⁴
10⁻⁵
10⁻⁶
P RAD (NORM.
0
.1
.2
.3
.4
.5
.6
.7
.8
.9
1.0
1.1
1.2
r (CM)

Figure 28

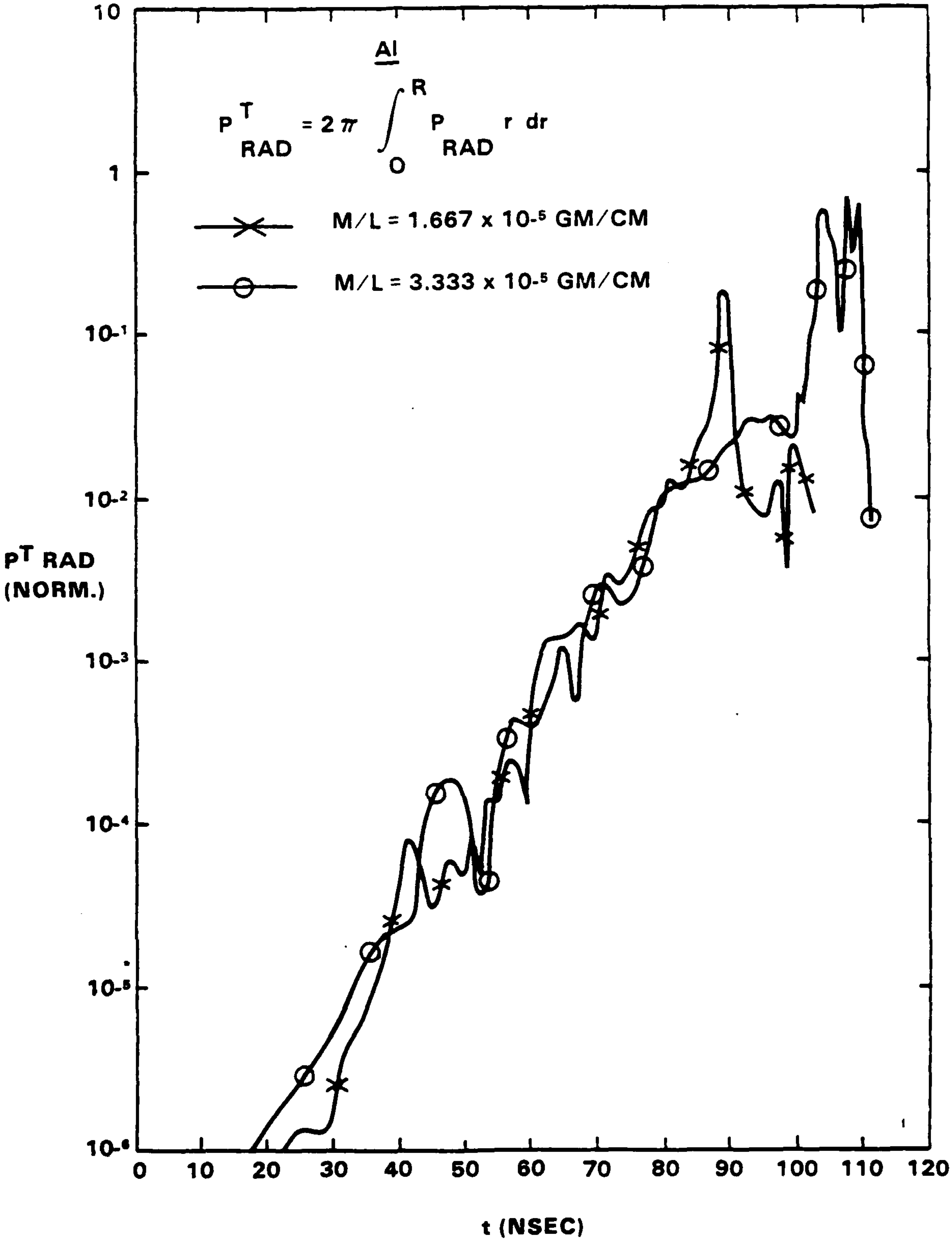

Al
$P^{T}_{RAD} = 2\pi \int_{O}^{R} P_{RAD}\, r\, dr$
M/L = 1.667 x 10-5 GM/CM
M/L = 3.333 x 10-5 GM/CM
10
1
10-1
10-2
10-3
10-4
10-5
10-6
PT RAD
(NORM.)
0
10
20
30
40
50
60
70
80
90
100
110
120
t (NSEC)

Figure 29

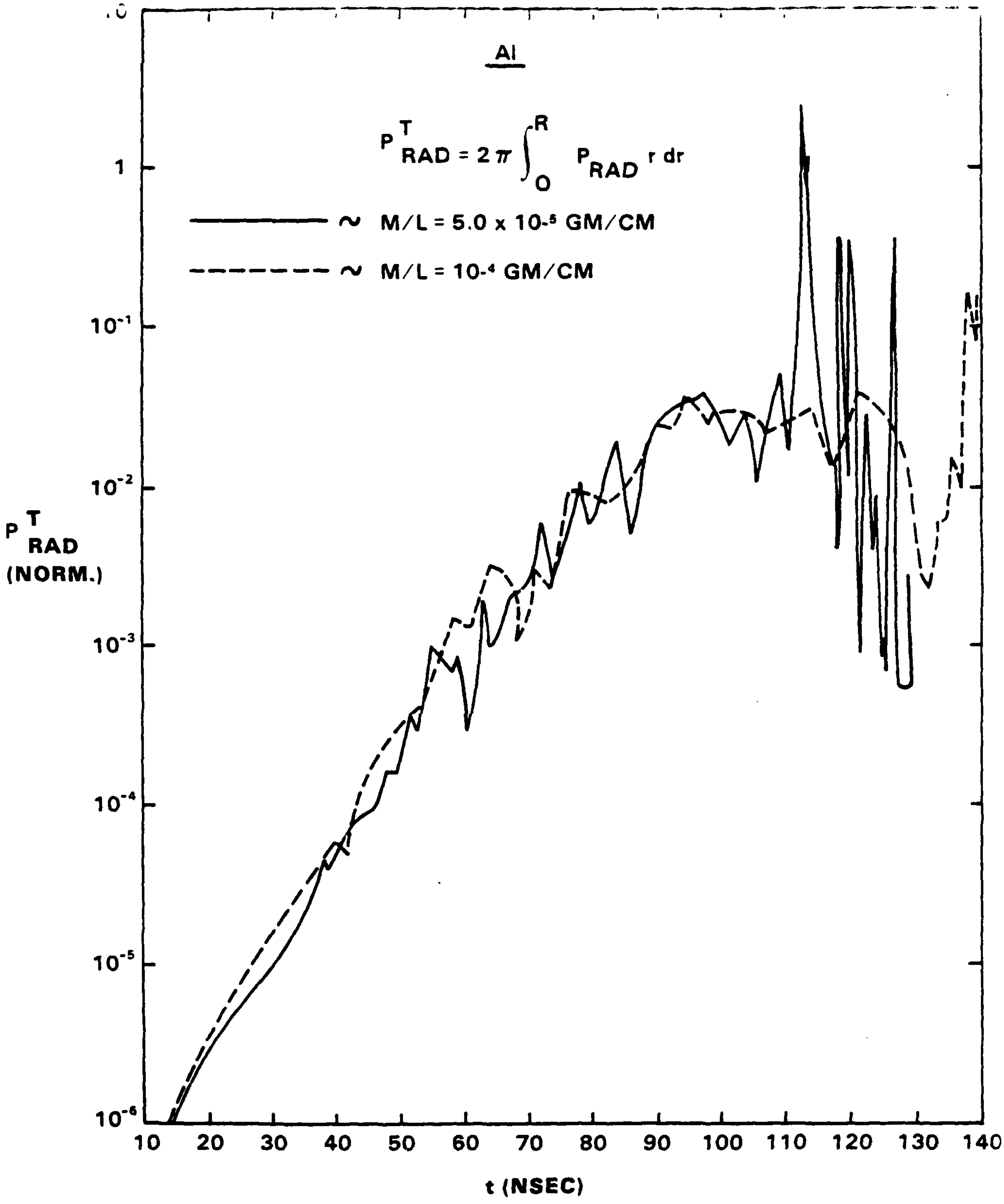

Al
$P^T_{RAD} = 2\pi \int_0^R P_{RAD}\, r\, dr$
~ M/L = 5.0 x 10-5 GM/CM
~ M/L = 10-4 GM/CM
P^T_{RAD} (NORM.)
.0
1
10-1
10-2
10-3
10-4
10-5
10-6
10
20
30
40
50
60
70
80
90
100
110
120
130
140
t (NSEC)

Figure 30

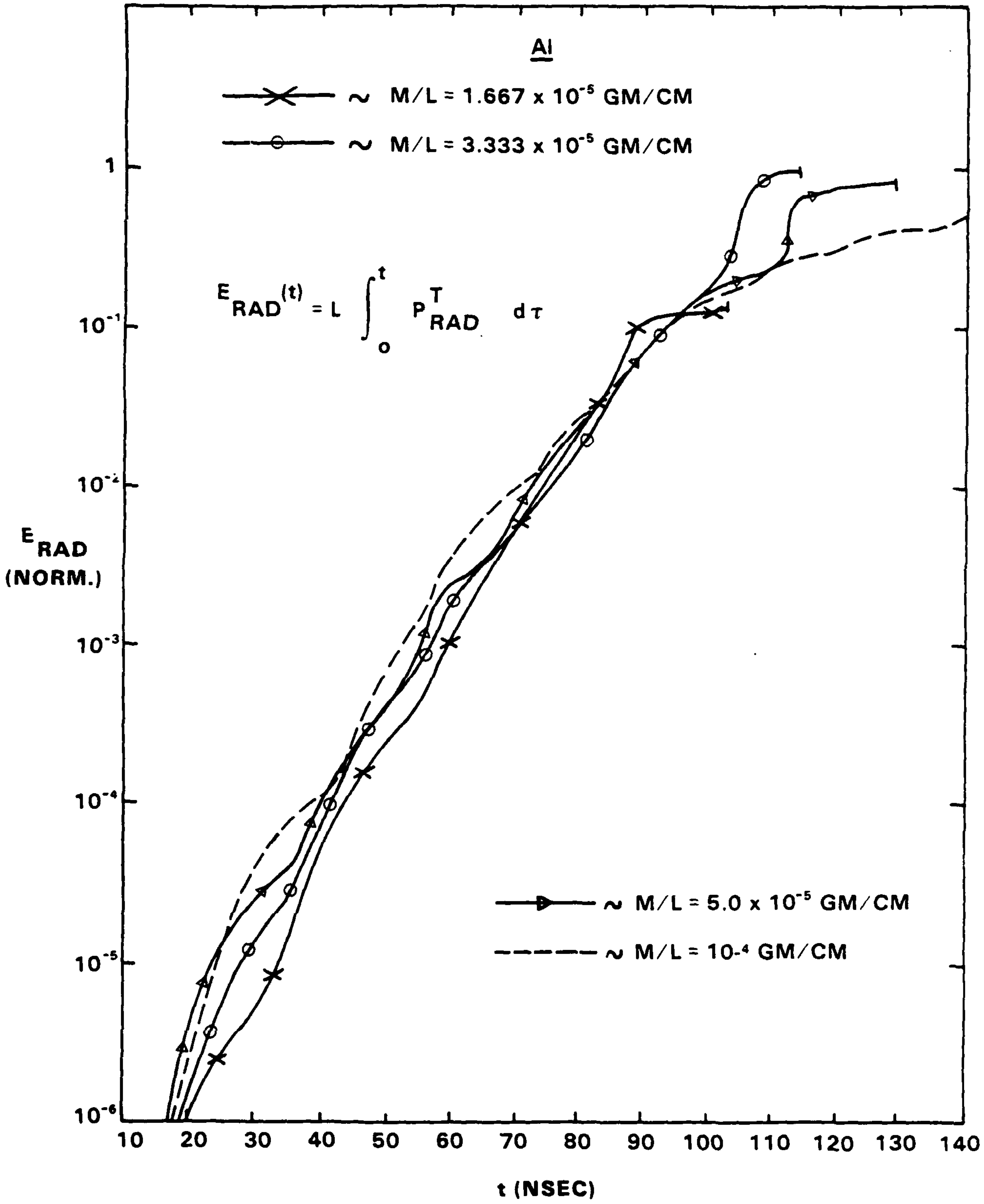
Al
~ M/L = 1.667 x 10⁻⁵ GM/CM
~ M/L = 3.333 x 10⁻⁵ GM/CM
$E_{RAD}(t) = L \int_o^t P_{RAD}^T \, d\tau$
~ M/L = 5.0 x 10⁻⁵ GM/CM
~ M/L = 10-⁴ GM/CM
E RAD (NORM.)
1
10⁻¹
10⁻²
10⁻³
10⁻⁴
10⁻⁵
10⁻⁶
10
20
30
40
50
60
70
80
90
100
110
120
130
140
t (NSEC)

Figure 51

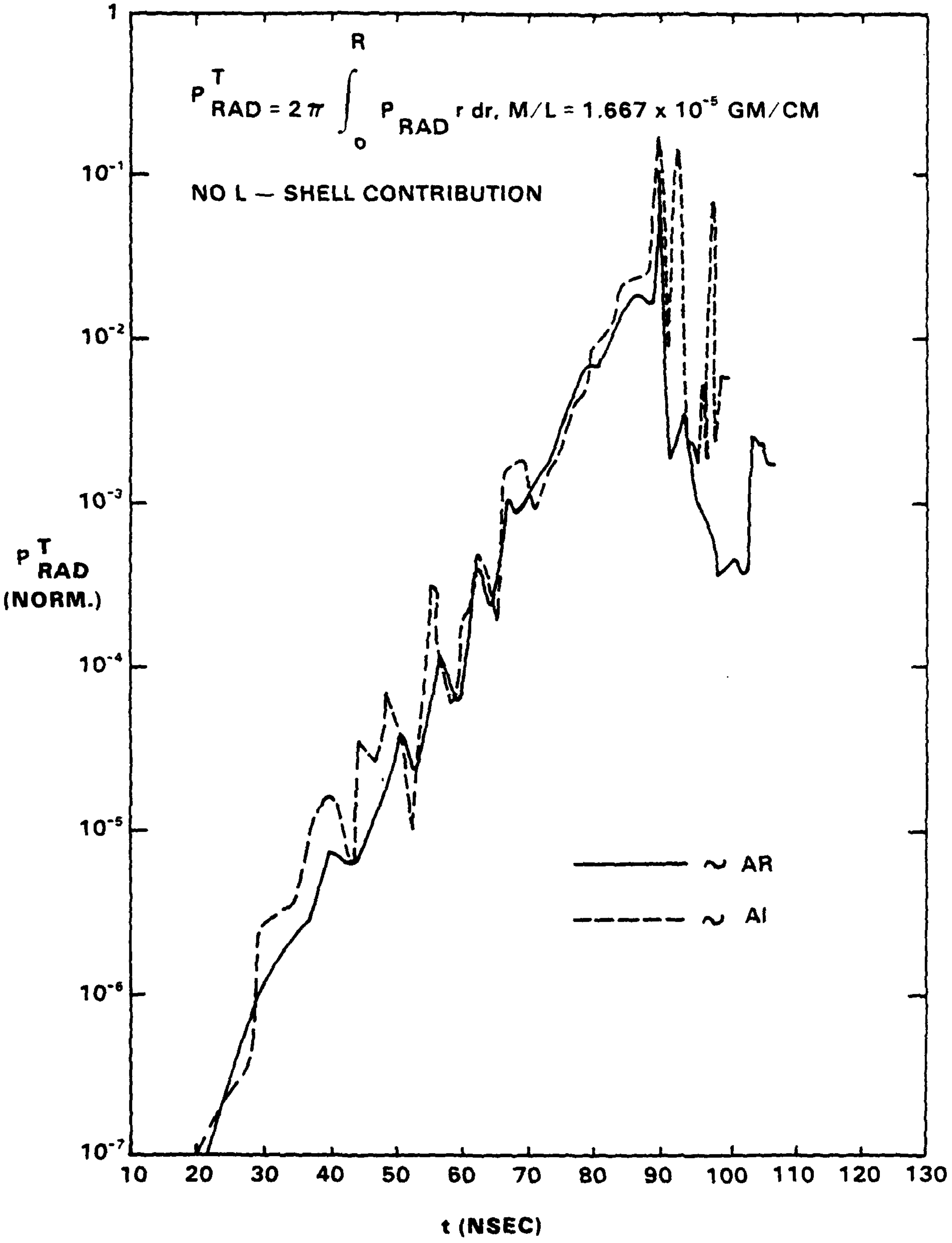

$P^T_{RAD} = 2\pi \int_0^R P_{RAD}\, r\, dr$, M/L = 1.667 x 10^{-5} GM/CM
NO L — SHELL CONTRIBUTION
P^T_{RAD} (NORM.)
1
10^{-1}
10^{-2}
10^{-3}
10^{-4}
10^{-5}
10^{-6}
10^{-7}
10
20
30
40
50
60
70
80
90
100
110
120
130
t (NSEC)
~ AR
~ Al

Figure 32

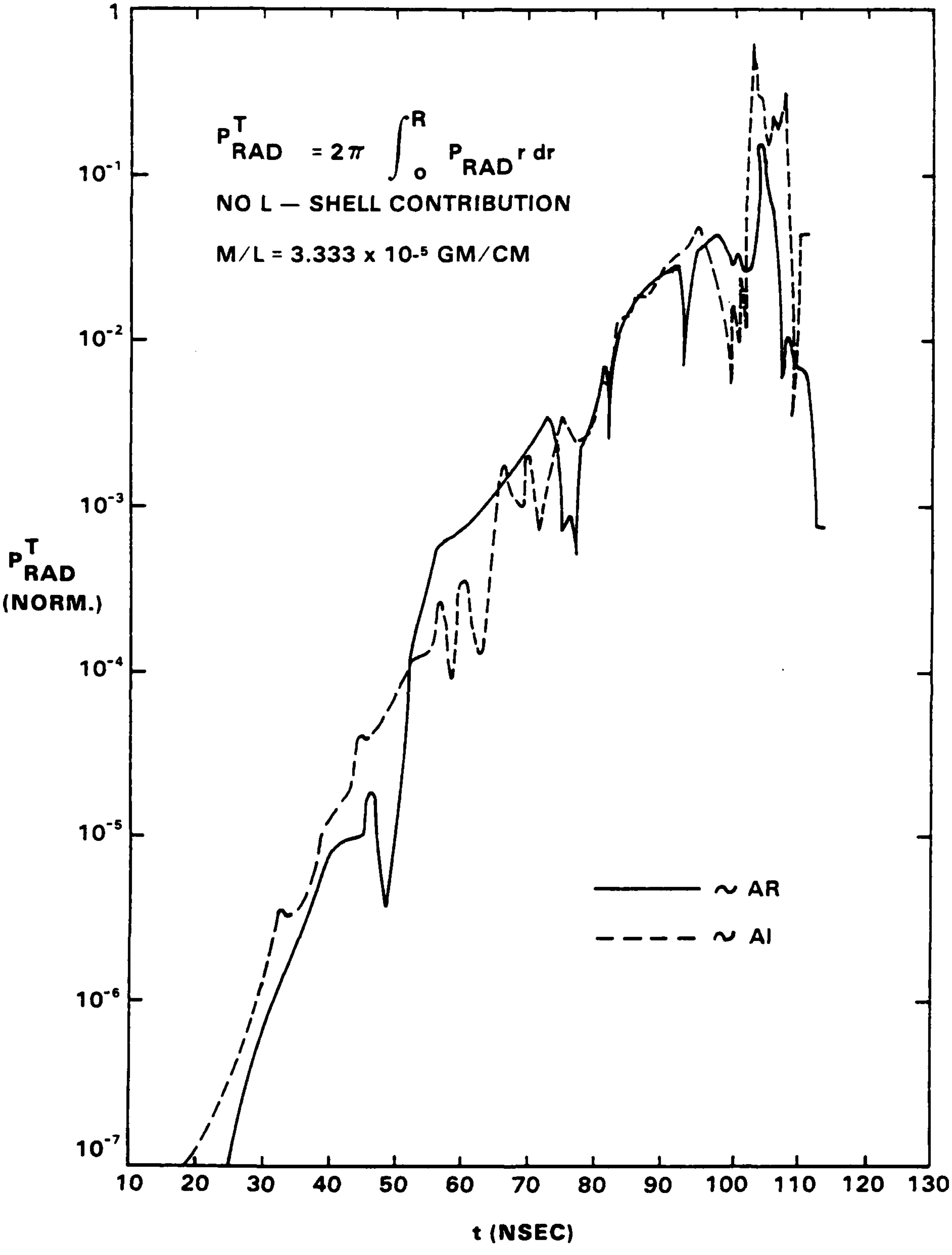
$P^T_{RAD} = 2\pi \int_o^R P_{RAD}\, r\, dr$
NO L — SHELL CONTRIBUTION
M/L = 3.333 x 10-5 GM/CM
1
10^{-1}
10^{-2}
10^{-3}
10^{-4}
10^{-5}
10^{-6}
10^{-7}
P^T_{RAD} (NORM.)
10
20
30
40
50
60
70
80
90
100
110
120
130
t (NSEC)
~ AR
~ Al

Figure 33

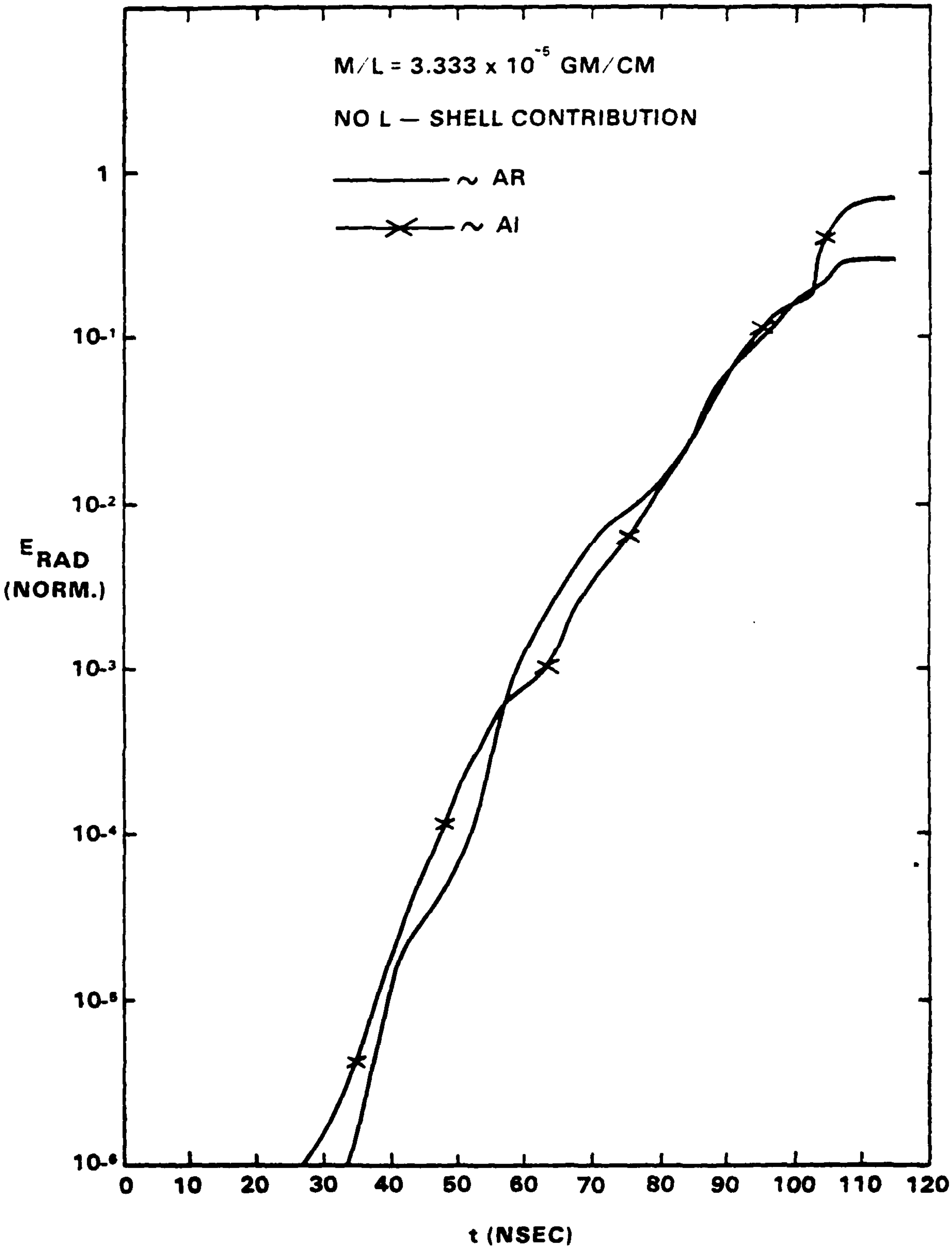

M/L = 3.333 x 10⁻⁵ GM/CM
NO L — SHELL CONTRIBUTION
~ AR
~ Al
E RAD (NORM.)
1
10-1
10-2
10-3
10-4
10-5
10-6
0
10
20
30
40
50
60
70
80
90
100
110
120
t (NSEC)

Figure 34

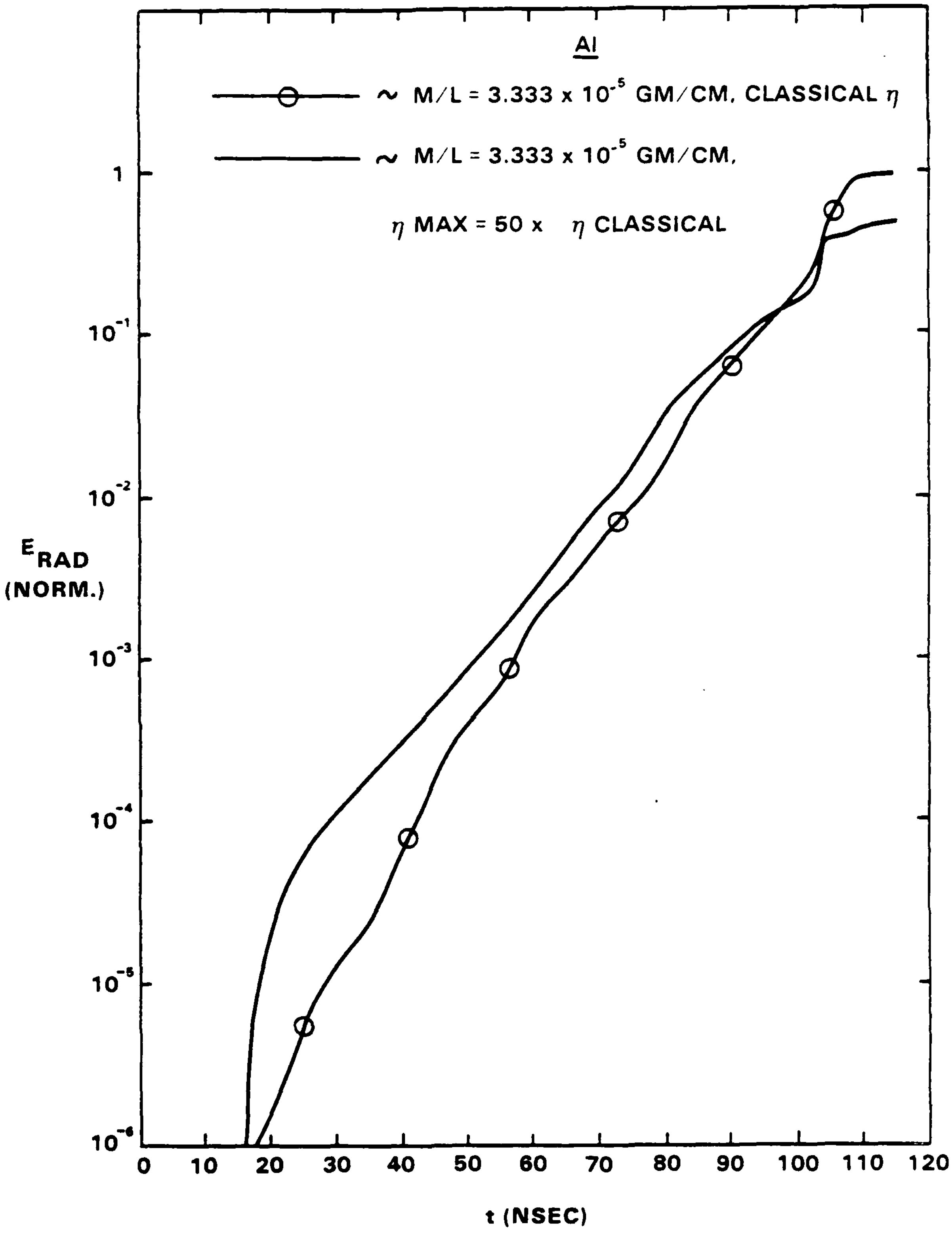
Al
~ M/L = 3.333 x 10⁻⁵ GM/CM, CLASSICAL η
~ M/L = 3.333 x 10⁻⁵ GM/CM,
η MAX = 50 x η CLASSICAL
E_RAD (NORM.)
1
10⁻¹
10⁻²
10⁻³
10⁻⁴
10⁻⁵
10⁻⁶
0
10
20
30
40
50
60
70
80
90
100
110
120
t (NSEC)

Figure 55

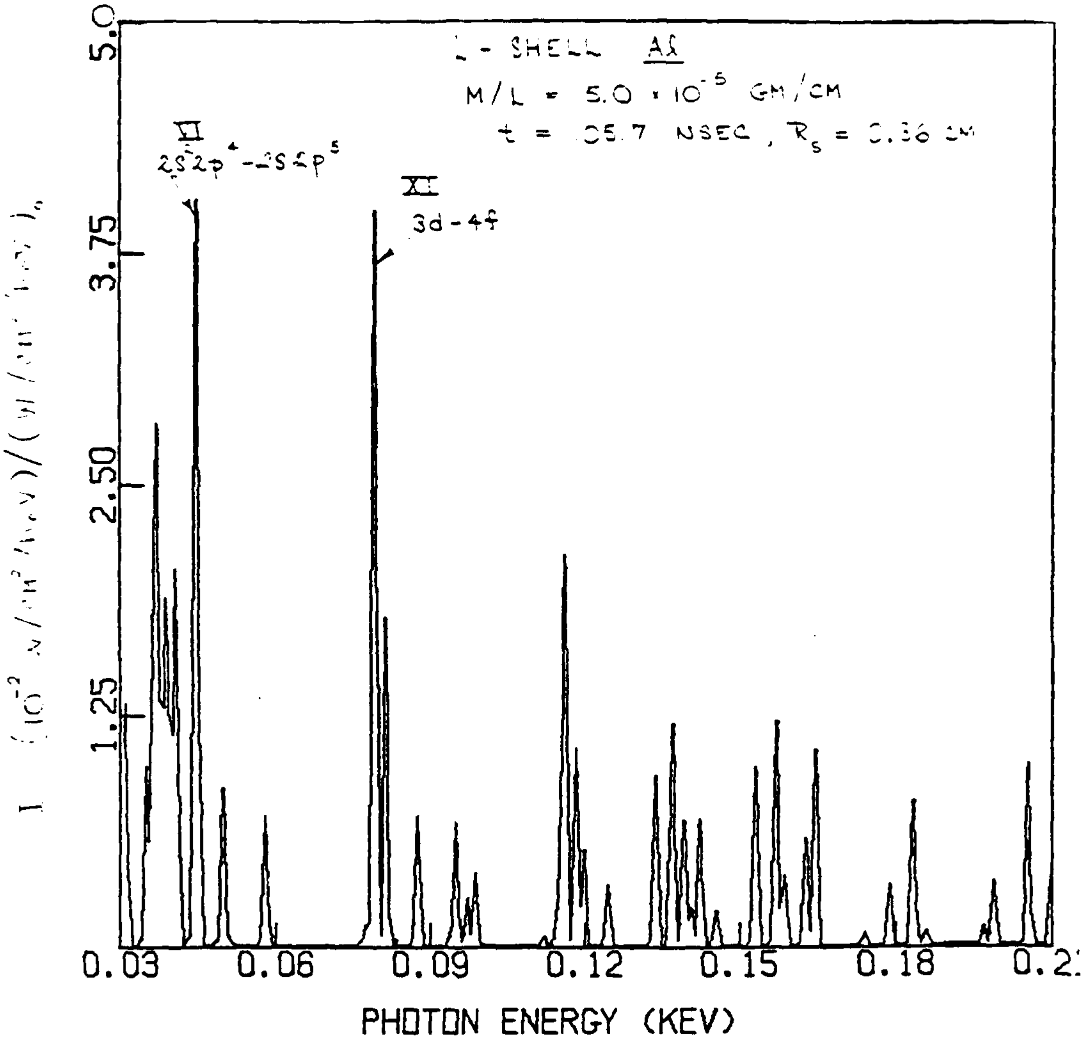
L - SHELL Al
M/L = 5.0 × 10^{-5} GM/CM
t = 05.7 NSEC, R_s = 0.36 CM
VI
$2s^2 2p^4 - 2s 2p^5$
XI
3d - 4f
I (10^{-2} W/CM^2 KEV)/(W/CM^2 KEV)$_0$
5.0
3.75
2.50
1.25
0.03
0.06
0.09
0.12
0.15
0.18
0.21
PHOTON ENERGY (KEV)

Figure 36

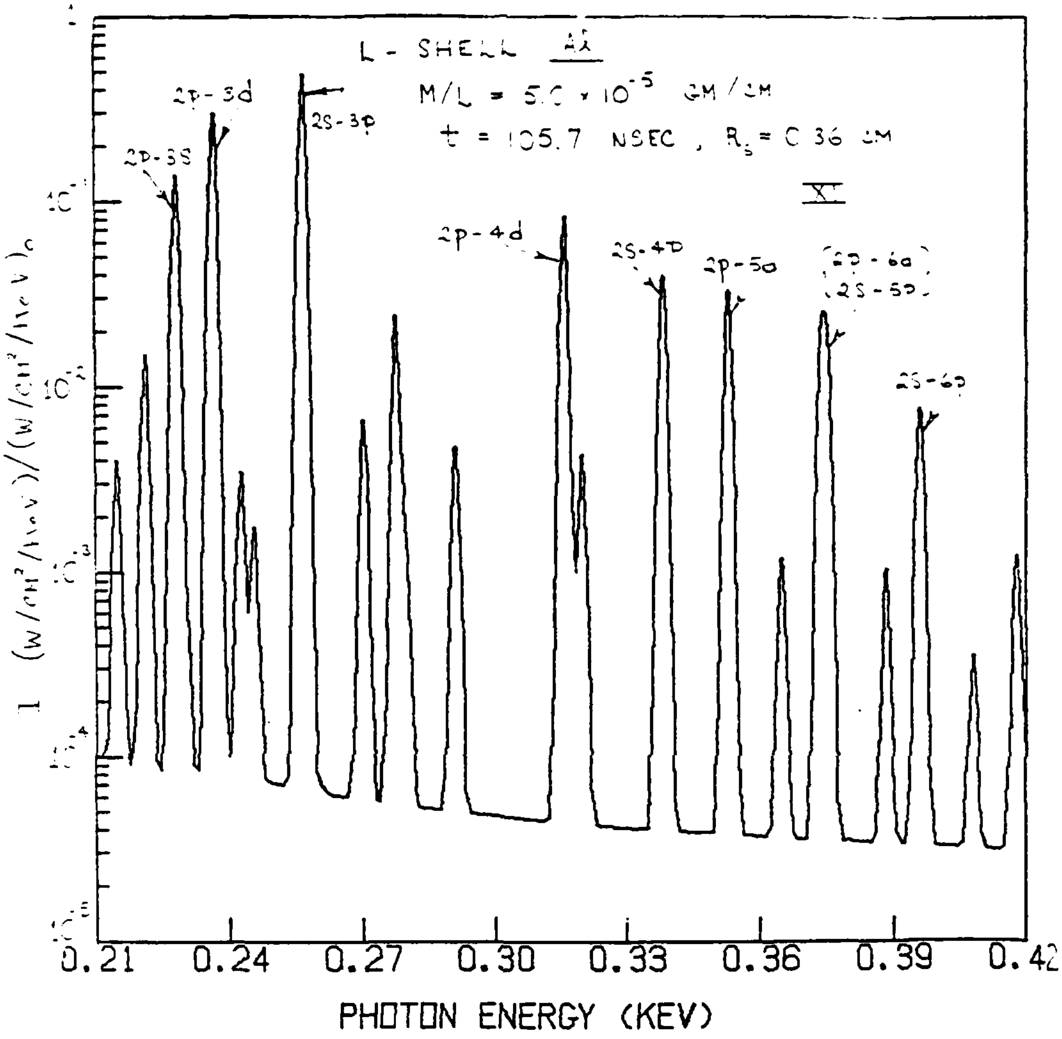
L - SHELL Al
$M/L = 5.0 \times 10^{-5}$ GM/CM
t = 105.7 NSEC , R_s = 0.36 CM
XI
2p-3s
2p-3d
2s-3p
2p-4d
2s-4p
2p-5d
(2p-6d)
(2s-5p)
2s-6p
10^{-1}
10^{-2}
10^{-3}
10^{-4}
10^{-5}
I (W/cm²/keV)/(W/cm²/keV)$_c$
0.21
0.24
0.27
0.30
0.33
0.36
0.39
0.42
PHOTON ENERGY (KEV)

Figure 57

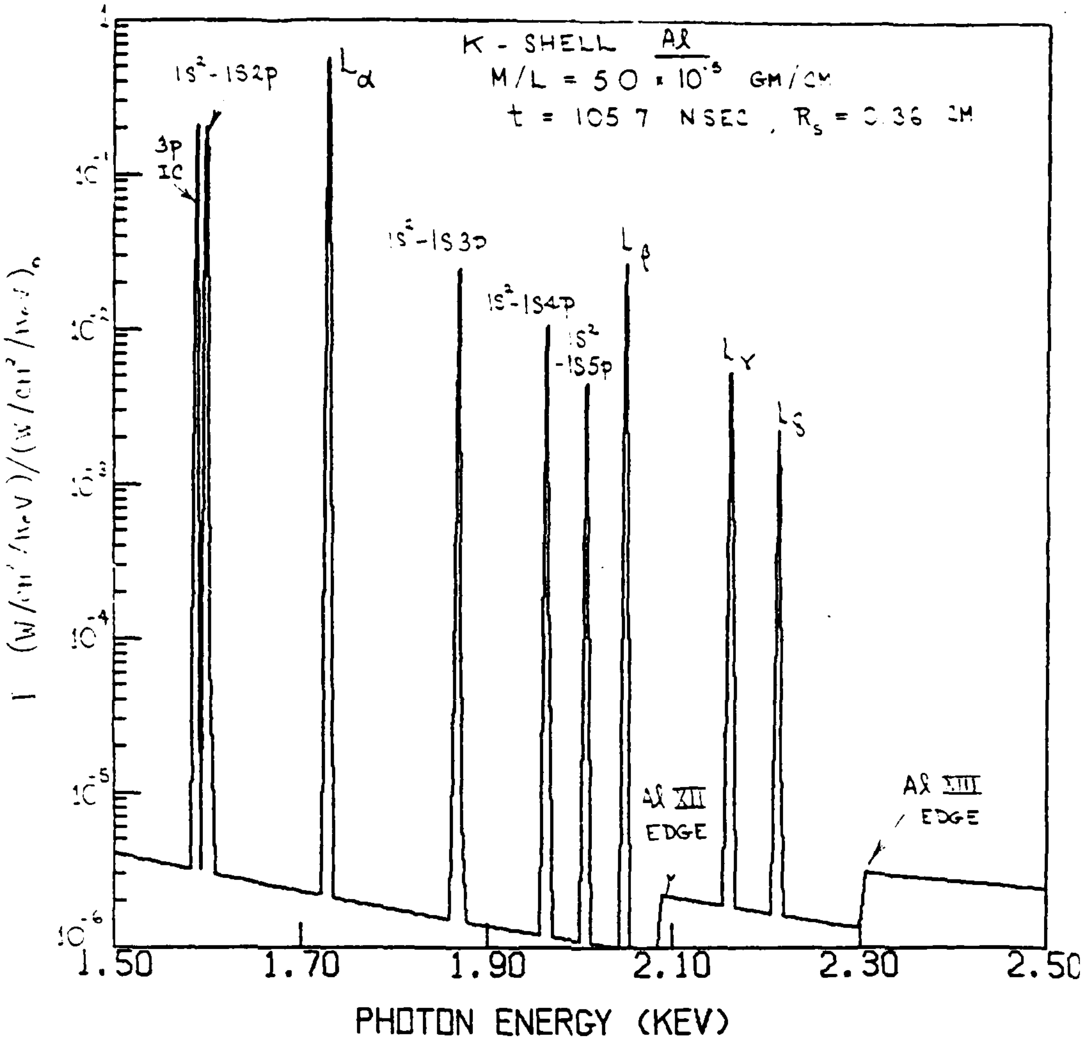
K - SHELL Al
M/L = 5.0 × 10^-5 GM/CM
t = 105.7 NSEC, R_s = 0.36 CM
1s^2-1s2p
3p IC
L_α
1s^2-1s3p
1s^2-1s4p
1s^2-1s5p
L_β
L_γ
L_δ
Al XII EDGE
Al XIII EDGE
I (W/cm^2/keV)/(W/cm^2/keV)_c
1
10^-1
10^-2
10^-3
10^-4
10^-5
10^-6
1.50
1.70
1.90
2.10
2.30
2.50
PHOTON ENERGY (KEV)

Figure 38

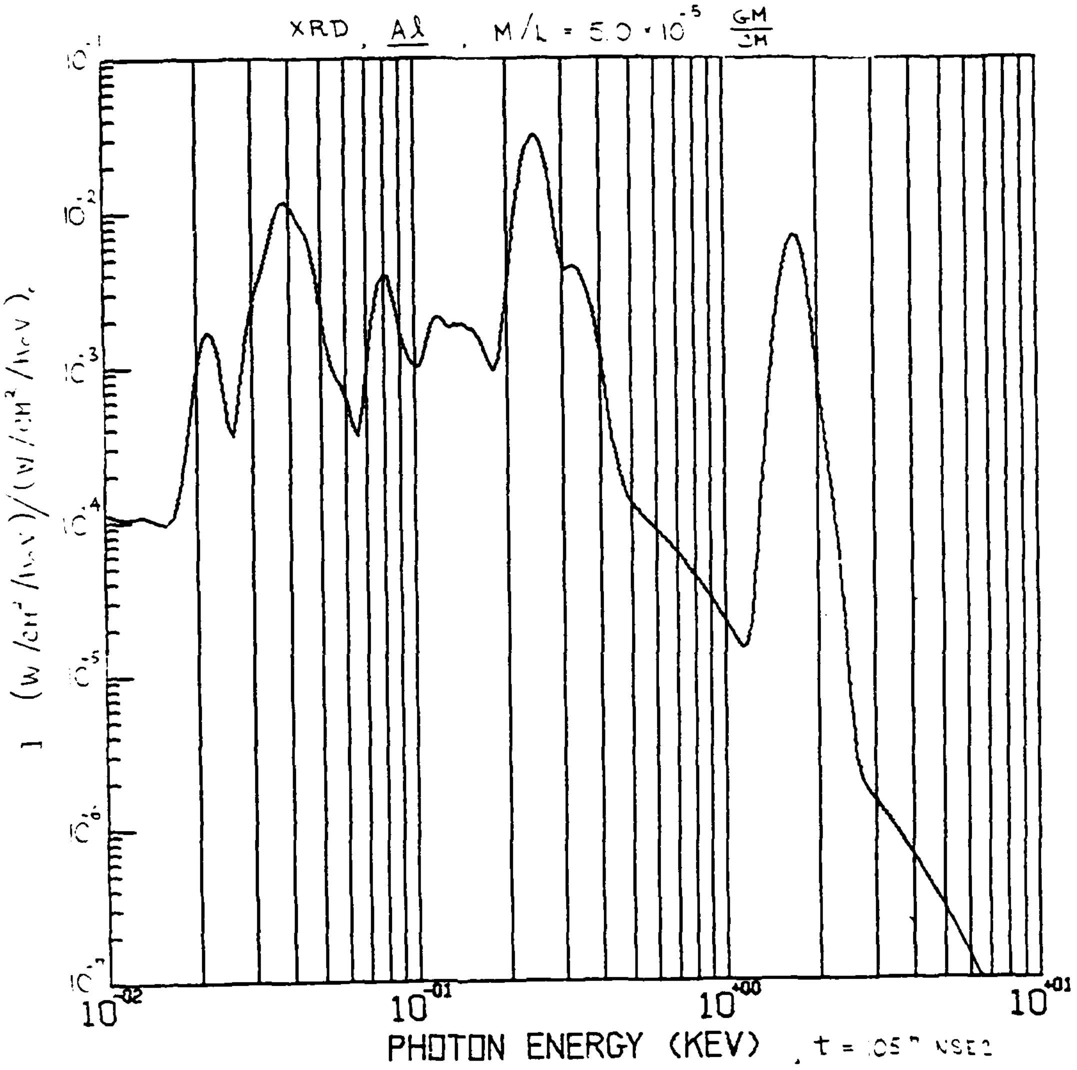
XRD , Aℓ , M/L = 5.0 × 10^-5 GM/CM
I (W/CM²/KEV)/(W/CM²/KEV)
10^-1
10^-2
10^-3
10^-4
10^-5
10^-6
10^-7
10^-02
10^-01
10^+00
10^+01
PHOTON ENERGY (KEV)
t = .05 NSEC

Figure 39

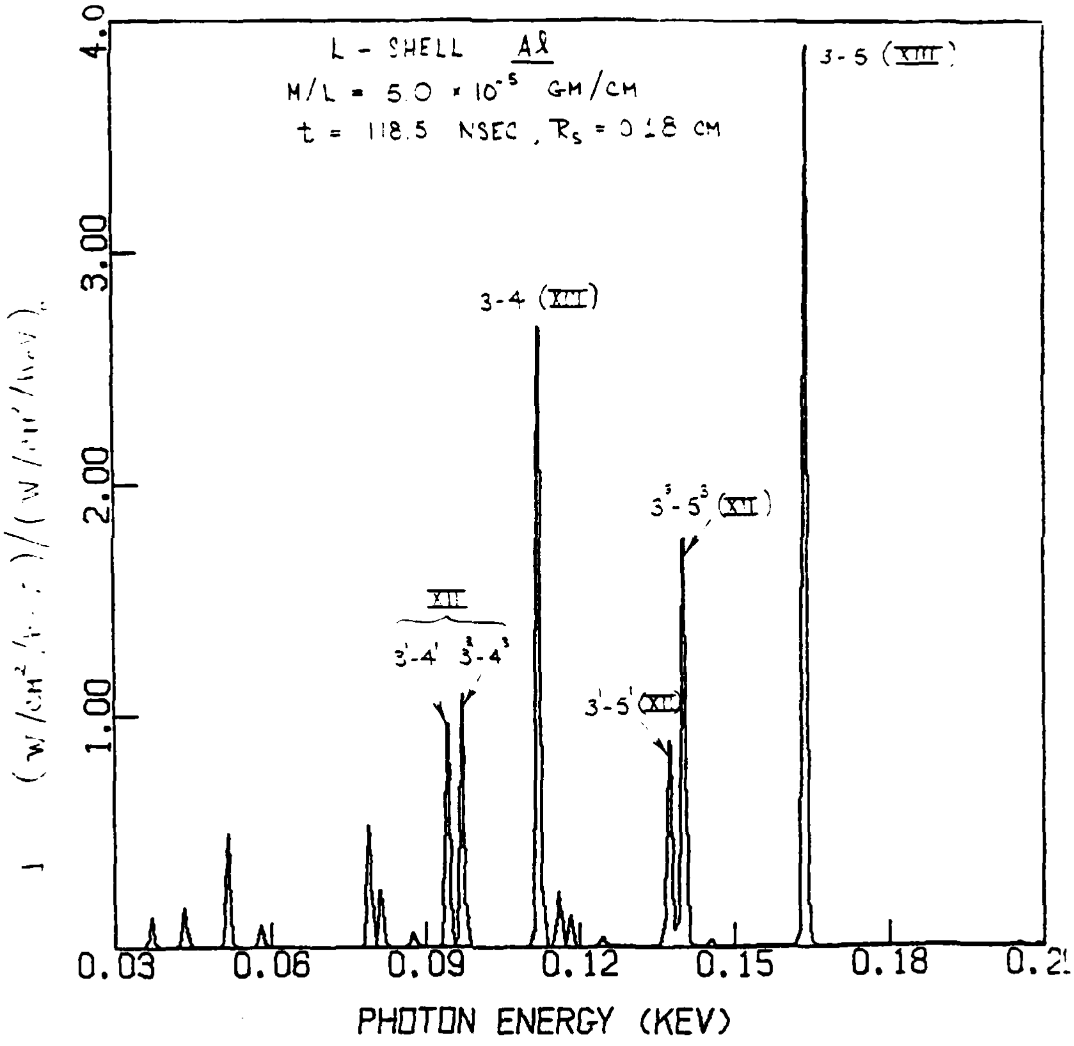
L - SHELL Aℓ
M/L = 5.0 × 10^{-5} GM/CM
t = 118.5 NSEC , R_s = 0.18 CM
3-5 (XIII)
3-4 (XIII)
3^3-5^3 (XII)
3^1-5^1 (XII)
XII
3^1-4^1 3^3-4^3
4.0
3.00
2.00
1.00
0.03
0.06
0.09
0.12
0.15
0.18
0.2
PHOTON ENERGY (KEV)

Figure 40

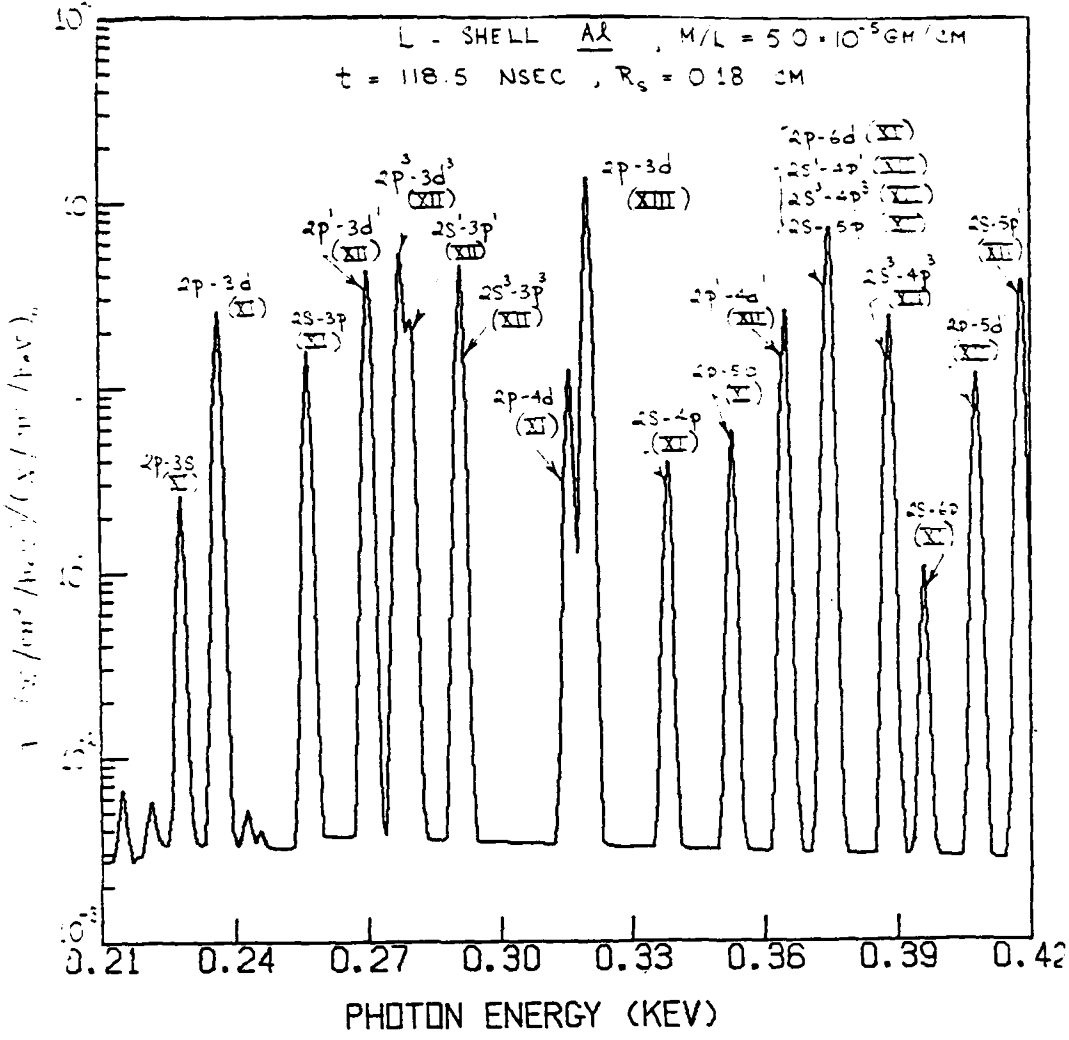
L - SHELL Aℓ , M/L = 5.0 · 10⁻⁵ GM/CM
t = 118.5 NSEC , Rs = 0.18 CM
2p-3s (X)
2p-3d (X)
2s-3p (X)
2p¹-3d¹ (XII)
2p³-3d³ (XII)
2s¹-3p¹ (XII)
2s³-3p³ (XII)
2p-4d (X)
2p-3d (XIII)
2s-4p (XI)
2p-5d (X)
2p¹-4d¹ (XII)
2p-6d (X)
2s¹-4p¹ (XI)
2s³-4p³ (XI)
2s-5p (X)
2s³-4p³ (XI)
2s-6p (X)
2p-5d (X)
2s-5p¹ (XI)
10²
10
1
10⁻¹
10⁻²
10⁻³
0.21
0.24
0.27
0.30
0.33
0.36
0.39
0.42
PHOTON ENERGY (KEV)

Figure 41

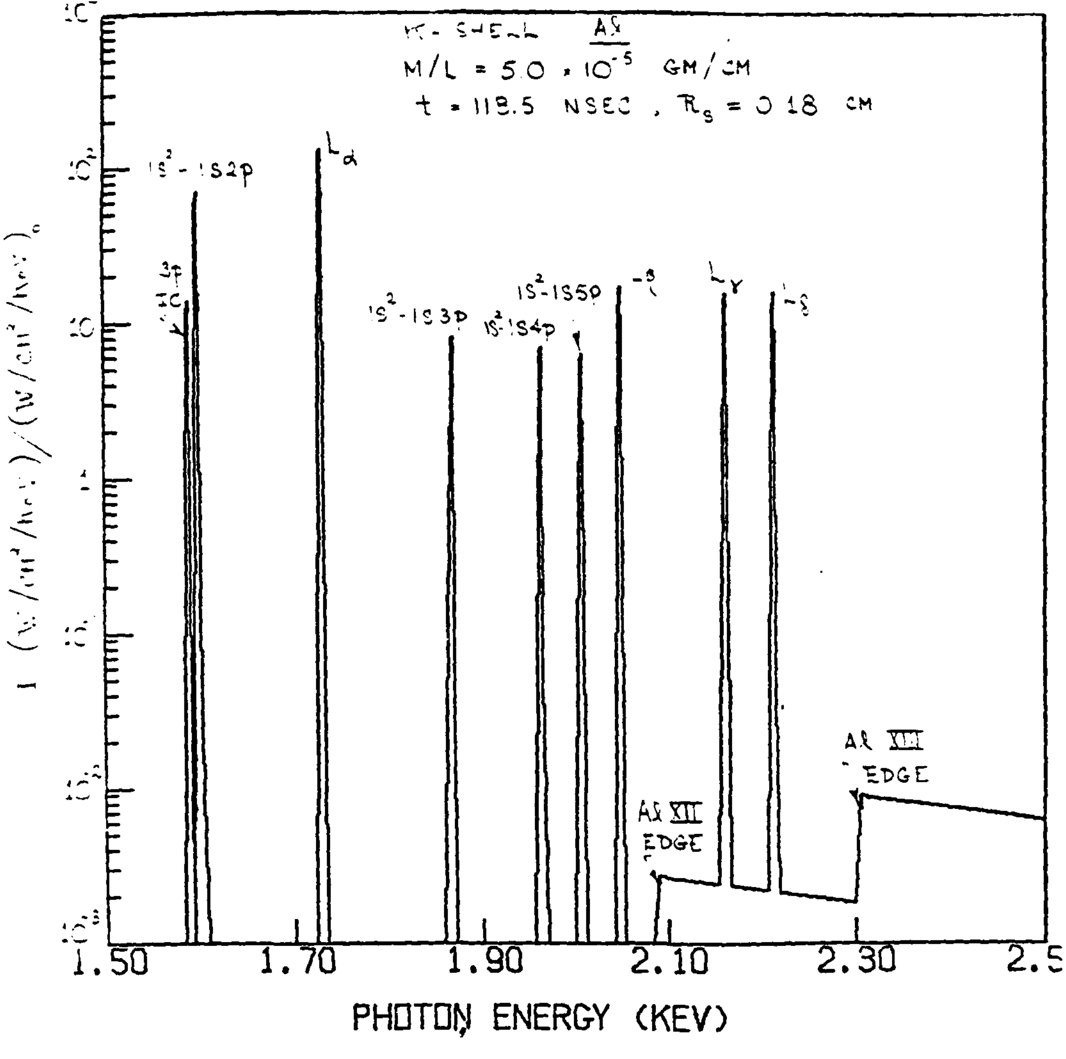
K-SHELL Al
M/L = 5.0 × 10⁻⁵ GM/CM
t = 118.5 NSEC , R_s = 0.18 CM
1s²-1s2p
Lα
3P
IC
1s²-1s3p
1s²-1s4p
1s²-1s5p
Lβ
Lγ
Lδ
Al XII EDGE
Al XIII EDGE
10³
10²
10
1
10⁻¹
10⁻²
10⁻³
I (W/cm²/keV)/(W/cm²/keV)₀
1.50
1.70
1.90
2.10
2.30
2.5
PHOTON ENERGY (KEV)

Figure 42

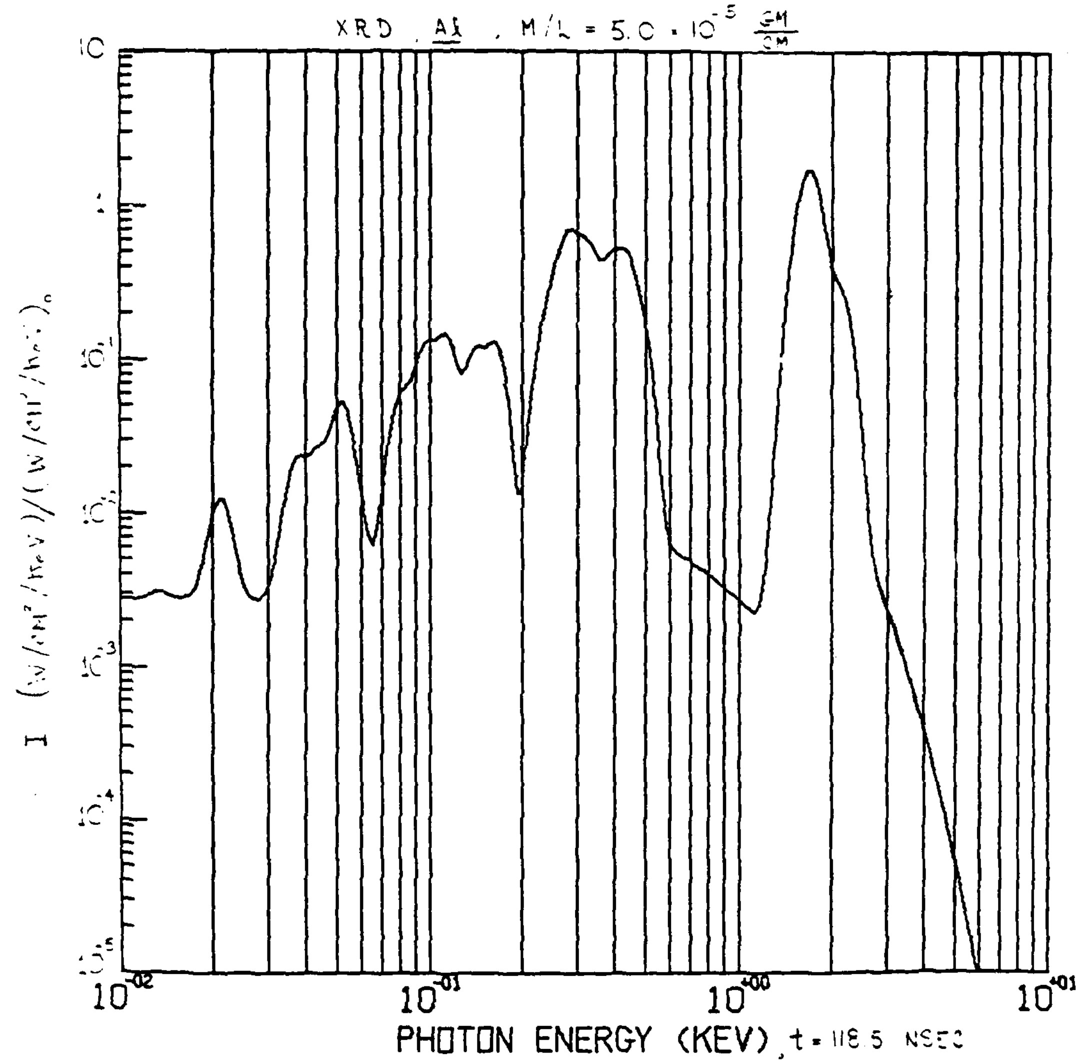
XRD , Al , M/L = 5.0 × 10^-5 GM/CM
10
1
10^-1
10^-2
10^-3
10^-4
10^-5
I (W/cm²/keV)/(W/cm²/keV)₀
10^-02
10^-01
10^+00
10^+01
PHOTON ENERGY (KEV), t = 118.5 NSEC

Figure 43

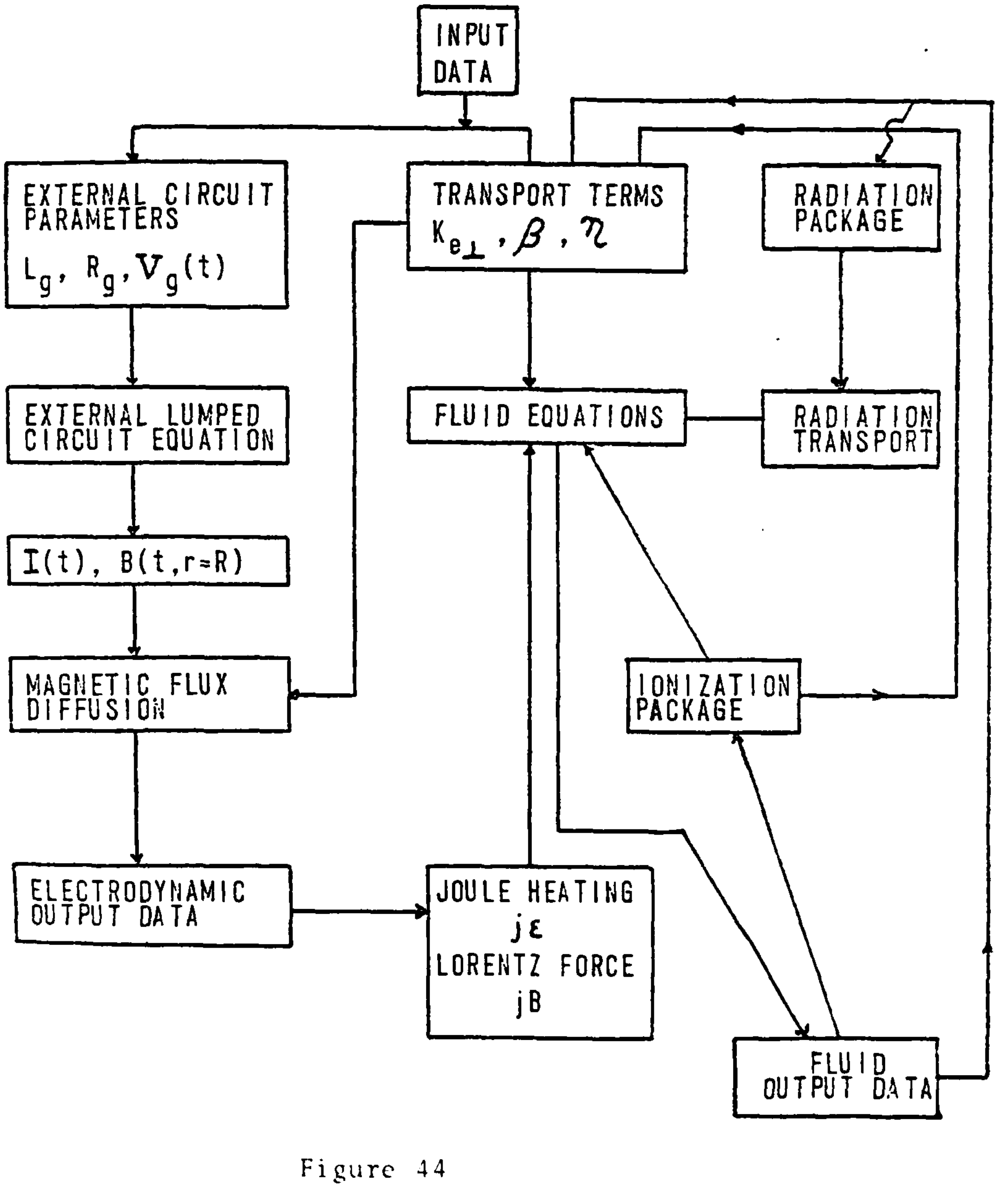
INPUT DATA
EXTERNAL CIRCUIT PARAMETERS
L_g, R_g, $V_g(t)$
TRANSPORT TERMS
$K_{e\perp}$, β, η
RADIATION PACKAGE
EXTERNAL LUMPED CIRCUIT EQUATION
FLUID EQUATIONS
RADIATION TRANSPORT
$I(t)$, $B(t, r=R)$
MAGNETIC FLUX DIFFUSION
IONIZATION PACKAGE
ELECTRODYNAMIC OUTPUT DATA
JOULE HEATING
$j\varepsilon$
LORENTZ FORCE
jB
FLUID OUTPUT DATA

Figure 44

Appendix A

DIRECT SOLUTION OF THE EQUATION OF TRANSFER USING FREQUENCY- AND ANGLE-AVERAGED PHOTON-ESCAPE PROBABILITIES FOR SPHERICAL AND CYLINDRICAL GEOMETRIES

[illegible]
Pergamon Press Ltd

DIRECT SOLUTION OF THE EQUATION OF TRANSFER USING FREQUENCY- AND ANGLE-AVERAGED PHOTON-ESCAPE PROBABILITIES FOR SPHERICAL AND CYLINDRICAL GEOMETRIES

J. P. APRUZESE
Science Applications, Inc., McLean, VA 22102, U.S.A.

(*Received 2 September 1980*)

Abstract—A previously developed technique for solving the transfer equation directly by using frequency- and angle-averaged escape probabilities in a planar, Doppler-broadened medium is generalized to encompass spherical and cylindrical geometries, as well as a Lorentz opacity profile. Two key elements permit this generalization to be made. The first is a reciprocity theorem relating the coupling constant from cell *i* to cell *j* to that from cell *j* to cell *i*. The second is the use of a universal but accurate mean angle of diffusivity

1. INTRODUCTION

In a previous paper,[1] it has been shown that line photon-escape probabilities can be utilized to obtain exact solutions of the transfer equation in a Doppler-broadened, plane-parallel medium. The central quantity needed to apply this technique, the coupling constant C_{ij}, is equal to the probability that a photon emitted in a cell of finite size *i* traverses the distance between cells *i* and *j* and is absorbed in cell *j*. This coupling constant is simply the probability that a photon emitted in cell *i* reaches the closest surface of cell *j* minus the probability that it reaches the rear surface of cell *j*. The simplicity of the plane-parallel geometry allows the frequency-averaged line escape probability $P_e(\tau_0)$ to be readily angle-averaged as

$$\overline{P_e(\tau_0)} = \int_0^1 P_e\left(\frac{\tau_0}{\mu}\right) d\mu. \tag{1}$$

In this paper, the plane-parallel formalism is extended to spherical and cylindrical geometries, where no such simple integral as Eq. (1) applies. In addition, the technique is extended to the case of a Lorentz profile by means of simple, but highly accurate, analytic fits to P_e. The technique developed here may also be extended to the case of a Voigt profile, provided that computationally efficient evaluations of P_e as a function of optical depth and damping constant are available.

2. CALCULATION OF THE COUPLING CONSTANTS IN SPHERICAL OR CYLINDRICAL GEOMETRY

The ease of determining photon coupling constants in planar geometry stems partially from the fact that each cell occupies 2π steradians, as measured from each other cell. In spherical or cylindrical geometry, this relation clearly does not hold and the greatest calculational difficulties are anticipated when computing the coupling constant from an outer to an inner cell, which involves complicated integration over solid angle. Use of the following reciprocity relation for coupling constants overcomes this potential difficulty:

$$C_{ji} = C_{ij}N_i/N_j, \tag{2}$$

where C_{ij} and C_{ji} are the coupling constants defined in the introduction and N_i and N_j are equal to the total number of absorbers (atoms, ions, or molecules) in cells *i* and *j*, respectively. These coupling constants are analagous to the collision probability matrix of neutron transport theory, for which a similar reciprocity relation exists.[2] To prove Eq. (2), we note that

$$C_{ji} = \sum_{m=1}^{N_i} \sum_{k=1}^{N_j} c_{km}/N_j. \tag{3}$$

where c_{km} is the coupling constant between the kth atom in cell j and the mth atom in cell i; here, the "atom" refers also to ions or molecules. Equation (3) states that the total coupling constant from cell j to cell i is the sum of the coupling constants between the individual atoms of the cells, normalized by dividing by the number of atoms in the cell originating the photon. Since the coupling constant between atom k and atom m equals that between atom m and atom k (since the photon path is the same) it follows that

$$C_{ij} = \sum_{k=1}^{N_j} \sum_{m=1}^{N_i} c_{mk}/N_i = \sum_{m=1}^{N_i} \sum_{k=1}^{N_j} c_{km}/N_i; \tag{4}$$

dividing Eq. (3) by Eq. (4) yields Eq. (2). Equation (2) allows computation of the coupling constants connecting inner to outer cells only; the outer-to-inner cell coupling constants are then obtained from the reciprocity relation.

In practice, it has proven possible to obtain quite accurate results by tracing the photon-escape probability over a single mean angle of diffusivity from the inner to the outer cell. In Fig. 1, this process is graphically illustrated for coupling cell 2 to cell 4. The ray along which the P_e are calculated intersects the radius at the mean diffusivity angle $\bar{\theta}$, the value of which is discussed below. Since the escape probabilities must be averaged over the originating cell, the coupling constant is given by

$$C_{24} = \frac{1}{\tau_a}\int_0^{\tau_a} [P_e(\tau_b - \tau) - P_e(\tau_b + \tau_c - \tau)]\, d\tau, \tag{5}$$

where τ_a, τ_b, and τ_c, are optical depths (see Fig. 1) and P_e refers to the photon-escape probability along the chosen mean ray and is not angle-averaged. Simple but quite accurate expressions for the single ray escape probability have been fitted as a function of line center optical depth τ for Doppler and Lorentz profiles. For a Doppler profile, the following expressions are used:

$$P_e(\tau) = 1/(1 + 0.65\tau + 0.29\tau^2), \qquad \tau \leqslant 5.18; \tag{6a}$$

$$P_e(\tau) = \frac{0.546847}{\tau\sqrt{\ln\tau}}, \qquad \tau > 5.18. \tag{6b}$$

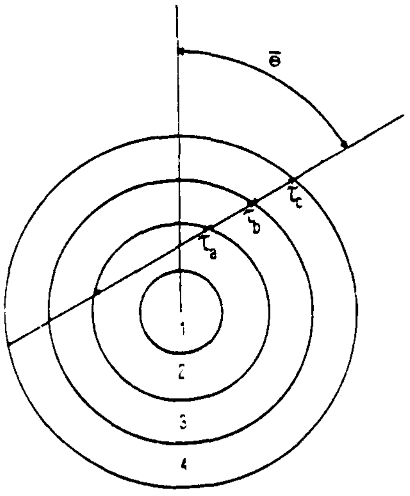

Fig. 1. The method used to obtain coupling constants connecting an inner cell (2) with an outer cell (4) is illustrated for spherical or cylindrical geometries. The quantities τ_a, τ_b, and τ_c are the line-center optical depths along the indicated segments. Escape probabilities are calculated along the ray at a mean angle $\bar{\theta}$ intersecting the radial at the center of the inner cell. The determination of $\bar{\theta}$ is discussed in the text.

Equation (6a) deviates from the exact Doppler profile escape probability in its domain by a maximum of 4% and the maximum deviation of Eq. (6b) is also 4%. Holstein[3] obtained the exact expression corresponding to Eq. (6b) for $\tau \to \infty$, viz.

$$P_e(\tau) = \frac{1}{\tau\sqrt{(\pi \ln \tau)}}, \tag{6c}$$

which differs from Eq. (6b) by just over 3%. Equation (6b) is utilized rather than the infinite-optical-depth limit of Eq. (6c) because it is more accurate at lower optical depths where more photon coupling occurs and it joins smoothly at $\tau = 5.18$ to the polynomial expression given in Eq. (6a).

For a Lorentz profile, the analytic approximations to P_e are also divided into two line-center optical depth domains on each side of $\tau = 5.18$. For $\tau \leqslant 5.18$,

$$P_e(\tau) = 1./(1. + 0.58572\tau) \tag{7a}$$

is adopted whereas, for $\tau > 5.18$, the following expression is used (which is the exact limit as $\tau \to \infty$[3]):

$$P_e(\tau) = 1/\sqrt{(\pi\tau)}. \tag{7b}$$

Equations (7a) and (7b) differ from the exact escape probability by a maximum of 8%: in both cases, the maximum discrepancy occurs in the vicinity of $\tau = 5.18$. For $\tau < 3.4$ and $\tau > 13$, the accuracy is better than 3%. The two expressions join smoothly at $\tau = 5.18$.

A principal question related to the use of this technique involves the specific angle $\bar{\theta}$ along which the rays should be traced to obtain the best coupling constants. These coupling constants are directly calculated only from the inner cells to outer cells, as discussed above. Any photon emitted from cell i whose radius of curvature is much less than that of cell j will travel nearly along the local radius when it reaches the vicinity of the outer cell j. Therefore, the value of C_{ij} obtained is quite insensitive to the choice of $\bar{\theta}$ *when cell* i *is located close to the origin relative to cell* j. If the angle $\bar{\theta}$ is chosen to provide high accuracy when cells i and j have nearly the same radius of curvature (i.e., in the planar limit), the scheme represented in Fig. 1 will automatically scale the C_{ij} correctly as cell i draws closer to $r = 0$. Therefore, $\bar{\theta}$ will be chosen to give accurate results for the planar limit, viz.

$$P_e\left(\frac{\tau}{\cos\bar{\theta}}\right) \cong \int_0^1 P_e\left(\frac{\tau}{\mu}\right) \mathrm{d}\mu. \tag{8}$$

Since, according to Eqs. (6) and (7), $P_e(\tau)$ depends on the line profile, the best value of $\bar{\theta}$ will also be profile-dependent. In this paper, the analysis will be confined to the cases of astrophysical and low-to-medium density laboratory plasmas whose line cores are dominated by Doppler broadening and whose line wings are Lorentzian. Surprisingly, the $\bar{\theta}$ which are chosen according to these considerations also give excellent results for a pure Lorentz line (see below).

The value of $\bar{\theta}$ which gives exact results for large optical depth is readily obtainable from Eqs. (6c), (7b), and (8). For a Doppler profile, letting $\bar{\mu} = \cos\bar{\theta}$ where $\ln\tau \gg \ln\mu$.

$$\begin{aligned}\frac{\bar{\mu}}{\tau\sqrt{[\pi\ln(\tau/\bar{\mu})]}} &= \int_0^1 \frac{\mu\,\mathrm{d}\mu}{\tau\sqrt{[\pi\ln(\tau/\mu)]}}\\ &\doteq \frac{1}{\tau\sqrt{(\pi\ln\tau)}}\int_0^1 \mu\,\mathrm{d}\mu = \frac{1}{2\tau\sqrt{(\pi\ln\tau)}} \Rightarrow \bar{\mu} = \frac{1}{2}.\end{aligned} \tag{9}$$

For a Lorentz profile, we must have

$$\sqrt{\left(\frac{\bar{\mu}}{\pi\tau}\right)} = \int_0^1 \sqrt{\left(\frac{\mu}{\pi\tau}\right)}\mathrm{d}\mu \Rightarrow \bar{\mu} = \frac{4}{9}. \tag{10}$$

The errors in the angle-averaged escape probability at large τ associated with a choice of $\bar{\mu} = \cos\bar{\theta}$ are, therefore, for Doppler and Lorentz profiles

$$\frac{\Delta P_e}{P_e}(\text{Doppler}) = 2\bar{\mu} - 1 \tag{11a}$$

and

$$\frac{\Delta P_e}{P_e}(\text{Lorentz}) = \frac{3}{2}\sqrt{(\bar{\mu})} - 1, \tag{11b}$$

respectively. Thus, choice of a $\bar{\mu}$ which is not exact at large τ leads to a constant error and not a constantly increasing error in P_e. Since the photoexcitation of line radiation is generally dominated by absorption of photons in the high-opacity Doppler core which are generally emitted within a few optical depths, the condition of high accuracy at large τ cannot be the sole criterion for the choice of $\bar{\mu}$. To guide this choice, errors in the Doppler P_e associated with use of various $\bar{\mu}$ have been calculated numerically for more modest optical depths. It is found that, for $1.5 \leq \tau < \infty$, $\bar{\mu}$ somewhat larger than 0.5 is required for exact agreement; a maximum $\bar{\mu}$ of 0.54 is required at $\tau = 3.4$. For $\tau < 1.5$, $\bar{\mu}$ smaller than 0.5 is required for exact agreement; as $\tau \rightarrow 0$, all $\bar{\mu}$ tend toward the correct $P_e = 1$. In view of these results, the value $\bar{\mu} = 0.51$ has been adopted for the following calculations. This value is accurate to 2% at $\tau = \infty$ and is slightly better than $\mu = 0.50$ for the important coupling region $1.8 \leq \tau \leq 25$. Moreover, even for a pure Lorentz profile, $\bar{\mu} = 0.51$ is accurate to better than 10% for all $\tau > 1$ and, according to Eq. (11b), is accurate to 7% as $\tau \rightarrow \infty$. No claim is made here that $\bar{\mu} = 0.51$ is the best choice under all circumstances. It is, however, a reasonable choice for our applications and yields good agreement with exact solutions of several diverse transfer problems. There is also a self-compensating aspect of the coupling constant technique for solving transfer equations which tends to reduce the sensitivity of the results to the choice of $\bar{\mu}$. The source function in each cell is established by photon coupling from within the cell and from other cells. If, for example, the chosen $\bar{\mu}$ is too large, the escape probabilities from other distant cells to the cell in question will be overestimated, generally leading to an overestimate of the coupling. However, the overestimate of P_e from the local cell partially compensates for this effect by reducing the local coupling which is proportional to $(1 - P_e)$. As is shown in Ref. 1, small errors in the coupling matrix do not result in large source-function errors.

As a precaution and to ensure consistency, the N coupling constants from cell i to other cells j are renormalized, as will now be described. First, the probability of escape from the entire plasma from cell i is calculated along the chosen $\bar{\theta}$. This quantity, P_i, must be equal to $1 - \sum_{j=1}^{N} C_{ij}$. It can be found to be slightly different because of numerical noise; therefore the C_{ij} are multiplied by the factor needed to make this sum over j equal to $(1 - P_i)$.

3. COMPARISON OF RESULTS WITH EXACT SOLUTIONS

The most meaningful test of our formalism is the following: how closely are we able to reproduce exact solutions of basic transfer problems in spherical or cylindrical geometry? The technique of using the coupling constants, once obtained, to solve for the steady-state line source function is described in Ref. 1. Briefly, the equation for the steady-state upper level population of a two-level atom in cell i is written as

$$\frac{dN_{ui}}{dt} = 0 = N_{Li}W_i + \sum_{j=1}^{N} N_{uj}A_{uL}C_{ji} - N_{ui}(A_{uL} + D_i), \tag{12}$$

where N_{ui} and N_{Li} are the upper and lower level populations of cell i, respectively, A_{uL} is the spontaneous transition probability (sec^{-1}), C_{ji} is the coupling constant from cell j to cell i as previously defined, and W_i and D_i are the total collisional population and depopulation rates, respectively, of the upper level in cell i. For the cases studied, the absorption coefficient and hence the C are fixed. A fixed absorption coefficient also allows the lower level populations N_l to be written in terms of the upper level population N_u for a two-level atom since

$$k \propto N_l B_{lu} - N_u B_{ul},$$

where the B are the stimulated absorption and emission probabilities. Solving Eq. (12) for the two-level-atom, thus reduces to an inversion of an $N \times N$ matrix. The requirements imposed on the W, D and A_u stem from the fact that the comparison cases specify the Planck function spatially and also the quenching parameter P_Q which is the ratio of collisional to total decay of the upper state. The W, D and A_u of Eq. (12) are chosen to be compatible with the specified Planck function and quenching parameter. The C are calculable from the fixed absorption coefficient.

The results of comparisons with previously published solutions to basic transfer problems are presented in Figs. 2–4. In Fig. 2, comparison is made with the hollow-sphere calculations of Kunasz and Hummer.[4] The cylindrical calculations of Avery *et al.*[5] are repeated with the present method and the results exhibited in Fig. 3. The comparisons of Fig. 3 are confined to cases where the cylinders are long compared to their widths, since the present techniques apply to infinite cylinders. Finally, since the mean diffusivity angle used in these calculations is most accurate for a Doppler profile, a comparison with pure Lorentz profile solutions obtained by Avrett and Hummer[6] is presented in Fig. 4 to determine the applicability of $\bar{\mu} = 0.51$ to Lorentz and hence to Voigt profiles.

It is self-evident from the three figures that the method yields very good accuracy. The maximum deviation of the calculated source function from that given by accurate solutions is 25% for the cylindrical and spherical cases, with most of the curves lying within 15% of the previously obtained values. For the planar Lorentz profile, the maximum error is 10%. Although exact solutions are clearly not obtained by using this formalism, the accuracy is more than acceptable considering that the technique obviates entirely the need for either frequency- or angle-integration. As might be expected, the largest number of cells required to obtain this accuracy (75) was needed for the stringent test of the Kunasz–Hummer cases, where both the absorption coefficient and the Planck function vary as r^{-2}. The smallest number of cells was

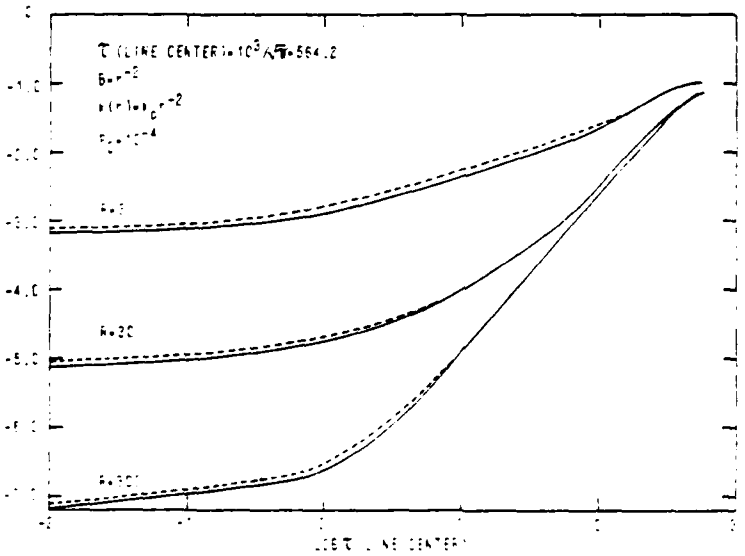

Fig. 2. Steady-state source functions obtained by use of the presently described method (dotted line) are compared with exact spherical solutions obtained in Ref. 4 by Kunasz and Hummer (solid line). In obtaining the present approximate solutions, we used 75 cells logarithmically spaced in τ. The radius of the inner boundary of each hollow sphere is 1 and each curve is labeled by the radius of the outer boundary. The Planck function and absorption coefficient vary as indicated. A pure Doppler profile is assumed with line center optical depth $10^3/\sqrt{\pi} = 564.2$.

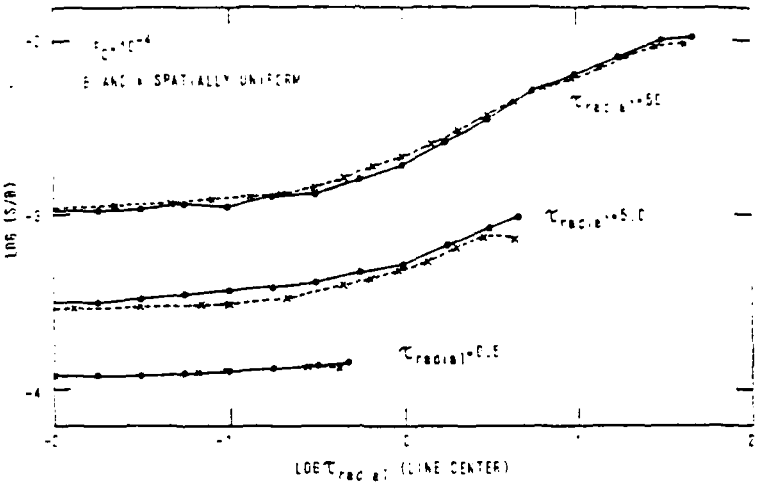

Fig 3. Steady-state source functions obtained by the present method (dotted lines) are compared with the Monte Carlo cylindrical solutions obtained in Ref. 5 (solid lines). The curves are differentiated by line center optical depth along the cylinder radius. In obtaining the present approximate solutions, 20 cells logarithmically spaced in τ were used, with selected cells plotted. The lines connecting the points are intended to guide the eye rather than to suggest interpolated values.

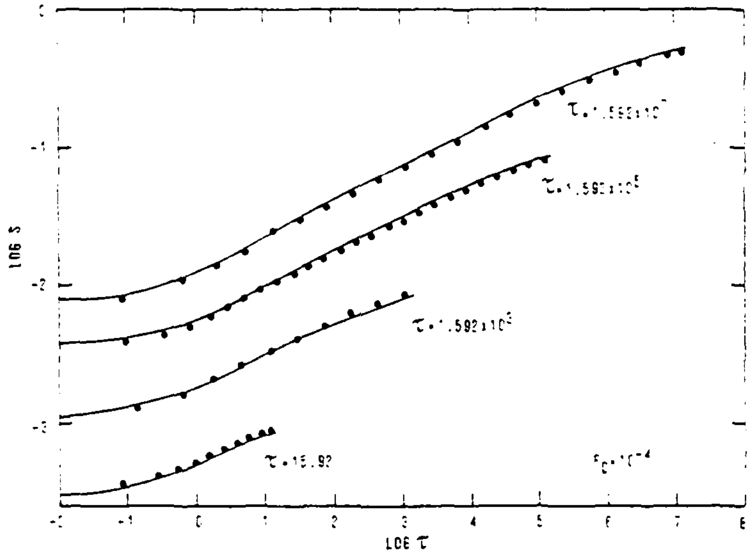

Fig 4. Steady-state source functions obtained by the present method (circles) are compared with the exact planar. Lorentz-profile solutions obtained in Ref. 6 (solid lines). The Planck function is assumed to be spatially uniform and equal to 1. The number of cells (logarithmically spaced in τ) presently used is 10, 10, 25, and 40, in ascending order of optical depth. The value of the source function at the center of each cell is indicated by the circles, except for $\tau = 1.592 \times 10^7$, for which every other cell plus the innermost cell are plotted.

used (10) in calculating the low-optical-depth planar Lorentz cases for which the Planck function was spatially uniform.

4. SUMMARY AND CONCLUSIONS

It has been shown that the use of escape probability techniques to obtain solutions to the radiative transfer equation may be extended from planar to cylindrical and spherical geometries. The formalism for line transfer requires that the line-profile-averaged photon escape probability along a ray be known as a function of optical depth. Convenient analytic fits to these quantities are given for the cases of pure Doppler and pure Lorentz line profiles. The technique presented is quite advantageous numerically in that it eliminates frequency and angle integrations at small cost in accuracy. It is also readily adaptable to different physical situations. For instance, for high-density plasmas for which Stark broadening dominates the line profile, the escape probability formulae given by Weisheit[7] could be readily employed.

Perhaps the main drawback to our approach (and the principal area for further work on this technique) is that profile-averaged escape probabilities are most easily obtained and used for spatially constant line profiles. When density and/or temperature gradients are present in such degree as to affect $P_e(\tau)$ significantly, the accuracy of this approach will deteriorate. Obtaining fits to $P_e(\tau)$ in the presence of such gradients is the only way to restore accuracy.

Acknowledgment—This work was supported by the Naval Research Laboratory.

REFERENCES

1. J. P. Apruzese, J. Davis, D. Duston, and K. G. Whitney, *JQSRT* 23, 479 (1980).
2. I. Carlvik, *Proceedings of the Third International Conference on the Peaceful Uses of Atomic Energy*, Vol. 2, p. 225. International Atomic Energy Agency, Vienna (1965).
3. T. Holstein, *Phys. Rev.* 72, 1212 (1947).
4. P. B. Kunasz and D. G. Hummer, *MNRAS* 166, 16 (1974).
5. L. W. Avery, L. L. House, and A. Skumanich, *JQSRT* 9, 519 (1969).
6. E. H. Avrett and D. G. Hummer, *MNRAS* 130, 295 (1965).
7. J. C. Weisheit, *JQSRT* 22, 585 (1979).

Appendix B

COLLISIONAL-RADIATIVE-EQUILIBRIUM SPECTROSCOPIC DIAGNOSIS OF A COMPRESSED, OPTICALLY THICK NEON PLASMA

PHYSICAL REVIEW A VOLUME 24, NUMBER 2 AUGUST 1981

Collisional-radiative-equilibrium spectroscopic diagnosis of a compressed, optically thick neon plasma

J. P. Apruzese,* P. C. Kepple, K. G. Whitney,† J. Davis, and D. Duston
Plasma Physics Division, Naval Research Laboratory, Washington, D.C. 20375

(Received 9 May 1980; revised manuscript received 9 March 1981)

By self-consistently calculating x-ray spectra from first principles, we have delineated the relationships between the spectrum and the state of compression and heating of a neon plasma in detail. A collisional-radiative model including Stark line profiles is used to determine the highly ionized high-density states of neon. One of our calculated spectra reproduces remarkably well an experimental spectrum obtained from laser implosion by Yaakobi *et al.* and indicates compression conditions significantly different from those obtained assuming the validity of local thermodynamic equilibrium. Implications of our calculations for spectroscopic diagnoses of fusion plasmas are discussed.

I. INTRODUCTION

One of the most widely used techniques to diagnose the properties of transient fusionlike plasmas is to analyze their x-ray emissions. In an example of the use of such methods, Yaakobi *et al.*[1] have measured the K-series emission spectrum from a neon plasma produced by laser implosion of a glass microballoon filled with neon at 8.6 atm pressure. Using a methodology that assumed the ionization conditions of the plasma and that accounted for opacity and Stark broadening of the Lyman-α and Stark broadening of the Lyman-β and Lyman-γ lines, they ascribed a density of 0.26 g cm^{-3} (ion density, 7.8×10^{21} cm^{-3}) to the neon emission region. From the measured line intensity ratios $I(\mathrm{Ly}\beta)$ $I(1s^2\text{-}1s3p)$ and $I(\mathrm{Ly}\alpha)$ $I(\mathrm{Ly}\beta)$, an electron temperature of 300 eV was inferred in the context of an LTE plasma model whose line radiation was assumed to be a Planck function—saturated. In this paper, we show that a theoretically self-consistent, steady-state analysis of all the main features of such spectra can be carried out that is based on a first-principles calculation in which the only free parameters are the average plasma properties of temperature, density, size, and velocity profile. This analysis leads to a set of general principles governing the relationships of high density, optically thick plasma properties to their emitted spectra. As a specific example of the application of such principles, we demonstrate that our calculations reproduce well the neon experimental spectrum discussed above and lead to a diagnosis of significantly lower density and higher temperature. Furthermore, our investigation allows an exposition of how and why a self-consistent physical model reproduces an experimental spectrum, while a simpler but inappropriate model such as LTE may lead to miscalculation and or misinterpretation of the spectrum.

II. PLASMA MODEL

For spectrum calculations we have employed a detailed multistate, multilevel model of ionized neon in the context of collisional-radiative equilibrium and an assumed spherical geometry. Since virtually all of the neon at peak compression consists of lithiumlike or more highly stripped ions, the model includes only the ground states for Ne I–Ne VII. For lithiumlike Ne VIII, the atomic model includes the excited states $1s^2\text{-}2p$, $-3s$, $-3p$, $-3d$, and $-4d$. For heliumlike Ne IX, we have the excited-state manifold $1s2s\,^1S$, $1s2p\,^3P$, $1s2p\,^1P$, and the $n=3$ and $n=4$ singlet states. For Ne X, $n=2$, 3, 4, and 5 as well as $n=1$ are included. All of the lines appearing in the Rochester spectrum (Lyα, β, and γ, Ne IX $1s^2\text{-}1s3p\,^1P$, $1s^2\text{-}1s4p\,^1P$, as well as $1s^2\text{-}1s2p\,^1P$) are calculated by self-consistently solving fully coupled nonlinear radiation transport and rate equations.[2] Most importantly, the calculation also includes the self-consistently computed effects of Doppler, Stark,[3] and mass-motional line broadening. Additionally, the calculated spectra are convolved with 1.5 eV of experimental (Gaussian) broadening.[1] However, in most cases, as pointed out by Yaakobi *et al.*, the experimental broadening has little or no effect due to the large Stark linewidths. The rate equations and the radiative transport equation are also used to solve in detail for the continuum radiation arising from recombination from the bare nucleus to the $n=1$ and 2 states of Ne X, and from Ne X $n=1$ to Ne IX $1s^2\,^1S$ and $1s2p\,^3P$.[2]

With the exception of electron collisional excitation rate coefficients and spontaneous decay rates, the methods of calculating the various rate coefficients used in this study have been described in detail in previous papers,[4,5] and only brief reference will be made to these. Every state is coupled to the next (energetically) highest ground state, by collisional ionization and collisional recombination. Additionally, photoionization and radiative recombination are computed in detail for the states mentioned above. The collisional ionization rates are calculated by Seaton's prescription,[6] and the photoionization cross sections are calculated in the hydrogenic approximation[7] using effective free-bound Gaunt factors.[8] Collisional- and total-radiative recombination rates are then calculated as the detailed balance of these. However, the details of the frequency dependence of the hydrogenic photoionization cross sections are replaced by a simpler exponential profile for the recombination process.[2] In addition, adjacent ground states are coupled by dielectronic recombination[9] found by summing capture rates over a manifold of states above the ionization limit which then decay via cascade to the ground state.

Excited levels of a given ion are coupled to the other excited states in the model and to the ground state by electron collisional excitation and deexcitation, and by spontaneous radiative decay. Collisional couplings include forbidden and spin-flip transitions as well as those which are dipole allowed. For Ne X, the Coulomb-Born approximation[10] was used, while a distorted-wave calculation with exchange[11] was used to calculate the coefficients for Ne VIII and Ne IX. Comparisons of these two methods have been made for several transitions in hydrogenlike Al XIII,[12] and excellent agreement was obtained.

As mentioned above, line photon reabsorption is taken into account by solving the radiation transport equation for six selected resonance lines, five of which appear in the published Rochester spectrum[1] (taken by Yaakobi *et al.*) and are generally used as diagnostics for neon- or argon-filled pellet targets. The present model neglects the effect of radiation reabsorption for lines which couple two excited states, even though such lines are optically thick in some of the cases discussed below. This simplification, however, results in no significant error in these cases, where the density is so high that collisional rates coupling excited states vastly exceed radiative rates and thus dominate the cross coupling of these levels. Unless these lines appear in the spectrum to be analyzed, it is not necessary to perform the radiation transport calculations for them. The same principle does not apply for the resonance lines dominating most spectra, where the reduced collision rates and higher radiative rates result in comparable importance for collisions and radiation, or even radiation dominance in the couplings.

Details of the radiation transport and photocoupling calculations are given elsewhere[2,13] and will not be elaborated here. However, an additional feature—the calculation of the effects of the different Doppler shifts caused by the inhomogeneous velocity profile of a plasma implosion on the emitted line profiles—has been included in the radiation transport algorithm. These effects will be fully discussed in an upcoming paper, but in the particular results of this paper it served us mainly to confirm what had been suspected, that even at implosion velocities of 2×10^{7} cm sec^{-1},[14] the effects are small due to the large Stark widths of the lines at high density. For lower density plasmas the effects can be quite significant but it is of little concern here.

In the analysis detailed below, spectra calculated for steady-state plasma conditions are used to interpret an experimental, time-integrated spectrum. While this approach may at first seem questionable, it was justified for the cases considered here—short-pulse Nd laser drivers—by Yaakobi *et al.*[15] in their letter on argon-filled glass microballoon experiments. They found from extensive hydrodynamical simulations of spherical target compressions that the most energetic emission of hydrogenlike lines occurs during a 10-psec time interval during which the plasma properties change little, spatially or temporally. These theoretical results, coupled with the fact that our analysis obtains striking agreement with experiment, indicate that this assumption can be productively employed under these conditions to interpret the emission properties of plasma cores under spherical compression.

III. COMPRESSION DIAGNOSTICS WITH CALCULATED SPECTRA

It is widely recognized that pellet compression along a low adiabat is most desirable in achieving maximum density prior to thermonuclear ignition. Hence, a major goal of laser-driven pellet compression experiments is to obtain the highest possible implosive drive while minimizing preheat. Knowledge of the degree to which this goal is met experimentally may be obtained from a variety of techniques, and one of the prime tools available is spectroscopy. For this purpose, one must know the sensitivity of the emitted spectrum to the plasma's density and temperature. Figure 1 presents three neon spectra calculated for a spherical plasma in CRE. They illustrate the evolution of the emitted spectrum as the same mass of neon is progressively compressed to higher densities and lower temperatures (i.e., along lower adiabats). The lower the adiabat, the closer to the top of the figure the spectrum appears. Increased density is primarily reflected in the widening of the lines due both to larger intrinsic Stark widths and possible opacity broadening. This effect has been utilized

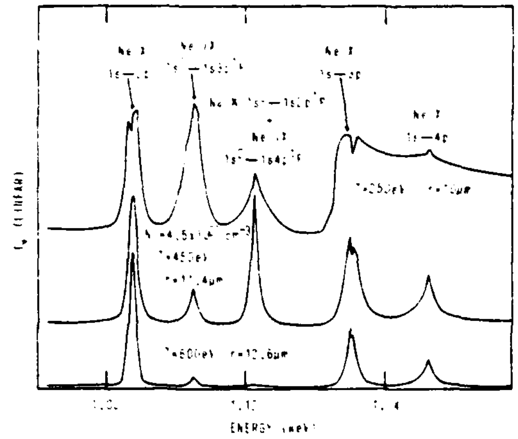

FIG. 1. Three calculated spectra are shown which illustrate, from bottom to top, the changes in spectral signature which occur as a constant neon mass is compressed to higher densities and colder temperatures. The spectra are calculated assuming that the neon plasma is in collisional-radiative equilibrium (CRE). The exterior pellet temperatures decrease from those of the core in accordance with the gradient described in the text. Only the middle spectrum includes the (negligible) pumping effect of the Na X impurity line at 1.13 keV.

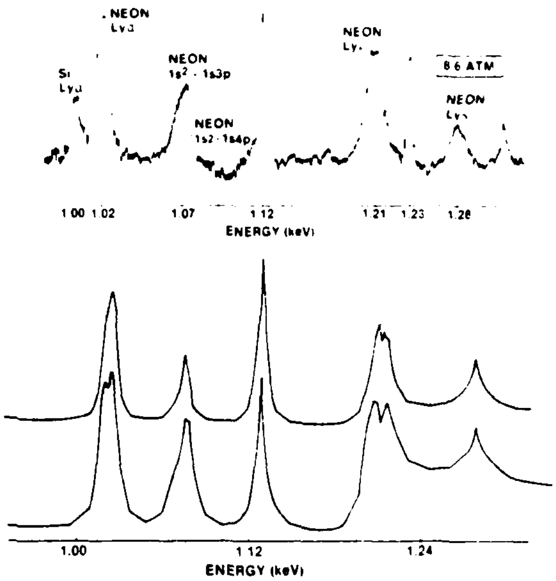

FIG. 2. The top spectrum was obtained by Yaakobi et al. at the University of Rochester from a laser-imploded microballoon filled with 8.6 atmospheres of neon. The bottom two spectra were calculated assuming CRE. The middle spectrum provides the best fit to the top one and arises from a plasma of $T_e = 385$ eV, $r = 11.4$ μm at $N_i \approx 4.5 \times 10^{23}$ cm^{-3}. *The bottom spectrum would be emitted* by a plasma of $T_e = 300$ eV, $r = 9.5$ μm, at $N_i = 7.8 \times 10^{23}$ cm^{-3}.

for argon compression diagnostics in the case of optically thin nonopacity broadened Stark lines.[14] The line profiles (as opposed to line intensities) are relatively insensitive to temperature.[16] However, effects of opacity broadening are specifically illustrated below in the interpretation of the Rochester neon experimental spectrum[1] taken by Yaakobi *et al.*

The pronounced temperature sensitivity of the emitted spectra is also apparent in Fig. 1. As the temperature is decreased from 600 to 450 to 250 eV, the intensity of the helium-like $1s^2$-$1s3p\ ^1P$ line at 1.074 keV increases dramatically relative to the hydrogen-like Ne X lines. In the Rochester spectrum, the Ne IX $1s^2$-$1s4p\ ^1P$ line (at 1.127 keV) was obscured by the impurity line Na X $1s^2$-$1s2p\ ^1P$, which is equal in wavelength to 1 part in 10^5. *In* fact this sodium line will optically pump the Ne IX level populations to some degree due to this close resonance. In the middle spectrum of Fig. 1 the effect of this impurity line has been included—the intensity having been derived from our computed fit to the Rochester spectrum[1] (taken by Yaakobi *et al.*) in Fig. 2. We included the sodium pumping line by assuming that the flux directed inward from the microballoon toward the neon filler is the same as the inferred flux directed outward. However, by calculating the emitted neon spectrum without the pumping influence of the impurity line, we have determined that the effect is negligible for these dense plasmas with high collisional cross-coupling rates between excited states. Therefore, *the line has been omitted in some of the calculated* spectra presented in Figs. 1–3, since its effect on the level populations is negligible.

Equally apparent as the helium line intensity change is the relative increase in the continuum radiation arising from recombination to the ground state of Ne IX as the temperature decreases. Indeed, at a temperature of 250 eV the Lyβ and Lyγ lines which sit on top of this continuum feature (whose edge lies at 1.196 keV) are more properly regarded as "line-continuum features" rather than pure lines. The appearance of this strong continuum edge can place strong constraints on the diagnosed temperature. Also, the continuum opacity may significantly affect both the shape and strength of the observed features arising from bound level transitions. Similarly, ionization by line photons—especially important when the lines are very wide due to Stark effects—may significantly affect the ionization balance of the plasma.

Having noted the spectral differences arising

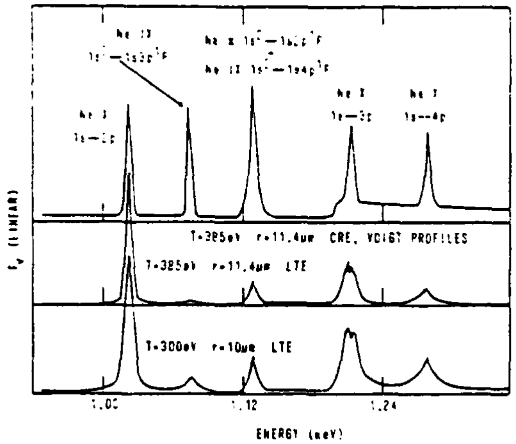

FIG. 3. The three calculated spectra shown represent the results of employing commonly used, but inaccurate, approximations. The top spectrum would be emitted by a neon plasma with pure Voigt line profiles whose conditions are those of the "best fit" of Fig. 2. The middle spectrum maintains the same physical conditions as the top, but Stark line profiles and LTE are assumed. The bottom spectrum arises from the same mass of plasma assumed to be in LTE but with a temperature of 300 eV and a radius of 10 μm. The sodium impurity line at 1.13 keV is included in these spectra.

from changes in density and temperature, we investigated the possibility of obtaining a fit to the Rochester experimental spectrum[1] using our first-principles ionization calculation, in which only temperature, density, size, and velocity variations in plasma conditions could be made.

The results of this effort are graphically summarized in Fig. 2, where the Rochester experimental spectrum (taken from Ref. 1) and two calculated spectra are displayed. The middle spectrum of Fig. 2 represents an excellent fit to the experimental spectrum displayed at the top of the figure. This "best-fit" calculated spectrum would arise from a spherical neon plasma of ion density 4.5×10^{21} cm^{-3} and radius 11.4 μm, having an electron temperature of 385 eV from $r=0$ to $r=8.8$ μm that then decreased smoothly to 296 eV at the surface. This gradient was inferred in a previous analysis of the degree of line self-reversals in such imploded plasmas,[14] and our present results support this gradient inference. Also shown in Fig. 2 (at the bottom) is the spectrum which would be emitted by a neon plasma characterized by the conditions originally inferred from the LTE analysis in Ref. 1. These conditions are $T_e=300$ eV (constant), $N_i=7.8\times10^{21}$ cm^{-3}, and $r\simeq9.5$ μm.

The need for a higher temperature and lower density than previously diagnosed is most readily understood by comparing the predicted 300-eV spectrum to the experimental one. The presence of the prominent continuum feature—the Ne IX ground-state ionization edge—in the 300-eV predicted spectrum is not matched by a similar feature in the experimental one. An explanation for its absence is that the experimental plasma contains less Ne IX and is therefore at a higher temperature, where more of the heliumlike neon is ionized. This degree of reduction of the continuum feature as the temperature increases is clearly evident in the theoretical spectra of Fig. 1, which served as a guide in obtaining the Fig. 2 fit to the Rochester experiment. A core temperature of 385 eV was needed to lower the calculated feature which is weak or nonexistent in the experimental spectrum. Moreover, temperatures higher than 385 eV were found to produce a Ne IX $1s^2$-$1s3p\,^1P$ line which was too weak to match the experimental line. Even at $T=400$ eV, the Fig. 2 comparison of calculated and experimental spectra deteriorated noticeably in this regard. Any temperature below 385 eV raises the helium continuum again producing a significant deterioration in the agreement even at our diagnosed density of 4.5×10^{21}. Our ability to zero in on 385 eV as the likely temperature in this manner strikingly illustrates both the need and the value of utilizing all of the information in the spectrum.

The Rochester analysis yielding $T_e\sim300$ eV was *based upon Planckian line ratios generated by an* LTE plasma. By contrast we find that a neon plasma of $T_e=300$ eV, $N_i=7.8\times10^{21}$ cm^{-3}, and $r=9.5$ μm has not reached LTE. Of the ionic species, only the Ne X concentration is close to its LTE value. Ne XI (bare nucleus) is about half of what would be expected in LTE, while heliumlike Ne IX has twice its LTE concentration. Moreover, the excited states of Ne X, whose radiative decay dominates the spectrum, are present to a far smaller degree than would be the case in LTE. The LTE excited-to-ground-state ratios of Ne X $n=2$, 3, 4, and 5 are, respectively, 0.13, 0.16, 0.23, and 0.32. We find that the highest ratios occur in the 300-eV model plasma at $r=0$, where they are 0.05, 0.06, 0.09, and 0.13, respectively. In effect, the ionization-excitation state of the plasma lags behind what is required for LTE. At an ion density of 7.8×10^{21} cm^{-3}, collisional processes dominate the coupling of the Ne X excited states to each other. Hence, these ratios of populations of the states lying above $n=2$ to that of $n=2$ do correspond to the required LTE ratios. The Ne X excited states are also in LTE with respect to the ground state lying above (the bare nucleus) due to the strength of collisional ionization and recombination processes. However, collisional excitation from and de-excitation to the NeX ground state from the excited states is generally at least two orders of magnitude weaker than collisional cross couplings among the excited states. Collisional deexcitation from the excited states to the ground state is also only about one-third as likely as spontaneous radiative decay to the ground state. Collisional processes are therefore not strong enough to enforce LTE between the ground and excited states of the *same* species—NeX. Moreover, due to the large Stark widths, the optical depths of Lyβ, γ, etc., are 2.2 or lower, as described below. Since these modest opacities do not permit multiple photon scattering, the states $n=3$ and above are weakly photoexcited and remain far from LTE with respect to $n=1$. However, since the optical depth of Lyα is ~200, it might at first be suspected that at least $n=2$ would be in LTE with respect to the ground state. The fact that this is not the case may be understood by applying the conditions required for LTE to the rate equations affecting the two states $n=1$ and 2. For simplicity we first consider the two-level-atom case in an optically thick plasma characterized by a line photon escape probability P_e. We let W_{21} stand for the collisional deexcitation rate coefficient and A_{21} stand for the spontaneous emission coefficient. The steady-state condition requires

$$N_2(W_{21}+A_{21}P_e)=N_1\left(W_{21}\frac{g_2}{g_1}e^{-h\nu/kT}\right), \qquad (1)$$

where photon reabsorption is accounted for by diluting the spontaneous emission coefficient by a factor equal to the mean photon escape probability. From Eq. (1),

$$\frac{N_2}{N_1}=\frac{(g_2/g_1)e^{-h\nu/kT}}{1+(A_{21}P_e/W_{21})}. \qquad (2)$$

For N_2/N_1 to have the LTE population ratio of these two levels, $(g_2/g_1)e^{-h\nu/kT}$, we must have

$$A_{21}P_e \ll W_{21}. \qquad (3)$$

Therefore, even a very optically thick plasma can be far out of LTE if $A_{21} \gg W_{21}$ to the extent necessary to offset a small P_e. That is, the mere existence of a small P_e due to large optical depth does not ensure the validity of Eq. (3). Therefore, the fact that Lyα is quite thick in this case does not in itself justify an LTE assumption. For the plasma conditions under consideration here, $A_{21} \cong 2.5W_{21}$. Therefore, LTE will not be valid near the surface of the plasma, where $P_e \approx 0.5$, since $A_{21}P_e \gtrsim W_{21}$ in this region. Of course, the emitted spectrum of optically thick lines tends to be dominated by surface emission. Nevertheless, one still might expect LTE to prevail in the optically thick interior based on the above two-level-atom analysis. However, there are three separate effects which in this case prevent LTE conditions from being established even in the thick plasma interior. First, even though the optical depth of Lyα is ~200, the line wings are so prominent at this high density that the mean escape probability is found numerically to be 0.06. Thus, $A_{21}P_e \cong 0.15\,W_{21}$ in the interior. According to Eq. (2) this alone will reduce the N_2/N_1 ratio to 0.87 times that of LTE. The other two effects which bring the actual ratio to only 0.38 times the LTE ratio are, first, a radiative leak in the Lyβ line, where $\tau \cong 2$, and, second, another photon escape mechanism in the optically grey recombination continuum from the bare nucleus to the ground state of NeX. A multilevel analysis is necessary to clarify the detailed contributions of the latter two mechanisms.

An accurate analytic treatment is possible in this case because the very large collisional rates coupling the excited states ($n=2$, 3, 4, 5, and NeXI) force the ratios of these states to each other to equal those of LTE, as confirmed by the calculated population densities. Let L_{ij} denote the LTE ratio of state i to state j. Then, the equation for the steady-state coupling of NeX $n=1$ to the overlying states becomes

$$N_1\left(\sum_{i=2}^{6} W_{1i}\right)=N_2\left((A_{21}P_{e21}+W_{21})\right.$$
$$+\sum_{i=3}^{5} L_{i2}(A_{i1}P_{ei1}+W_{i1})$$
$$\left.+L_{62}(W_{R61}N_eP_{e61})\right). \qquad (4)$$

In Eq. (4) W_{ij} is the collisional rate coupling states i and j, P_{eij} is the escape probability for the photon emitted during a radiative transition from state i to j, A_{ij} is the spontaneous transition probability, and W_{R61} is the radiative recombination rate from the bare nucleus to NeX $n=1$. Equation (4) contains all of the important processes populating and depopulating NeX $n=1$ at this temperature and density. The processes which are omitted—collisional recombination from NeXI and its inverse, and ionization and recombination processes from and to NeIX—are relatively unimportant compared to what is included, and thus their omission does not quantitatively affect this analysis. Equation (4) is easily solved for N_2/N_1. When the collisional rates and Einstein A's are inserted, the ratio N_2/N_1 is found to be a function of the escape probabilities for a particular plasma temperature, density, and size. For Lyβ, the numerical results yield $P_{e31} \cong 0.7$, and for the $n=1$ recombination continuum $P_{e61} \cong 0.3$. The Lyβ radiation leak in concert with Lyα, γ, and δ would reduce N_2/N_1 to 0.65 times the LTE ratio; inclusion of the free-bound continuum leak brings the ratio down to the actual 0.05, which is 0.38 that of LTE. Photon escape in Lyγ and Lyδ makes little difference since their spontaneous transition probabilities are factors of 4.4 and 13.5, respectively, below that of Lyβ.

In summary, escape of radiation in the optically grey Lyβ and NeXI continuum transitions adds to the radiation escape in the line wings of Lyα and prevents LTE from being established even in the plasma interior. While the strong collisional coupling of the states above NeX $n=1$ forces $n=3$ and above into LTE with $n=2$, it in turn adds to the escape of radiation emitted during decays of these levels and further reduces all the excited-state populations relative to $n=1$. Fundamentally, the lack of detailed balancing of all of the NeX radiation—i.e., by *reabsorption*—prevents LTE conditions from being established.

The need for a reduced density in order to explain the observed spectrum (from 7.8×10^{21} to 4.5×10^{21} cm^{-3}) is implied by two features of the predicted spectrum at 7.8×10^{21} cm^{-3}; namely, the Lyα, Lyβ, and Lyγ lines are too wide, and the Lyα line exhibits a self-reversal which is not observed. We will first consider the question of the Lyβ and γ lines. As previously mentioned, the total concentration of hydrogenlike NeX in our 300-eV model plasma is roughly equal to the LTE value. However, since our excited-state densities are much less than the LTE amounts, the ground state has a greater than LTE density—varying from 75% greater at the center ($r=0$) to 2.2 times greater at the plasma surface. The reason for this spatial gradient is that the radiation field is less intense at the surface, which therefore, with less optical pumping, contains fewer bare nuclei and more hydrogenlike neon. The optical depths of Lyβ and Lyγ in collisional-radiative equilibrium are therefore about twice the previously assumed LTE values. We find a peak optical depth of 2.2 for Lyβ in contrast to the value of 1.2 that was previously used[1] to calculate the first-order opacity-broadening correction. This results in a 50% increase in linewidth because of the extra opacity broadening. Also, we do not find that the Lyγ line is optically thin; instead, it has a peak optical depth of 1.1. In summary, significantly greater opacity broadening for both Lyβ and Lyγ occurs in CRE than in LTE, which forces a reduction in density in order to reduce the Stark and opacity widths to fit the experimental spectrum.

As noted above, the 300-eV model plasma predicts an asymmetric self-reversal for Lyα. This asymmetry is due to the effects of plasma motion. The self-reversal itself is a well-known effect of large line opacity in a non-LTE plasma. Reducing the linewidth by reducing the density from 7.8×10^{21} to 4.5×10^{21} cm^{-3} turns the self-reversal into a "shoulder" which is more consistent with experiment. The increased temperature of 385 eV reduces the fraction of ground state NeX, and thus the Lyα opacity, contributing to this effect. The width of the opacity-broadened Lyα line is also in very good agreement with experiment when this lower density is assumed, as is apparent in Fig. 2.

IV. EFFECTS OF SIMPLIFYING ASSUMPTIONS ON THE CALCULATED SPECTRA

We have seen above that neither Voigt profiles nor LTE are valid assumptions for the physical state of these high-density neon plasmas. However, it is of interest to invert the analysis and examine spectra calculated using these erroneous assumptions in order to estimate the magnitude of error. Figure 3 displays three spectra which represent the results of employing commonly used, but inaccurate approximations. The top spectrum was computed using conditions identical to those of the "best fit" to the experimental spectrum at the top of Fig. 2, except that Voigt rather than Stark line profiles were used. Consequently, the much narrower lines of this spectrum bear little resemblance to the observed spectrum or to the theoretical Stark-profile spectrum in the middle of Fig. 2. The bottom two spectra of Fig. 3 were computed with Stark profiles but with the LTE assumption. Since the true excitation state of the plasma lags behind LTE, when LTE is assumed, the theoretical excitation state is increased, resulting in more ionization and less Ne IX. The reduced heliumlike neon is reflected in the very weak Ne IX $1s^2$-$1s3p\,^1P$ line, which for $T=300$ or 385 eV is much less intense than that which is measured. Also, the Ne IX ground-state recombination continuum is much reduced, especially in the case of the 300-eV spectrum. Neither LTE spectrum agrees with experiment. It is conceivable that an LTE spectrum of neon at a much lower temperature might show a relatively increased Ne IX $1s^2$-$1s3p\,^1P$ line and thus agree more closely with the experimental spectrum of Fig. 2. However, the lower temperature would reduce the collisional rates even further—meaning that LTE would be an even more inappropriate model.

V. SUMMARY AND CONCLUSIONS

We have utilized a first-principles, multistate, multilevel model of highly ionized, high-density neon to predict the emitted spectrum as a function of the compressed state of the plasma. The appearance of the spectrum has been found to sensitively reflect this state, and the particular features which change in accordance with the various plasma properties have been noted and the underlying physics discussed. The model has been found capable of generating an excellent detailed fit to a previously published experimental spectrum, and the fitting process has led to a considerable refinement of the inferred plasma conditions, including an estimate of the extreme sensitivity of the predicted spectrum to these conditions.

One should note that the authors of Ref. 1 attempted only to obtain an approximate temperature to aid in inferring the density. On the other hand, it is our purpose here to illustrate the potential of non-LTE spectroscopic analysis for obtaining accurate temperatures as well as accurate densities. We have shown that despite the complexity of the dynamics of compression, detailed, realistic, and accurate modeling of the radiative output is both possible and fruitful.

ACKNOWLEDGMENTS

The authors wish to thank Dr. B. Yaakobi for granting permission to use his spectra and for providing a copy for reproduction here. This work was supported in part by the Defense Nuclear Agency.

---

[*] Science Applications, Inc., McLean, Va.

[†] Optical Sciences Division.

[1] B. Yaakobi, D. Steel, E. Thorsos, A. Hauer, and B. Perry, Phys. Rev. Lett. 39, 1526 (1977).

[2] K. G. Whitney, J. Davis, and J. P. Apruzese, Phys. Rev. A 22, 2196 (1980).

[3] H. R. Griem, M. Blaha, and P. C. Kepple, Phys. Rev. A 19, 2421 (1979).

[4] D. Duston and J. Davis, Phys. Rev. A 21, 1664 (1980).

[5] K. G. Whitney and J. Davis, J. Appl. Phys. 45, 5294 (1974); J. Davis and K. G. Whitney, *ibid.* 47, 1426 (1976).

[6] M. J. Seaton, Proc. Phys. Soc. London 79, 1105 (1962).

[7] V. L. Jacobs, J. Davis, P. C. Kepple, and M. Blaha, Astrophys. J. 211, 605 (1977).

[8] W. J. Karzas and B. Latter, Astrophys. J. Suppl. Ser. 6, 167 (1961).

[9] V. L. Jacobs and J. Davis, Phys. Rev. A 18, 697 (1978).

[10] L. A. Vainshtein and I. I. Sobel'man, Lebedev Report No. 66 (unpublished).

[11] J. Davis, P. C. Keeple, and M. Blaha, J. Quant. Spectrosc. Radiat. Transfer 16, 1043 (1976).

[12] D. Duston, J. Davis, and K. G. Whitney, NRL Memorandum Report No. 3846 (unpublished).

[13] J. P. Apruzese, J. Davis, and K. G. Whitney, J. Appl. Phys. 48, 667 (1977).

[14] S. Skupsky, University of Rochester Laboratory for Laser Energetics Report No. 80 (unpublished).

[15] B. Yaakobi, S. Skupsky, R. L. McCrory, C. F. Hooper, H. Deckman, P. Bourke, and J. M. Soures, Phys. Rev. Lett. 44, 1072 (1980).

[16] A. Hauer, K. B. Mitchell, D. B. Van Hulsteyn, T. H. Tan, E. J. Linnebur, M. M. Mueller, P. C. Kepple, and H. R. Griem, Phys. Rev. Lett. 45, 1495 (1980).

Appendix C

PLASMA CONDITIONS REQUIRED FOR ATTAINMENT OF MAXIMUM GAIN IN RESONANTLY PHOTO-PUMPED Al XII AND Ne IX

(This page intentionally left blank.)

NRL Memorandum Report 4618

Plasma Conditions Required for Attainment of Maximum Gain in Resonantly Photo-Pumped Al XII and Ne IX

J. P. Apruzese

Science Applications, Inc.
McLean, VA 22102

J. Davis

Plasma Radiation Group
Plasma Physics Division

K. G. Whitney

Applied Optics Branch
Optical Sciences Division

October 9, 1981

This research was sponsored by the Defense Nuclear Agency under Substask T99QAXLA014, work unit 37, and work unit title, "Advanced Concepts Theory Program."

NAVAL RESEARCH LABORATORY
Washington, D.C.

(This page intentionally left blank.)

REPORT DOCUMENTATION PAGE		READ INSTRUCTIONS BEFORE COMPLETING FORM
1. REPORT NUMBER NRL Memorandum Report 4618	2. GOVT ACCESSION NO.	3. RECIPIENT'S CATALOG NUMBER
4. TITLE (and Subtitle) PLASMA CONDITIONS REQUIRED FOR ATTAINMENT OF MAXIMUM GAIN IN RESONANTLY PHOTO-PUMPED Al XII AND Ne IX		5. TYPE OF REPORT & PERIOD COVERED Interim report on a continuing NRL problem. 6. PERFORMING ORG. REPORT NUMBER
7. AUTHOR(s) J. P. Apruzese*, J. Davis, and K. G. Whitney		8. CONTRACT OR GRANT NUMBER(s)
9. PERFORMING ORGANIZATION NAME AND ADDRESS Naval Research Laboratory Washington, DC 20375		10. PROGRAM ELEMENT, PROJECT, TASK AREA & WORK UNIT NUMBERS 62704H; 47-0858-0-1
11. CONTROLLING OFFICE NAME AND ADDRESS Defense Nuclear Agency Washington, DC 20305		12. REPORT DATE October 9, 1981 13. NUMBER OF PAGES 24
14. MONITORING AGENCY NAME & ADDRESS(if different from Controlling Office)		15. SECURITY CLASS. (of this report) UNCLASSIFIED 15a. DECLASSIFICATION DOWNGRADING SCHEDULE
16. DISTRIBUTION STATEMENT (of this Report) Approved for public release; distribution unlimited.		
17. DISTRIBUTION STATEMENT (of the abstract entered in Block 20, if different from Report)		
18. SUPPLEMENTARY NOTES *Present address: Science Applications, Inc., McLean, VA 22102 This research was sponsored by the Defense Nuclear Agency under Subtask T99QAXLA014, work unit 37, and work unit title, "Advanced Concepts Theory Program."		
19. KEY WORDS (Continue on reverse side if necessary and identify by block number) Plasma mixture Radiative pumping X-ray lasing Plasma diagnostics		

20. ABSTRACT (Continue on reverse side if necessary and identify by block number)

We present a detailed analysis of the plasma conditions required to optimize gain in two proposed x-ray lasing schemes using resonant photo-pumping. In one proposed configuration, the Si XIII line $1s^2$-$1s2p^1P$ at 6.650 Å pumps Al XII $1s^2$-$1s3p^1P$ at 6.635 Å, inverting the Al XII n = 3 and n = 2 levels which are separated by 44 Å. A similar approach which utilizes the Na X $1s^2$—$1s2p^1P$ line at 11.00 Å to pump the Ne IX $1s^2$-$1s4p\ ^1P$ line at 11.001 Å would invert the n = 3 and n = 2 levels of Ne IX, separated

(Continues)

20. ABSTRACT (Continued)

by 82 Å. Conditions in the pumped neon and aluminum plasmas, and in the pumping silicon plasma, are calculated using a multistage, multilevel atomic model with multifrequency radiation transport. For modeling the pumping sodium line we have inferred the intensity from a spectrum of a neon filled, laser-imploded glass microballoon containing sodium impurities obtained at Rochester. It is found that peak gain of about 100 cm^{-1} occurs at ion densities of 10^{20} cm^{-3} and 4×10^{20} cm^{-3} in the pumped neon and aluminum plasmas, respectively. At higher ion densities the inversions are rapidly collisionally quenched. Temperatures required to maximize gain in the pumped plasmas are found to be 50 eV and 100 eV, for neon and aluminum, respectively. Plasmas of lower temperature do not contain enough of the active ion species, whereas at higher temperatures the photon pumping of the upper levels results in excessive ionization from these levels to the hydrogen-like species. Finally, since the pumping silicon and pumped aluminum lines are slightly off resonance, we have investigated the effect of streaming the plasmas toward each other at various velocities to offset some or all of the wavelength difference. It is found that a streaming velocity of 6.8×10^7 cm sec^{-1}—fully offsetting the wavelength difference—will approximately triple the achieved gain compared to the zero velocity case. Lesser increases in gain occur with partial velocity offsets.

CONTENTS

(This page intentially left blank.)

PLASMA CONDITIONS REQUIRED FOR ATTAINMENT OF MAXIMUM GAIN IN RESONANTLY PHOTO-PUMPED Al XII AND Ne IX

I. Introduction

It has been suggested[1-4] that population inversions in plasmas may be efficiently pumped by opacity broadened lines from different ionization stages of the same element or from different elements in a two component plasma. Experimental evidence[5,6] has been presented for inversions of the $n = 4$ and $n = 3$ levels in Mg XII and Mg XI, which were pumped by resonant Lyα and $1s^2$-$1s2p\,^1P$ radiation in C VI and C V. The abovementioned lasing transitions in Mg lie at ~130 and 156 Å for Mg XII and Mg XI, respectively. In this paper we present a detailed analysis of the plasma conditions which would be needed to optimally implement two promising lasing schemes utilizing resonant photoexcitation with considerably shorter lasing wavelengths (82 Å and 44 Å). The radiation field--critical in a photoexcitation process--is modeled in detail. The pumped and pumping transitions--as well as other key optically thick lines--are calculated on a frequency grid allowing for accurate modeling of broadening processes and frequency-dependent absorption. Previous efforts at modeling short-wavelength resonantly photo-excited lasing processes have employed assumed linewidths[1], line profiles arising from uniform source functions[2], assumed power densities[3,5], or probability-of-escape approximations[4]. In another study[7], the pumped plasma was modeled with a fine frequency grid but the pumping spectrum was assumed to be a filtered Planckian. In section II our atomic model is described along with the methodology for its employment for calculations for both the pumped and pumping plasmas. In section III the equilibrium results are presented for optimum plasma densities, temperatures, and relative velocities and the relevant physical processes controlling these effects are analyzed. Finally, we summarize the work and present our basic conclusions in section IV.

Manuscript submitted July 28, 1981.

II. Description of Model and Calculations

A. Basic Details of Models

The photon pumping schemes to be analyzed are the following. Scheme 1 would employ the Si XIII $1s^2$-$1s2p\,^1P$ resonance line at 6.650 Å to pump the Al XII $1s^2$-$1s3p\,^1P$ resonance line at 6.635 Å, creating an inversion of the $n = 3$ and $n = 2$ levels of Al XII. Scheme 2 utilizes the Na X $1s^2$-$1s2p\,^1P$ line at 11.00 Å to pump the Ne IX $1s^2$-$1s4p\,^1P$ line at 11.001 Å, creating an inversion primarily in the $n = 3$ and $n = 2$ levels of Ne IX. Scheme 1 results in stimulated emission at 44 Å and scheme 2 at 82 Å. Ionic state and level densities as well as the radiation field are computed for Al using the model described in ref. 7. For Si, a precisely analogous model to Al--the same level structure and transitions--is employed. The Ne atomic model is described in ref. 8. This model possesses an extra degree of sophistication in that self-consistent Stark profiles[9] are used for the line opacity rather than the Voigt profiles employed for Al and Si. For Na, no atomic model is employed. Rather, the profile of the pumping line at 11.00 Å is utilized as it was experimentally measured from glass impurities in a laser implosion experiment at the University of Rochester[10]. The multifrequency measured profile is modified within the pumped neon plasma by absorption and re-emission in the Ne line and this phenomenology is computed in detail using the flux profile of the Na line as an input condition on the Ne plasma. Further details are given below in subsection C. Results given below are calculated for collisional-radiative equilibrium (CRE).

B. Pumped Plasma Calculation

As previously pointed out[6], radiation trapping effects in the pumped plasma can generally be minimized or eliminated by making the transverse dimensions of the plasma small. We have followed this approach in modeling the pumped plasma--the radiation field is calculated in a planar plasma of infinite area with thickness small enough to insure an optically thin regime over a broad angular range of specific intensities. Our objectives—given an optically thin lasing medium--are to determine a range of temperatures, densities, and, for scheme 1, streaming velocities that will optimize gain and to determine some of the tradeoffs involved. We have previously discussed trapping effects in the pumped plasma in refs. 4 and 7.

The pumped plasma is assumed to be bathed symmetrically in the pumping radiation which is calculated (for Si) or measured (for Na). The penetration of the pumping radiation into the pumped plasma is calculated in a straightforward manner. At the outer boundaries of the pumped plasma the inward specific intensity along each ray at each frequency I_ν^- is taken to be that emitted from the pumping plasma which is also assumed to be planar. The radiative transfer equation is then solved in the pumped plasma with this particular boundary condition for I_ν^- applied at each of the chosen rays at the outer boundaries of the pumped plasma. The calculation in the pumped plasma then proceeds by iteration until steady state conditions are obtained. Since fully coupled radiative transport and rate equations are solved in this model, the steady state obtained is a self-consistent collisional radiative equilibrium. The quantity of primary interest here--the gain coefficient of the lasing transition--is obtained as a linear function of the computed densities of the upper and lower states. Finally, the temperature, density and (for Al) velocity of the pumped plasma was varied in order to obtain the functional dependence of the gain coefficient on these quantities. We make no attempt to calculate the depletion of excited states by lasing, and thus are computing only the linear amplifier behavior.

C. Treatment of the Pumping Plasma

Our principal objective is to determine the effect of varying conditions in the pumped plasma on the achieved gain. Therefore, we selected only one set of pumping conditions for each of the Si and Na plasmas. Since the $1s^2$-$1s2p^1P$ Si XIII and $1s^2$-$1s3p^1P$ Al XII lines are off resonance by 0.015 Å, the profile of the $1s^2$-$1s2p^1P$ line must be wide enough to produce significant intensity at 0.015 Å (i.e. 13 Doppler widths at 400eV) from line center. Thus, for a stationary plasma the line must be opacity broadened[2]. If the resonance line is very thick at line center, the Lorentz wings will still exceed optical depth unity many Doppler widths from line center, guaranteeing a wide profile. Such conditions can be obtained in a moderate energy Si plasma of 1.5 mm width, temperature 400eV, and ion density $8X10^{19}cm^{-3}$. Plasmas similar to this have been realized in the laboratory[11]. Most importantly, the CRE calculation for this plasma indicates that, depending on position, 62-82% of the ions are in the active (helium-like) stage. Furthermore, the optical depth of the pumping resonance line $1s^2$-$1s2p^1P$ is ~500, which produces a very wide profile, as shown in Fig. 1. In addition to the calculated emission profile the

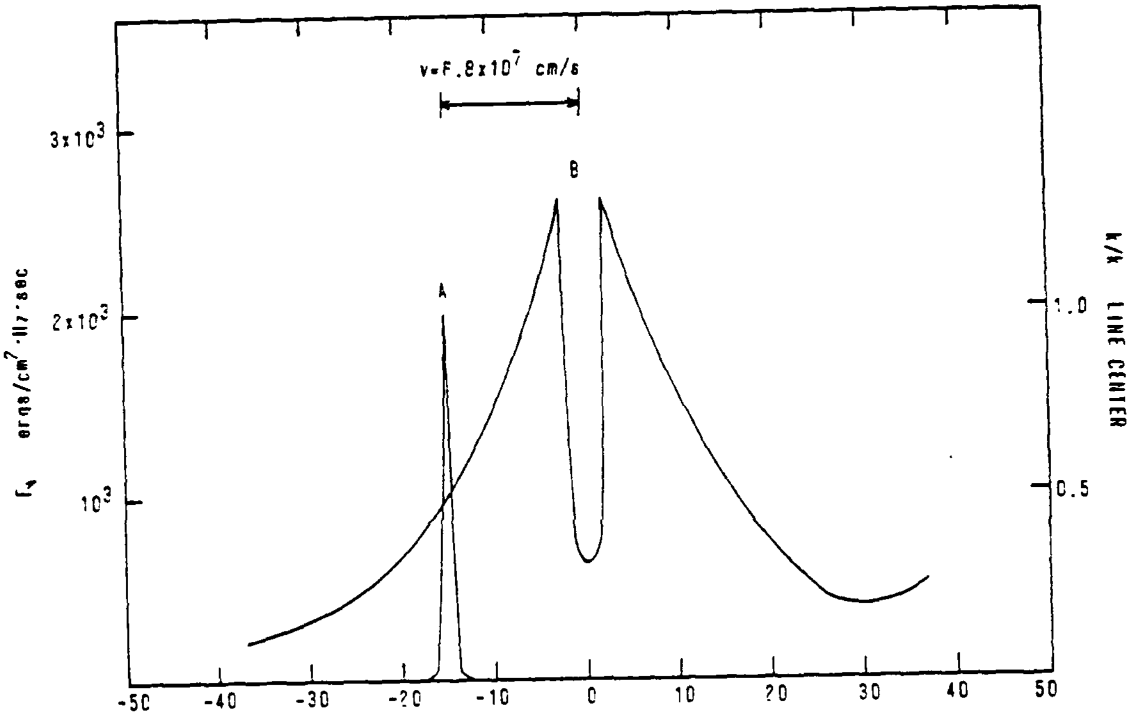

Fig. 1 — The line profile of the Si pumping line (B) calculated to arise from the indicated plasma conditions is shown on the same wavelength scale as the intrinsic absorption profile of the pumped Al line (A). The left vertical scale applies to the flux of the emitted Si line; the right vertical scale applies to the absorption coefficient of the Al line.

intrinsic absorption profile for the $1s^2$-$1s3p^1P$ Al XII line is shown for typical conditions in the aluminum plasma. In this case, the Si resonance line is sufficiently broadened by opacity to overcome the resonance defect. Therefore, under the reasonable assumption that these equilibrium Si plasma conditions be achieved the Si/Al lasing scheme will be viable at least in this sense that the resonance defect can be overcome.

To obtain a radiation source to pump Ne, we have analyzed the spectrum of a laser-imploded neon filled glass microballoon obtained at Rochester[1c]. One of the strongest lines appearing in this spectrum is that of the Na X $1s^2$-$1s2p^1P$ line--which arose from sodium impurities in the glass. Since we have been able to reproduce the observed spectrum with a first-principles non-LTE calculation of the line and continuum intensities[5], the theoretical calculation which matches the observed spectrum also yields the absolute intensities of the lines--(flux in ergs/cm^2-sec-Hz) at the outer surface of the pellet. Knowing the absolute intensities of the Ne lines, one may infer the Na line intensity profile from its measured intensity relative to the Ne lines. Its value at the central peak is 6.6×10^3 ergs/(cm^2-sec-Hz). It is this intensity profile which we use as our pump source in the Na/Ne calculations discussed in the next section.

The frequency profile is the one appearing in the published spectrum[1c], where experimental sources of broadening are relatively small. In any event deconvoluting any experimental broadening would result in a sharper central peak, which, since the lines are perfectly resonant, would give a better pump source. In the next section it is shown that this experimentally observed Na X $1s^2$-$1s2p^1P$ line intensity profile is sufficient to pump a substantial inversion in the Ne X $n = 2$ and $n = 3$ levels. This finding is significant in light of the fact that this radiation was merely a consequence of sodium impurities in the glass, i.e. no effort was made to increase its intensity in the experiment. We note that only the radiation of the Na resonance line was used to pump Ne, whereas the pumping effects of all the calculated Si radiation-pumping plus other lines plus continuum, were included in the Al calculation.

III. Results of Gain Calculations

A. Density Dependence

A principal question related to the time varying conditions in the pumped plasma is: at what density is gain maximized? As has been often pointed out[3,4,6,12], there exists for each lasing scheme contemplated a density above which no inversion is possible, due to the tendency of collisional processes to bring the state densities into LTE. At much lower densities one also expects that the gain coefficient will be reduced purely because there are fewer lasing ions in a given linear distance. It is evident that some density must exist at which the gain in steady state will be a maximum. This behavior is shown in Figs. 2 and 3, where the results of detailed calculations for various pumped plasma densities are presented for Si/Al and Na/Ne, respectively. In each case the gain for the strongest of the 2-3 lines (the 2p-3d) is plotted against the pumped plasma's density. For Ne, the assumption of statistical equilibrium for the $n = 3$ singlet sublevels is enforced, whereas, for the Si/Al calculation, results are presented with this assumption both enforced and relaxed. The chosen temperatures approximately correspond to maximum values for gain, this point is discussed further in the next section. Note that substantial peak gains - of 10^2 cm^{-1} or more - are obtained for both schemes. For the Si/Al calculations, zero relative velocity between the two components was assumed. The assumption of statistical equilibrium leads to an overestimate of gain at low densities; however, for densities near the predicted peak gain, around $4X10^{20}$ cm^{-3}, the overestimate is very slight. This effect is due to the increasing validity of the statistical equilibrium assumption at higher densities as collisional processes dominate the populating of the sublevels.

For Al, peak gain occurs at an ion (electron) density of $4X10^{20}$ ($1.2X10^{21}$) cm^{-3}, for Ne the corresponding figures are 10^{20} ($8.1X10^{20}$) cm^{-3}. For hydrogenic lasing schemes, Bhagavatula[3,6] has presented reduced variable equations which demonstrate that the dependence of electron density at peak gain on Z is Z^7. We note with interest that the Z-dependence of electron density at peak gain implied by the above numbers for our helium-like schemes is fairly similar, $Z^{6.3}$.

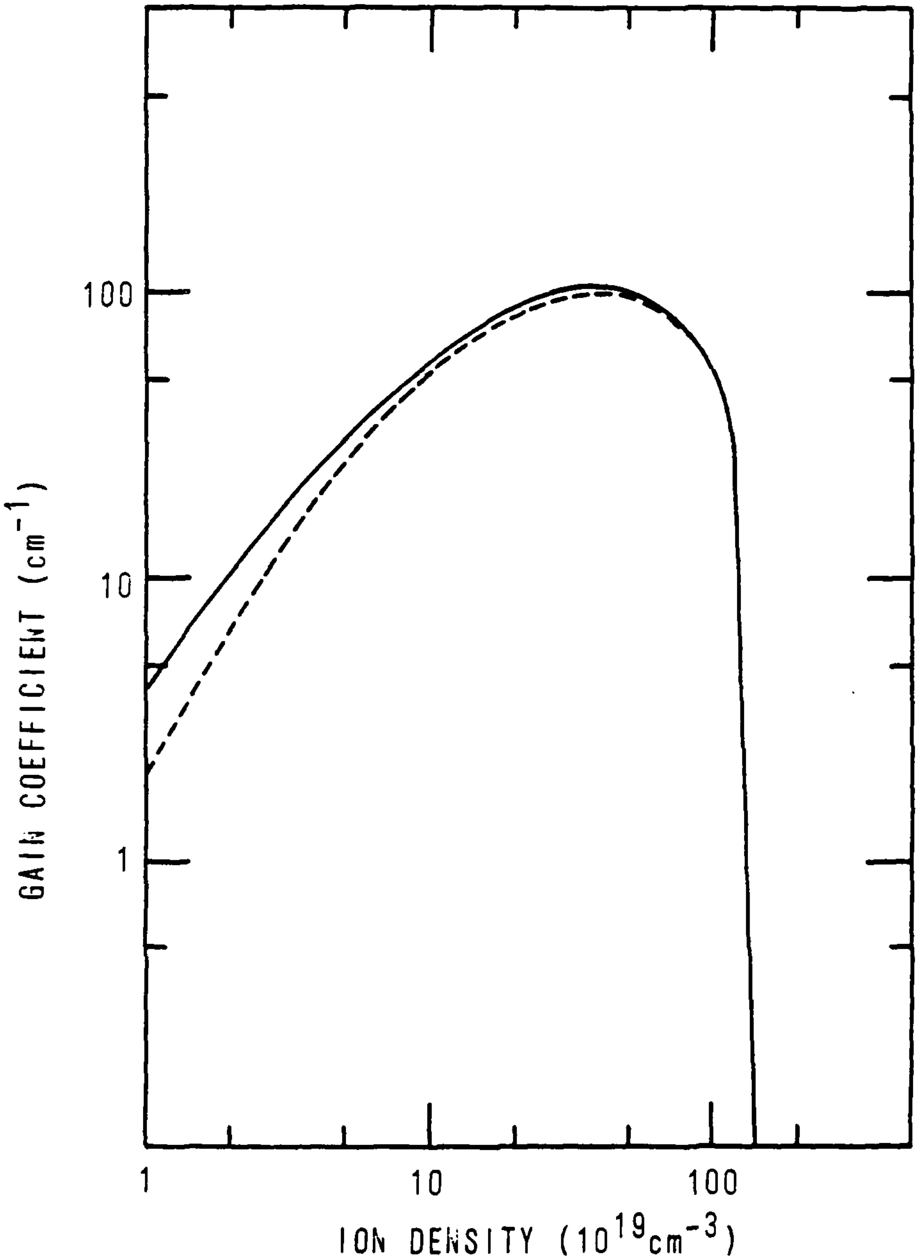

Fig. 2 — Line center gain coefficient in the Al XII $2p^1P$-$3d^1D$ line is plotted vs. Al plasma ion density, with an assumed pumped plasma temperature of 100 eV. Dual results for the assumption of collisional equilibrium (solid line) between the 3p-3d states and for a general, rate-by-rate treatment of these states are displayed. Characteristics of the pumping Si plasma are discussed in the text.

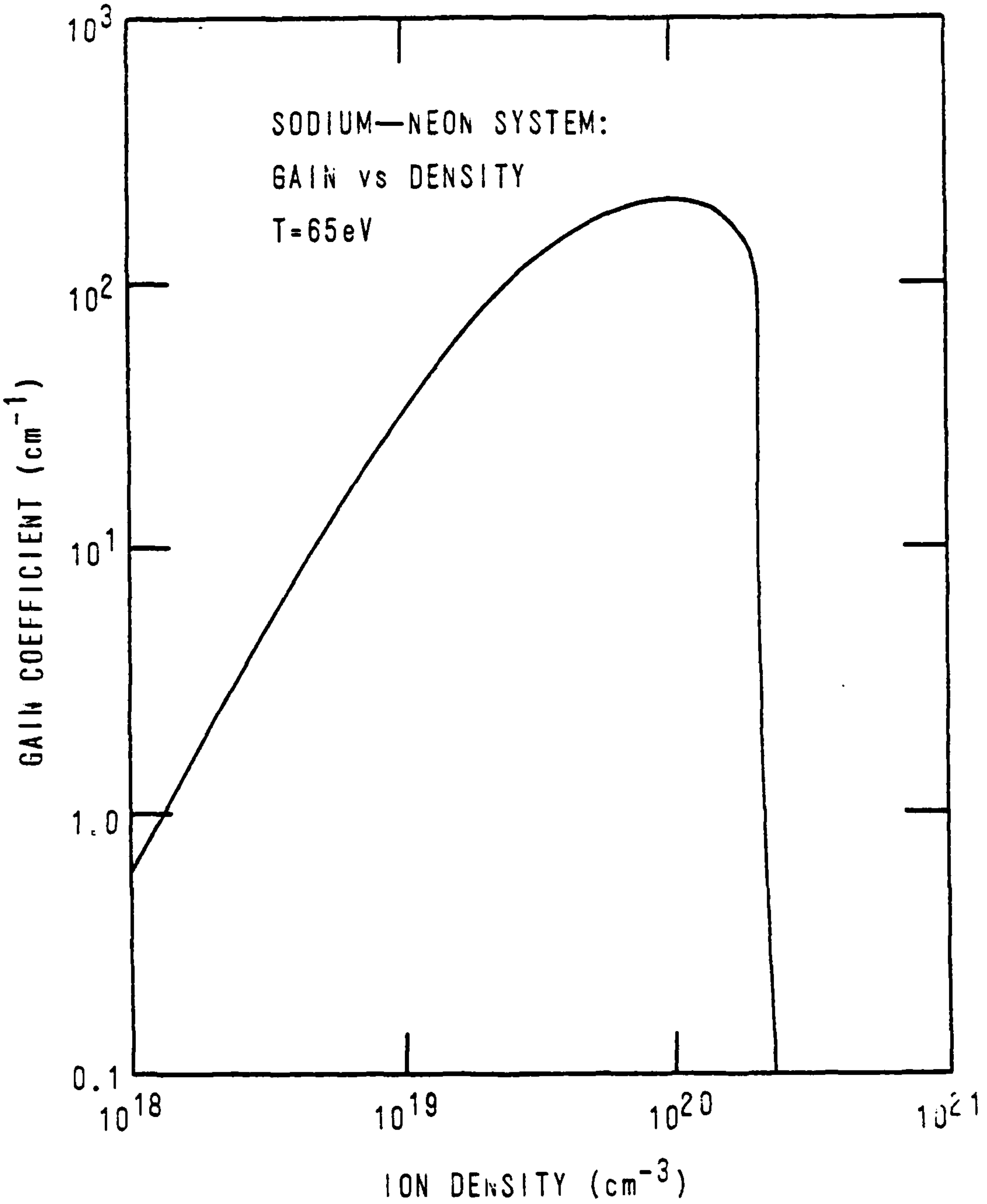

Fig. 3 — Line center gain coefficient in the Ne IX $2p^1P$-$3d^1D$ line is plotted vs. Ne plasma ion density, for an assumed pumped plasma temperature of 65 eV.

B. Temperature Dependence

In Figs. 4 and 5 results for gain vs. temperature are plotted for the Si/Al and Na/Ne systems for fixed ion densities of $5\text{X}10^{19}$ cm^{-3} and 10^{20} cm^{-3}, respectively. The gain dependence on temperature is similar to that on density in that a maximum is exhibited with a sharp falloff on one side caused by the variation of the active ion species' populations with temperature. Note however, that the temperature of maximum gain is much lower than one would expect from coronal model calculations of the ionic species abundances. Such calculations[13] reveal that helium-like ion concentrations peak at 120eV and 330eV for Ne and Al, respectively. The present calculations predict corresponding peak gains at 50eV and 100eV. These lower pumped plasma temperatures are necessitated by the radiative pumping to the $n = 4$ and $n = 3$ bound levels in the two schemes which greatly facilitates collisional ionization. Hence peak lasing ion abundance is forced to much lower temperatures where fewer electrons are capable of ionization from these bound states. At still lower temperatures a sharp gain and abundance falloff occurs as the plasma assumes a more normal configuration when the "extra" ionization becomes small. In these two lasing systems, the strength of the pumping decisively affects the temperature at which the pumped plasma must be prepared for maximum gain to occur. Such effects have been noted elsewhere[6,7] in somewhat different contexts.

C. Velocity Dependence

For the Na/Ne system, the pumped and pumping lines are within resonance to 1 part in 10^5, and thus there is no question as to the adequacy of the wavelength coincidence. For Si/Al, however, the wavelength difference of 0.015 Å amounts to 13 Doppler widths at 400eV. For a photon travelling at normal incidence to the pumped plasma, this resonance defect could be made up if the two plasmas stream toward each other at $6.8\text{X}10^7$ cm sec^{-1}. But given the wide opacity broadened pumping line profile (Fig. 1) the functional dependence of gain on plasma streaming velocity must be calculated; this result is presented in Fig. 6. In these calculations, the frequencies of the radiation incident on the pumped plasma were shifted angle-by-angle to reflect the streaming velocities indicated. Even though there is a substantial self-reversal at the center of the pumping line, peak gain does indeed occur for the matched streaming velocity of $6.8\text{X}10^7$

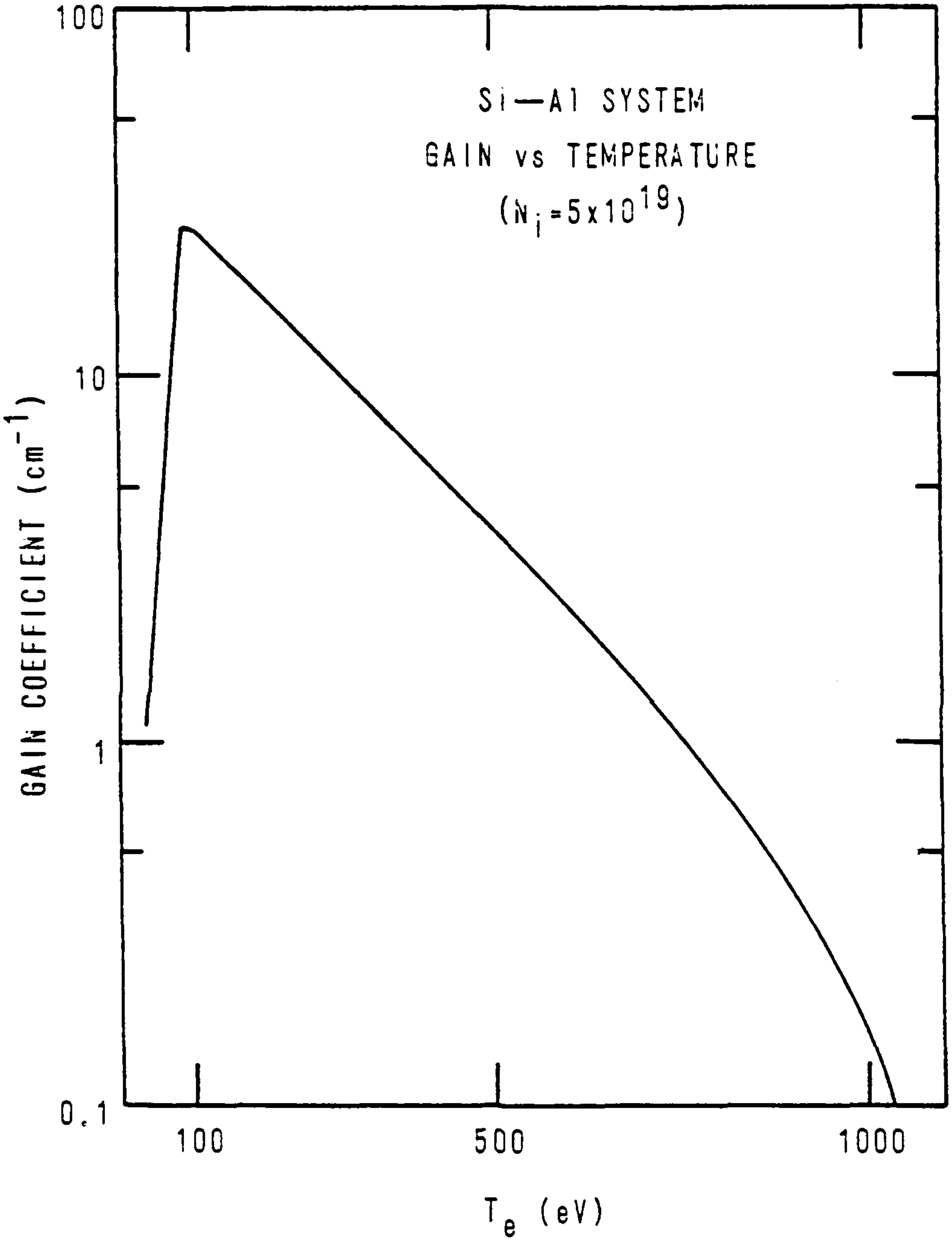

Fig. 4 — Line center gain coefficient in the Al XII $2p^1P$-$3d^1D$ line is plotted vs. Al plasma temperature for a fixed Al ion density of 5×10^{19} cm^{-3}.

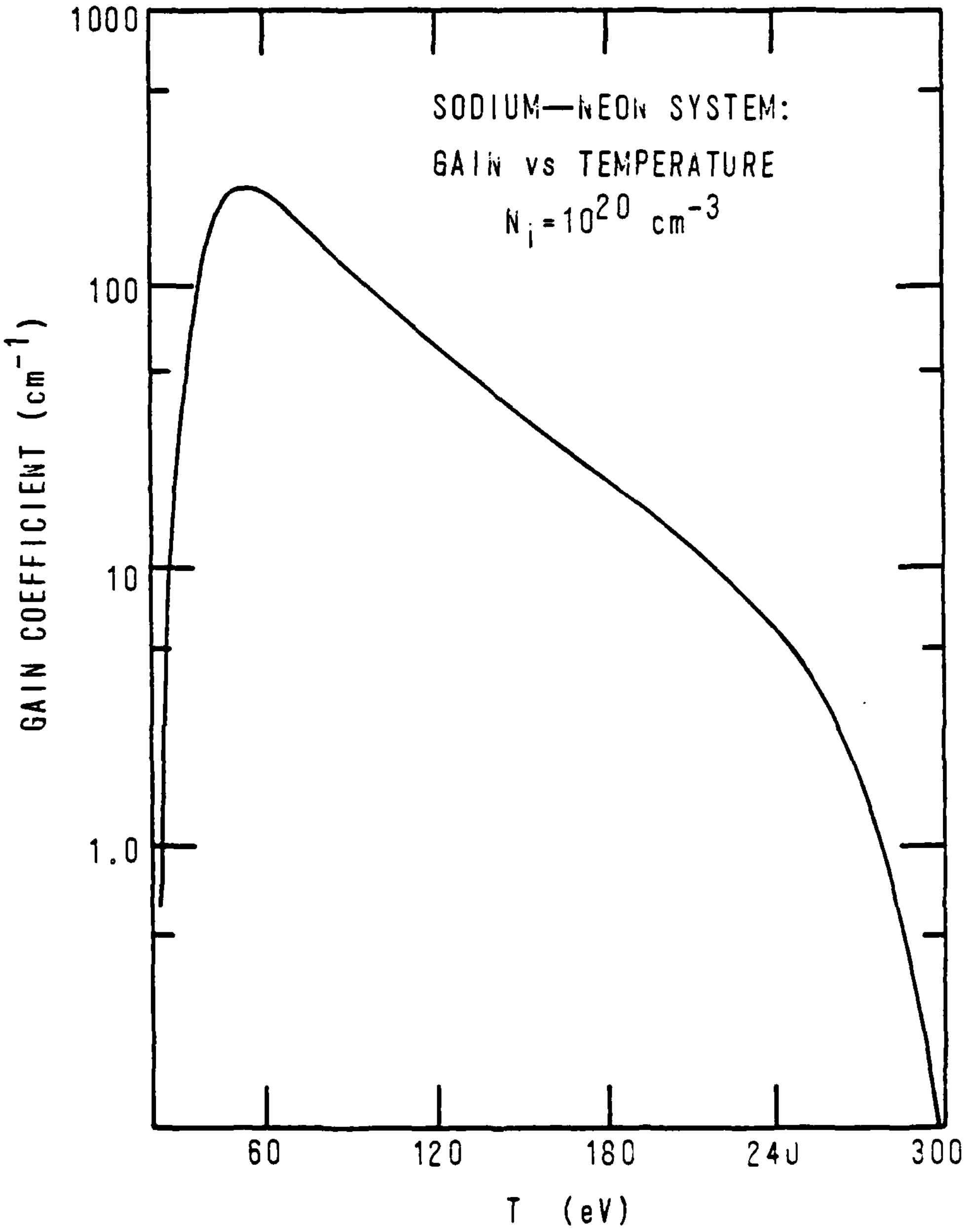

Fig. 5 — Line center gain coefficient in the Ne IX $2p^1P$-$3d^1D$ line is plotted vs. Ne plasma temperature for a fixed Ne ion density of 10^{20} cm^{-3}.

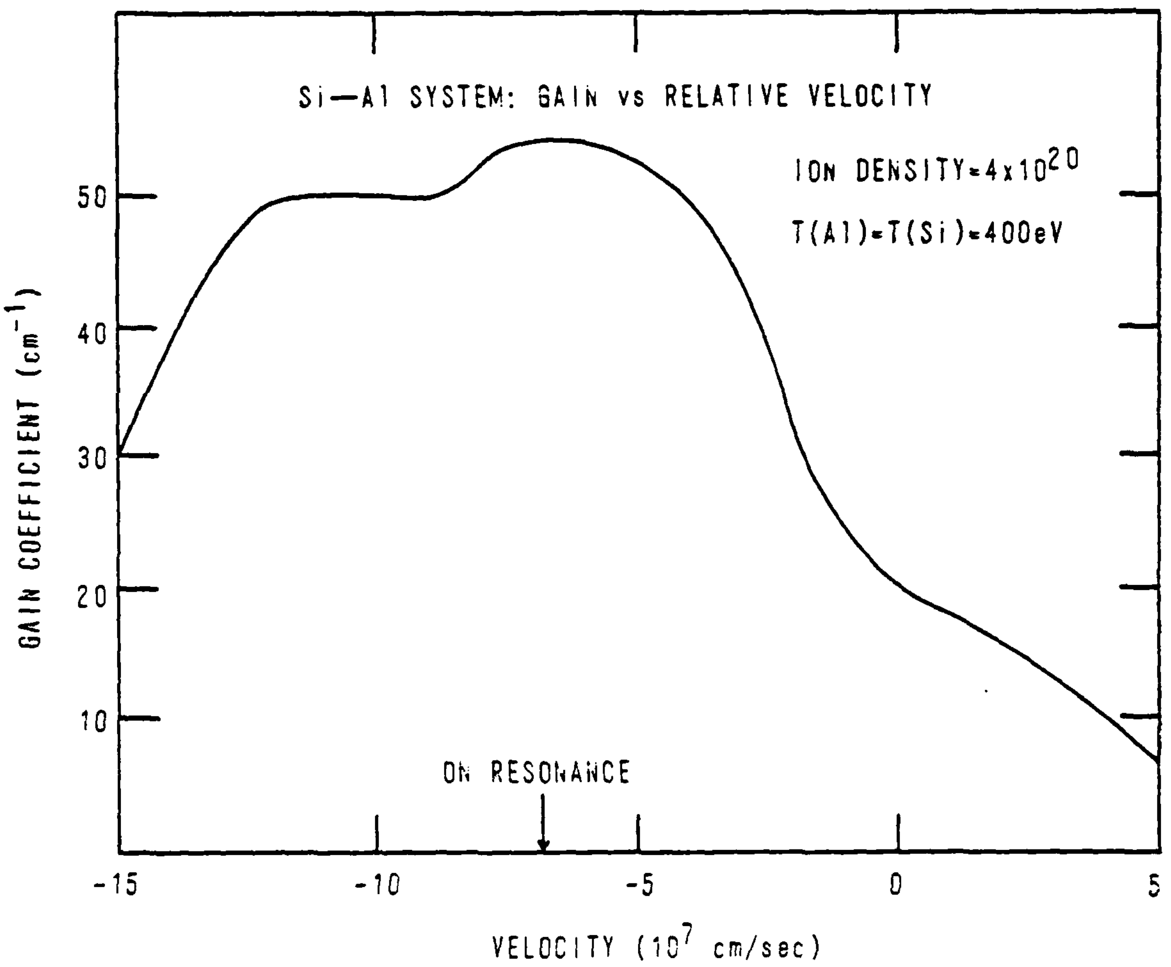

Fig. 6 — Line center gain coefficient in the Al XII $2p^1P$-$3d^1D$ line is plotted vs. velocity of approach of the Si and Al plasmas. The Al ion density is 4×10^{20} cm^{-3} and its temperature (the same as that of the pumping Si plasma) is assumed to be 400 eV.

cm $\sec^{-1}$. This is due to the fact that most of the pumping radiation is not normally incident on the pumped plasma and therefore a range of velocity shifts are sampled (due to the cos θ effect) at any one physical streaming velocity. At the perfectly matched streaming velocity of $6.8\mathrm{X}10^{7}$, gain is ~3 times that of zero streaming velocity because the very highest pumping line intensities just outside the self reversed core are sampled to the greatest degree. Having the two components, Si and Al, approach each other is therefore helpful, but not essential to the scheme's basic viability.

IV. Further Remarks and Conclusions

We have determined through a series of detailed calculations the conditions under which significant gain at x-ray wavelengths, employing the Na/Ne and Si/Al plasmas for resonant photon pumping, should be attainable in the laboratory. Substantial gain at 82 Å and 44 Å for Na/Ne and Si/Al, respectively, is in principle achievable, as documented in Figs. 2-6. However, the task of setting up the correct plasma conditions is not trivial for a number of reasons. For optimum employment of both schemes, the temperature of the pumped plasma should be maintained well below that of the pumping plasma to avoid excessive ionization in the lasing medium. This could perhaps be accomplished by keeping the two components as physically separate as possible to reduce conductive temperature equilibration. Similarly, the pumping plasma might be heated first, and then the pumped medium activated through use of a delayed heating pulse or laser beam to assure that the pumped plasma passes through the optimal temperature range while being exposed to the intense pumping radiation. Also, in previously successful experiments[14], stepped targets using metal plates as heat sinks have allowed experimenters to tune the plasma temperature downward at certain distances from the initial plasma formation surface. Perhaps similar techniques could be employed for the present schemes. Even though a lower pumped plasma temperature is essential for optimum steady state gain, substantial gain is still achievable for equal pumped and pumping plasma temperatures (Fig. 6).

In the case of the Na/Ne system, pumping radiation was generated in an actual pellet implosion experiment at Rochester for which the ion density of the pellet has been diagnosed as $4.5\mathrm{X}10^{21}$ cm^{-3}[8], which is more than an order of magnitude greater than the neon ion density required for maximum gain. In short, a very dense sodium plasma is desirable to obtain high pumping power, but a relatively tenuous neon medium is needed to prevent collisional processes from neutralizing the pumped inversion. Therefore, a configuration which is the reverse of a normal pellet suggests itself. One might compress a cylindrical glass rod (with a cylindrically focussed laser, perhaps) which has been heavily doped with sodium impurities. This rod would initially be encased in neon, which would form a more tenuous blowoff plasma. Or, alternatively two physically separate Na and Ne plasmas could be created with intensities and pulse widths tailored to produce optimum gain characteristics. This would certainly allow different densities to be produced in the separate components, and would minimize or eliminate conductive temperature equilibration. Since ionization of the pumped plasma by pumping radiation other than the resonance line did not present any serious difficulties in the Si/Al calculation, it would not be expected to present a problem in the Na/Ne case. However, this cannot be stated with complete confidence because, as mentioned above, only the Na resonance line radiation is assumed incident on the Ne in our calculations.

ACKNOWLEDGMENT

This work was supported in part by the Defense Nuclear Agency.

REFERENCES

1. A.V. Vinogradov, I.I. Sobelman, and E.A. Yukov, Kvant. Electron. (Moscow) 2, 105(1975) [Sov. J. Quantum Electron. 5, 59 (1975)].

2. B.A. Norton and N.J. Peacock, J. Phys. B 8, 989 (1975).

3. V.A. Bhagavatula, J. Appl. Phys. 47, 4535 (1976).

4. J.P. Apruzese, J. Davis, and K.G. Whitney, J. Phys. B 11, L643 (1978).

5. V.A. Bhagavatula, Appl. Phys. Lett. 33, 726 (1978).

6. V.A. Bhagavatula, IEEE J. Quantum Electron. 16, 603 (1980).

7. K.G. Whitney, J. Davis, and J.P. Apruzese, Phys. Rev. A 22, 2196 (1980).

8. J.P. Apruzese, P.C. Kepple, K.G. Whitney, J. Davis, and D. Duston, Phys. Rev. A., in press.

9. H.R. Griem, M. Blaha, and P.C. Kepple, Phys. Rev. A 19, 2421 (1979).

10. B. Yaakobi, D. Steel, E. Thorsos, A. Hauer, and B. Perry, Phys. Rev. Lett. 39, 1526 (1977).

11. P. Burkhalter, J. Davis, J. Rauch, W. Clark, G. Dahlbacka, and R. Schneider, J. Appl. Phys. 50, 705 (1979).

12. K.G. Whitney, J. Davis, and J.P. Apruzese, "Some Effects of Radiation Trapping on Stimulated VUV Emission in Ar XIII", in Cooperative Effects in Matter and Radiation, edited by C.M. Bowden, D.W. Howgate, and H.R. Robl (Plenum, New York, 1977).

13. V.L. Jacobs, J. Davis, J.E. Rogerson, and M. Blaha, Astrophys. J. 230, 627 (1979); also unpublished calculations for Al.

14. V.A. Bhagavatula and B. Yaakobi, Opt. Commun. 24, 331 (1978).

(This page intentionally left blank.)

Appendix D

DESCRIPTION OF WHYRAD CODE

This appendix is a brief documentation of the main routine and subroutines employed in the program. It is expected that a user closely interested in the code will have access to a listing; this documentation should facilitate understanding of the code architecture. Most of the quantities employed in the input data, in subroutine INITAL or main program WHYRAD, are described in comment blocks immediately adjacent to their input location. Figure 44 shows a general flow chart of the code.

Subroutine INITAL provides the initialization of the dynamic variables whether it's a complete job start or restart. For a $t = 0$ start the radial distributions of temperature, adiabatic exponent, number density, magnetic field, etc. are imputted; a $t > 0$ restart is accommodated by a call to tape #17. The number density initial conditions may be specified by Gaussian distributions of n_I, polynomial representations of n_I, or general cell-by cell readin of ρ ($\approx n_I m_I$).

Subroutine READIN incorporates the atomic physics data for inclusion into the ATPHYS ionization chemistry-radiation package. Only argon data for READIN are presently available.

Subroutine ATPHYS feeds the ground plus first excited state physics into the hydrodynamic cells at each time step: within this routine estimates of ionization level, adiabatic exponent, and the magnitudes of various radiation forms are made. The flag KRAD = 1 selects this routine.

Subroutine VOLTG incorporates the voltage-time profile into the model; linear interpolations between a maximum of 30 normalized time points (t/t_{pulse}) are employed as the representations.

Subroutine CURG incorporates a current-time profile, if desired instead of voltage, into the model. Linear interpolations between a maximum of 30 normalized time points are employed. The flag ICUR = 0 chooses the voltage input, ICUR = 1 chooses the current input.

Program WHYRAD is the main routine in the code. It accepts the namelist READIN of many of the control variables, performs the main solution operations, specifically the extenal circuit coupling and the calling of the ETBFCT numerical integration algorithms, specifies the time step loop, prints out the results and sets up, if desired, the information to be stored on file for the next restart.

Subroutine RTPHYS serves a similar function that ATPHYS does; it translates the ionization-radiation output from the multicell real-time package or the TERRYS curve-fit package to conform as an input to WHYRAD. If the TERRYS radiation package is employed then ionization number and total chemical potential (used for the calculation of the isentropic exponent) are also determined within RTPHYS. In addition, a benchmark radiationless hydrodynamic option (IHYD > 0) may be called within this subroutine.

Subroutine TERRYS links together the curve fit radiation package and writes out the total (line plus continuum) radiation power at each cell (erg/sec cm^3), as well as the cross sectional area integrated power (erg/sec cm) for the total amount, the line radiation < 1 keV photons (L-shell), > 1 keV (K-shell), and continuum.

Subroutine DUST$R incorporates the curve fits of the aluminum or argon MCELL optically thin radiation package, with polynomial dependence of volume emission rate (erg/sec cm^3) on electron temperature at $n_I = 10^{19}$ cm^{-3}; dependence at other densities is estimated by scaling estimates of power law form.

Real function RAD$SP computes the opacities from the radiating cell out to the plasma boundary along the photon path length; free-bound, K and L shell line and a single average frequency free-free radiation modes are considered. If IBCHOC = 1 a more exact ten frequency FF Bremsstrahlung representation is employed.

Subroutine FLBAR incorporates the computation of the ten frequency FF path length along two rays emitting from the cell of interest. Integration is carried through the range of number densities, ionization levels and temperatures along the path.

Real function RC$SIG evaluates the recombination continuum absorption cross section needed for evaluation of the bound-free optical thickness in RAD$SP.

Real function PE$FBC computes the probability of escape for bound-free radiation, while real function PE$LKT computes the probability of escape for line radiation.

Real function LBAR computes the path lengths for line and bound-free radiation transport, with integration carried through the range of number densities and temperatures along the path.

Subroutine DTSET determines the integration time step in terms of the collapse dynamics of the discharge. The minimum time step over the radial cells is evaluated on the basis of the Courant-Fredericks-Lewy sound speed condition, the ratio of the thermal energy to the Joule heating, the ratio of the thermal energy to the local radiative transport, and the ratio of the thermal energy to the previous time step internal energy change. The minimum of these results is taken and employed. The last criterion, based on the internal energy change, is usually the most restrictive. The Alfven speed is also determined here to establish minimum inertia and density in the outer regions of the implosion.

Subroutine DRSET evaluates the dynamic rezoning cell widths based on the local cell ion number density. IDR ≤ 1 selects uniform incrementation, IDR ≥ 2 imposes the rezoning. The cell center radii and the annular incremental volume are also calculated here.

Subroutine BSOLVE incorporates the tridiagonal algorithm for the solution of the self-induced magnetic field as a function of the external circuit-imposed boundary condition and the assumed resistivity function.

Subroutine TRANS specifies the transport coefficients of thermal conductivity, electron-ion temperature relaxation, thermoelectric effect and, in particular, the anomalous resistivity. The choice of classical resistivity, core-corona anomalous resistivity, or one based on the ion sound speed is made with flag ITURB (0, 1, 2, respectively).

Subroutine TDIFF involves the tridiagonal algorithm for the fully implicit solution of the energy equation thermal diffusion source term. This calculates the final temperature value within a time step to represent the complete electron temperature and total internal energy conservation equations.

Subroutine EQUIL evaluates the effects of energy equilibration between the electrons and ions. Also, for comparative purposes, black body heat flux is evaluated here.

Subroutine ECHEK contains the evaluation of the local energy balance between input electrical energy, hydrodynamic internal energy, and radiated energy.

Subroutine ROSSL contains a double linear interpolation (density and electron temperature), giving the Rosseland coefficients for the black body radiation calculation.

The ETBFCT routines (ETBFCT, VELOCE, NGRIDE, SOURCD, OGRIDE, CONSRE) are exactly as found in Ref. 3 except some of the comment statements were not punched.

The MCELL multicell routines specifically called in WHYRAD-MCRAT, UTILIT, and PRRAD connect the hydro package to the full multicell chemistry plus radiation transport package. The calling of these routines has to be specified in JSL statements.

The NRLLIB qualitative plotting code is employed through the calling of ASXASY and IPLOT.

The input cards are first a NAMELIST group for a WHYRAD input, then another group of standard input for INITAL. Then (for the TERRYS package choice, employed in the example calculations of Section V) the Bremsstrahlung radiation frequency table is read in, in INITAL, for use in subroutine RTPHYS. Initial conditions over the radial distributions come next (read in INITAL) starting from RADX(I) through BO(I) {magnetic field}. For a restart, quantities from EMAS, EADD, ... (statement 505) through to READ (M,105) (BO(I), I=1,NR), statement 161, are input from the storage file. Finally, the voltage distribution is input through VOLTG.

AD-A113 597   SCIENCE APPLICATIONS INC MCLEAN VA   F/G 20/9
RADIATION FROM HIGH TEMPERATURE PLASMAS.(U)
FEB 82 E KANE, J APRUZESE   N00173-80-C-0493
UNCLASSIFIED   SAI-82-686-WA   NL

3 OF 3
AD A
113597

END
DATE
FILMED
5-82
DTIC

Appendix E

LIST OF SYMBOLS

a	B/z
b	Coefficient in optically thin representation
B	Azimuthal magnetic field
B	Gaussian density distribution coefficient
c	Speed of light
C_1	Ion sound speed
C_s	Sound speed
D	Source function term
e	Electron charge
E	Plasma internal energy
E_{TCP}	Total chemical potential energy
h	Planck's constant
I	Total axial current
IP	Ionization potential
j	Axial current
k	Boltzmann's constant
$k_{e\perp}$	Thermal conductivity
[illegible]	Radiation path length
L	Electrode spacing discharge length
L_g	Circuit inductance
m	Specie mass

M	Power in rezoning algorithm
M	Pinch mass
n	Number density
N	Coefficient in optically thin representation
NR	Computational cell number
p	Pressure
P	Probability of escape function
P_{RAD}	Radiative power
q_e	Thermal flux
Q_e	Heating term
r	Radial coordinate
r_w	Return circuit radius
R	Gas constant
R	Pinch radius
Ry	Rydberg
t	Time
T	Temperature
U_z	Axial current velocity (drift speed)
v	Radial velocity
V_g	Driving voltage
V_p	Plasma voltage
z	Axial coordinate
Z_g	Circuit impedance
Z_I	Ionization number
ZA	Atomic number

[illegible]	Thermal flux coefficient
γ	Isentropic exponent
ε	Axial electric field
ε_j	Emission coefficient
η	Resistivity
κ	Absorption coefficient
Λ	Coulomb logarithm
ν	Radiation frequency
ρ	Density
σ	Cross section
τ	Relaxation time
$\tau_{\ell,s}$	Optical depths
[illegible]	Generalized density function
ω	Cyclotron frequency
ω_p	Plasma frequency

<u>Subscripts</u>

BF	Bound-free radiation
e	Electron
FF	Free-free (Bremsstrahlung) radiation
I	Ion
j	Radiative frequency integer
K	K-shell
ℓ	Long path
L	L-shell

R	At outer pinch radius
S	Short path
0	At pinch centerline
an	Anomalous transport coefficient
$c\ell$	Classical microscopic transport coefficient
OT	Optically Thin

Appendix F

PROMINENT FORTRAN VARIABLES

FORTRAN SYMBOL	VARIABLE
AJZ(I)	j
ANE(I)	n_e
ANI(I)	n_I
BN(I)	B field (new)
BO(I)	B field (old)
DR(I)	dr
EDOTJ(I)	εj
EFIELD(I)	ε
ENEW(I)	E
ETA(I)	η
FLPLAS	L
FVOL(I)	cell volume
GAMMA(I)	γ
PNEW(I)	p
PRAD(I)	P_{RAD}
RADN(I)	cell center r
RB(I)	cell boundary radius
RC(I)	cell center r
RNEW(I)	ρ
RVOLD(I)	ρV

FORTRAN SYMBOL	VARIABLE
PV(I)	pv
TCP(I)	L_{TCP}
TEV(I)	T_e
TE(I)	T_e
TI(I)	T_I
VEL(I)	v
VG	input voltage
Z(I)	Z_I

LMED

-8